Università degli Studi di Bologna

Facoltà di Scienze Matematiche Fisiche e Naturali

Search for a Diffuse Flux of Astrophysical Muon Neutrinos in the ANTARES Telescope

Simone Biagi

Advisor: Prof. Maurizio Spurio

PhD Coordinator: Prof. Fabio Ortolani

Dottorato di Ricerca in Fisica - XXII ciclo

Settore Scientifico Disciplinare: FIS/01

Marzo 2010

Contents

Introduction

Neutrino astronomy is a very young branch of astroparticle physics. The close relationship between cosmology and particle physics was recognised only relatively recently. In the first minutes of life, the Universe was a micro-world that can only be described by quantum-theoretical methods of elementary particle physics. Today, particle physicists try to recreate the existed conditions in the early Universe by using electron-positron, proton-antiproton, and proton-proton collisions at high energies.

From an historical point of view, Galileo innovated the astronomy by using the telescope to enhance his observations. Today we know that the visible radiation is just a small region of the electromagnetic spectrum. In addition to the electromagnetic radiation, the detection of cosmic rays also plays a fundamental role in our understanding of the astrophysical objects. Recently, the Auger experiment shows the first hints of association of cosmic rays with $E > 6 \times 10^{19}$ eV and nearby extragalactic objects.

The disadvantage of classical astronomies like observations in the radio, infrared, optical, ultraviolet, X-ray, or γ-ray band is related to the fact that electromagnetic radiation is absorbed in matter. In addition, energetic γ-rays from distant sources are attenuated by interactions with photons of the cosmic microwave backround.

A similar limitation affects also the observation of charged cosmic rays. Protons interact with the cosmic microwave background, that limits their range to < 100 Mpc for $E_p \sim 10^{20}$ eV. At lower energies, the directional information is lost because of the irregular galactic magnetic fields that randomise the original proton direction.

Neutrons, on the other hand, does not suffer the deflection due to magnetic fields, but their short lifetime limits severely their range.

The requirements for an *optimal* cosmic-messenger can be summarised as follows: the particle should be neutral, stable and weakly interacting. A candidate that fulfils all these conditions is the neutrino.

INTRODUCTION

Neutrinos can travel distanced much longer than protons or photons because they only interact weakly. Neutrinos are not deflected during their travel from the source to the Earth, hence they allow to identify galactic and extragalactic sources of cosmic rays. However, large detectors are needed to compensate the low interaction cross section; this is also the reason why they have not been used in astronomy until very recently. In 1960, Markov proposed a possible way to detect high-energy neutrinos using huge volumes of natural material such as ice o deep seawater. Muon neutrinos produced in astrophysical objects would interact via charged current with one of the nucleons of the surrounding medium. Neutrino charged current interaction would induce a muon that emits Cherenkov photons in the ice or water, to be detected by a lattice of photomultipliers installed in the medium. At energies above $\sim$ TeV muons resulting from charged current interactions can travel kilometres and are almost collinear with the parent neutrinos. Given the low cross section of the νN interaction and the predicted astrophysical neutrino fluxes, the typical size of the detector should be of the order of km^3.

The ANTARES high-energy neutrino telescope is a three-dimensional array of photomultipliers distributed over 12 lines installed in the Mediterranean Sea. The detector has been operated in partial configurations since March 2006 and was completed in May 2008. The main goal of the experiment is the search for high-energy neutrinos from astrophysical sources. A neutrino telescope in the Northern hemisphere includes the Galactic Centre in its field of view and is complementary to the IceCube Antarctic telescope. It is also meant to be a first step towards a km^3 neutrino observatory in the Northern Hemisphere.

In this thesis, the search for very-high energy ($E > 10$ TeV) extraterrestrial muon neutrinos from unresolved sources is presented. The sensitivity of point source search techniques should be too small to detect neutrino fluxes from individual sources; however it is possible that many sources could produce an excess of events over the expected atmospheric neutrino background. The discrimination between the cosmic signal flux and the atmospheric neutrino background can be only made on the basis of the neutrino energy. An energy estimator is proposed in this work, and the sensitivity of the ANTARES detector to diffuse muon neutrinos is evaluated from MonteCarlo simulations. A first look to the data is also presented.

The structure of this thesis is as follows. A general overview of the knowledge of cosmic rays and neutrino astronomy in given in Chapter 1. In Chapter 2 the neutrino interaction and the detection principle is explained. Then, the ANTARES telescope is presented (Chapter 3). The MonteCarlo simulation tools and the samples that have been generated are shown in Chapter 4. In Chapter 5 the analysis for the search of diffuse flux neutrinos is explained and the ANTARES sensitivity estimated. Finally, Chapter 6 is devoted to make a comparison with the real ANTARES data.

Chapter 1

Physics of cosmic rays

1.1 High energy cosmic rays

Cosmic rays were discovered in 1912 by V. Hess [1]. Using three golden electrometers he measured the amount of radiation up to an altitude of 5300 meters in a free balloon flight. He found that the level of radiation increased with altitude, showing that some kind of radiation enters the atmosphere from above. This contradicts the hypothesis that the flux of ionizing particles arises from Earth's radioactive rocks exclusively. He gave the name of "cosmic radiation" to this phenomenon. Hess received the Nobel Prize in Physics in 1936 for his discovery.

1.1.1 Composition and energy spectrum

Charged Cosmic Rays (CR) have been observed from energies of $E_{CR} \sim 10^9$ eV up to $E_{CR} \sim 10^{21}$ eV (Fig. 1.1). Almost 90% of all the incoming cosmic ray particles are simple protons, with nearly 10% being helium nuclei (alpha particles), and slightly under 1% are heavier elements, electrons (beta particles), or gamma ray photons. The composition of Cosmic Rays is quite similar to the one of Solar System, with some relevant differences (Fig. 1.2). First of all, nuclei with $Z > 1$ are much more abundant in Cosmic Rays. Then two groups of elements (Li-Be-B and Sc-Ti-V-Cr-Mn) are many orders of magnitude more abundant in Cosmic Rays than in the Solar System: these abundances can be explained considering the collisions of carbon and oxygen (for the first group) and of iron (for the second one) with the interstellar medium that produce lighter elements through a process of spallation.

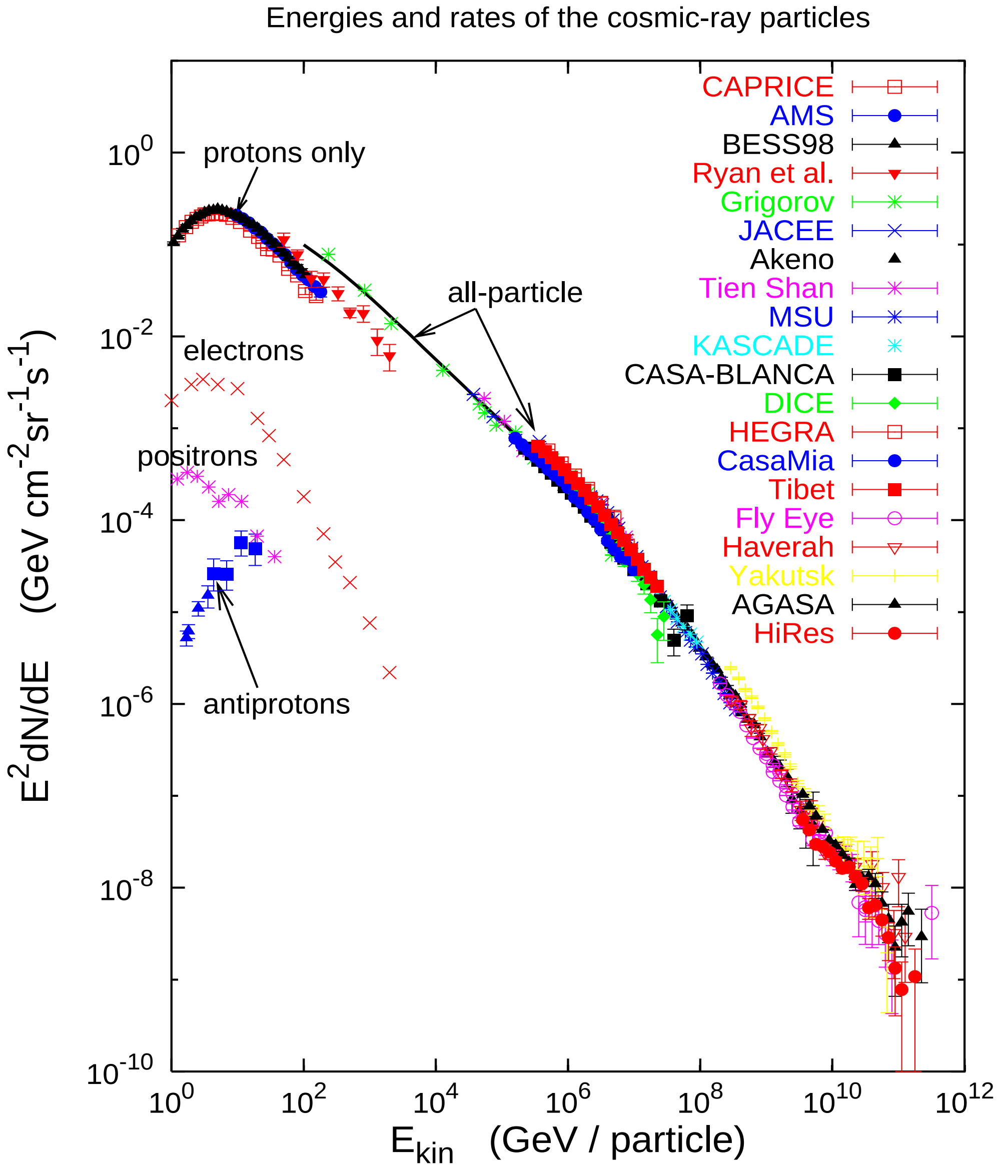

Figure 1.1: Primary Cosmic Ray spectrum from 10^9 to 10^{21} eV as measured from Earth [2]. The vertical scale has been multiplied by E^{-2} to emphasise the changing shape of the spectrum.

The energy spectrum follows a broken power law of the form:

$$\frac{dN}{dE} \propto E^{-\alpha}. \tag{1.1}$$

Two kinks are present in the spectrum, referred to as *knee* and *ankle*. The spectral

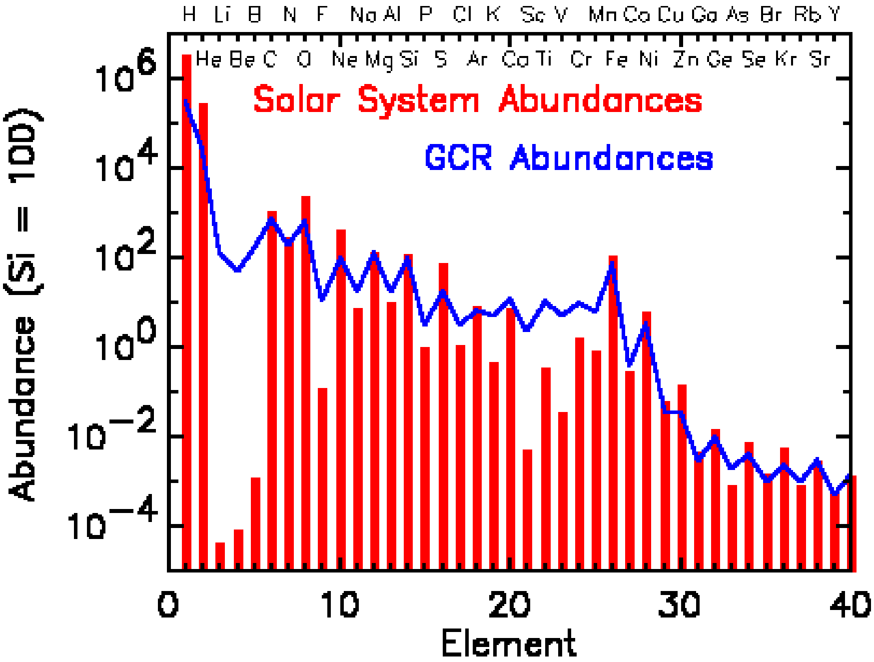

Figure 1.2: Relative abundance of elements in Cosmic Rays with $E \sim 100$ GeV compared with Solar System abundance. Both data have been normalised to $Si = 100$ [3].

indices for different parts of the spectrum are [4]:

$$\alpha \approx \begin{cases} 2.67 & \text{for} \qquad\quad \log(E/\text{eV}) < 15.4 \\ 3.10 & \text{for } 15.4 < \log(E/\text{eV}) < 18.5 \\ 2.75 & \text{for } 18.5 < \log(E/\text{eV}). \end{cases} \tag{1.2}$$

Below $\sim$ 10 GeV per charged particle the flux of cosmic rays is reduced by the solar wind shielding, and below $\sim$ 100 MeV CRs are not energetic enough to reach the Earth.

Up to energies of $\sim 10^{14}$ eV, the CR spectrum is directly measured above the atmosphere. In this energy range, the Fermi mechanism is responsible for the acceleration of CRs [5; 6]. The so called *standard model of galactic CRs* has been confirmed by experiments on satellites and stratospheric balloons that also provided the most relevant information about the composition of CRs. A conclusive evidence of connection with sources is still missing. The arrival direction at the Earth of CR is randomised by the Galactic ($B \simeq 3$ μG) and intergalactic ($\sim$ nG) magnetic fields. The gyro-radius of a nucleus having charge Z and energy E (in eV) is:

$$R_{gyro}(E) = \frac{E \times B_{Galaxy}}{Z} \simeq 3 \times 10^{-16} \frac{E}{Z} \text{ [pc]}. \tag{1.3}$$

R_{gyro} is comparable with the thickness of the Galactic disk ($\simeq$ 200 pc) for a proton with $E \sim 10^{18}$ eV. This means that pinpointing of charged CR sources is possible only with protons having $E > 10^{19}$ eV.

Beyond 3×10^{15} eV, the spectral index changes and becomes more hard. The *knee* of the CR spectrum is still an open question and different models have been proposed to explain this particular shape [7]. Some models expect a maximum energy for the CR, due to the iterative scattering processes involved in the acceleration sites. The maximum energy depends on the nucleus charge Ze, leading the prediction of a different cutoff for every nucleus type. As a consequence, CR composition is expected to be proton-rich before the *knee*, and iron-rich after.

Above energies of $\sim 10^{14}$ eV, due to the low flux of cosmic rays, measurements are accessible only from big infrastructures located on the ground. Detector arrays reveal showers of secondary particles created by interaction of primary CRs and distributed in a large area. For instance, KASCADE explored the region around the *knee* [8]. Although experimental techniques are very difficult and have poor resolution, observations of this region of the energy spectrum seem to indicate that the average mass of CRs increases when passing the *knee*.

The highest CRs exceed even 10^{20} eV. After the *ankle*, where is a flattening in the spectrum, it is generally assumed that CRs have extragalactic origin. No galactic source class is energetic enough for the production of particles at such high energies, and the gyro-radius of the particles becomes too large and they escape from the galaxy already at lower energies. In addition, at energies $\sim 10^{20}$ eV, the particle diffusion is low compared to the traveling path through the Galaxy [9]. The observed particles point in this case back to their original source. The observed events are isotropically distributed, which is only possible for travelling lengths longer than the diameter of the galaxy.

Above 6×10^{19} eV the CR flux is expected to be suppressed by the Greisen-Zatsepin-Kuz'min (GZK) effect [10; 11]. The cut-off in the flux is caused by the photo-interaction of protons with the 2.7 K Cosmic Microwave Background (CMB) radiation. The observation of a suppression in the ultra high energy region of the CR energy spectrum is confirmed both by HIRES [12] and Auger [13], while in the AGASA data [14], now under revision, the suppression was not observed. However, in the most recent analysis of the Auger data, including all the events collected up to March 2009, the interpretation of the Ultra High Energy Cosmic Ray spectrum in terms of GZK effect cannot be firmly established.

1.1.2 Acceleration mechanism

The origin of cosmic rays is a key issue for neutrino astronomy: in fact high energy neutrino production is related with the acceleration of cosmic rays. One of the difficulties in the determination of the origin of cosmic rays comes from the fact that charged particles are deviated by the Galactic and extra-Galactic magnetic fields.

The Fermi mechanism, introduced in the previous subsection, explains the particle acceleration by iterative scattering processes of charged particles in a shock-wave. These shock-waves are assumed to be originated in environments of exceptional gravitational forces, like the vicinity of black holes or stellar gravitational collapses. Stochastic particle acceleration can be described by following a particle entering an acceleration region with an energy E through the acceleration process, until it exits the region again. It is assumed that particles are accelerated at moving magnetic fields inhomogeneities, and in each encounter, it increases its energy by an amount proportional to its energy ($\Delta E = \xi \times E$). The gain ξ comes from the movement in magnetic field inhomogeneities.

Two basic configurations for stochastic acceleration can be considered. The first approach is to consider a moving gas cloud (Fig. 1.3, left). Particles are scattered elastically in the irregularities of the magnetic field, and their direction is randomised in the cloud. Particles escape from the cloud in any direction with an average gain in energy $\Delta E \propto \beta^2 E$, proportional to the squared cloud velocity. This is called the second order Fermi acceleration mechanism.

In comparison, the first order Fermi acceleration mechanism considers a plane, infinite shock front (Fig. 1.3, right). In this case, particles do not enter into a cloud but go back and forth between the shock-wave front. The average energy increase is $\Delta E \propto \beta E$, where β is the velocity of the shocked plasma flow. Note that the second order mechanism is independent of the velocity direction, but it is of second order and not very efficient ($\beta \sim 10^{-2}$).

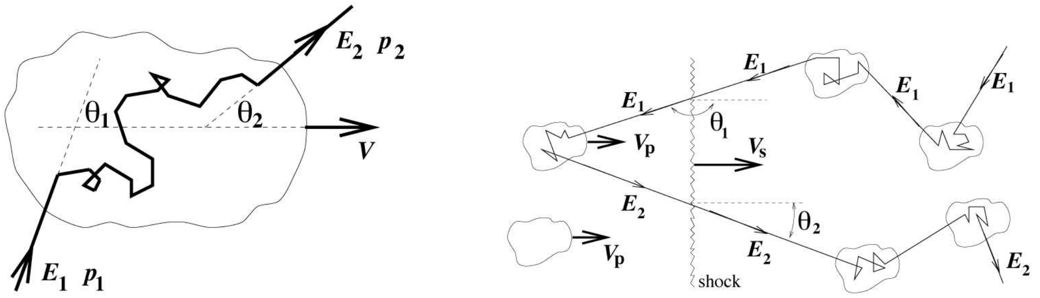

Figure 1.3: Left: Second order Fermi acceleration. Interaction of a cosmic particle of energy E_1 in a magnetised cloud moving with speed V. Right: First order Fermi acceleration. The shock is considered to be plane, moving with a velocity V_s. Figure taken from [15]

The Fermi mechanism is supposed to occur after supernova explosions, giving a maximum energy to a charged particle of $\sim$ 100 TeV. During the travel of these accelerated cosmic rays trough the Galaxy, they can interact and produce gamma-rays, positrons, neutrons, anti-protons and neutrinos.

The supernova remnant (SNR) models cannot explain the CR flux above the *knee*, but there is no consensus on a preferred accelerator model up to 10^{19} eV. CRs can be accelerated beyond the *knee* if, for instance, the central core of the supernova hosts a rotating neutron star. Already accelerated particles can also suffer additional acceleration due to the neutron star strong variable magnetic field. The maximum energy cannot exceed $\sim 10^{19}$ eV [16].

1.2 High energy γ-rays

Some galactic accelerator must exist to explain the presence of CRs with energies up to the *ankle*. These sources can be potentially interesting for a neutrino telescope.

Due to the influence of galactic magnetic fields, charged particles do not point to the sources. Neutral stable particles, photons and neutrinos, do not suffer the effect of magnetic fields: they represent decay products of accelerated charged particles but cannot be directly accelerated.

There are mainly two mechanisms to produce such γ-rays: we refer to a *leptonic model* [17; 18] when electrons are accelerated, and to a *hadronic model* [19] when protons or other nuclei are accelerated. In the leptonic model the most important processes which produce high energy γ-rays are synchrotron radiation, *bremsstrahlung* and Inverse Compton (IC) scattering. Interactions of energetic electrons with ambient background photon fields produce IC γ-rays with a high efficiency. In the hadronic model it is assumed that photons are produced by the decay of neutral pions. This mechanism implies that in addition to neutral pions, charged pions should also be produced. In this case, if high energy photons are produced in the hadronic model, high energy neutrinos will be produced as well. For this reason, the sources that emit high energy photons will be described in this section.

Most of observed TeV γ-ray galactic sources have a power law energy spectrum $E^{-\alpha_\gamma}$, where $\alpha_\gamma \sim 2.0 \div 2.5$. The values of the spectral index are very close to the expected spectral index of CR sources.

The Energetic Gamma-Ray Experiment Telescope (EGRET) detected in the 1990s photons in the MeV $\div$ GeV range [20]. The last EGRET catalogue contains 271 detections with high significance; it can be seen that apart from extragalactic objects like Active Galactic Nuclei or galactic Pulsars, most of the other sources have not been identified.

Following its launch in June 2008, the *Fermi Gamma-ray Space Telescope (Fermi)* began a sky survey in August [21]. The Large Area Telescope (LAT) on *Fermi* in 3 months produced a deeper and better-resolved map of the γ-ray sky than any previous space mission. In Fig. 1.4 the 205 most significant γ-ray sources with energies above 100 MeV are shown; most of them are in the galactic plane.

Because of gamma ray fluxes at energies greater than 100 GeV are very low, ground-based detectors are needed. High energy γ-rays are absorbed when reaching the Earth atmosphere, and the absorption process originates a cascade of high energy relativistic secondary particles. These particles will eventually emit Cherenkov radiation, at a characteristic angle in the visible and UV range, which can be detected at ground level by means of telescopes that collect the light towards photomultipliers. This method, the Imaging Air-Cherenkov Technique (IACT), can provide the direction and energy informations of the primary photon.

Pioneering ground based γ-ray experiments proved the feasibility of the IACT, such as Whipple [22], HEGRA [23], CANGAROO [24] and CAT[25]. At present, the new generation apparatus are the HESS [26] and VERITAS [27] telescope arrays and the

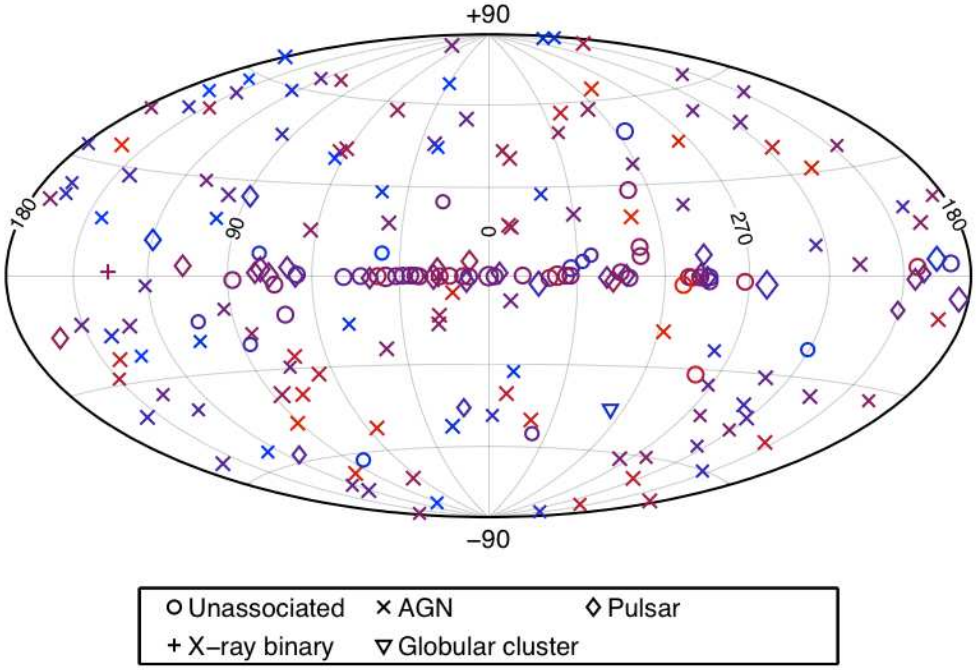

Figure 1.4: The LAT Bright Source List, showing the locations on the sky (Galactic coordinates in Aitoff projection) coded according to the legend. The colours of the symbol indicate relative spectral hardness on a sliding scale. Symbols more blue in colour indicate sources with harder spectra than those that are more red [21].

MAGIC [28] telescope. These IACT telescopes have provided a catalogue of TeV γ-ray sources. Of particular interest (mainly for a neutrino detector placed in the North hemisphere) is the great population of TeV γ-ray sources in the galactic centre region discovered by the H.E.S.S. telescope.

The mean free path travelled by photons is limited by interactions with the infra-red, microwave and radio background photons. The γ-ray absorption length as a function of the energy is shown in Fig. 1.5; in particular, above 10 TeV the horizon of photons is limited to less than 10 Mpc.

1.3 TeV γ-rays and neutrino production

The astrophysical production of high energy neutrinos is mainly supposed via the decay of charged pions in the interaction of high energy nucleons with matter or radiation.

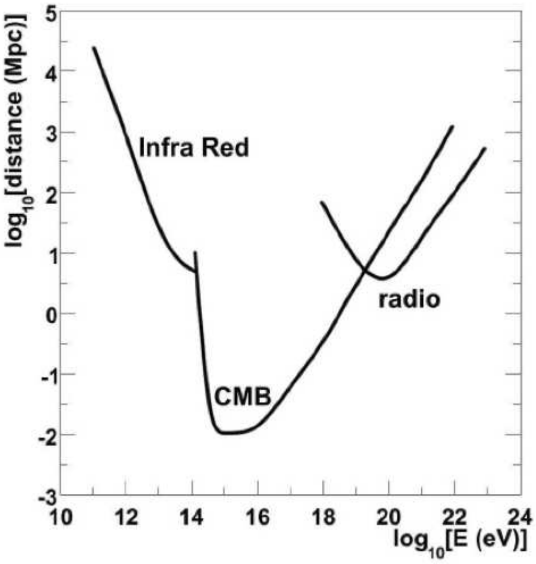

Figure 1.5: Absorption length of HE photons as a function of their energy. They interact with lower energy Infra-Red photons, with the Cosmic Microwave Background radiation and with photons in the radio domain.

Accelerated protons will interact in the surroundings of the CRs emitter with photons predominantly via the Δ^+ resonance:

$$\begin{aligned} p+\gamma &\rightarrow \Delta^+ \rightarrow \pi^0 + p \\ p+\gamma &\rightarrow \Delta^+ \rightarrow \pi^+ + n \end{aligned} \tag{1.4}$$

Protons will interact also with ambient matter (protons, neutrons and nuclei), giving rise to the production of charged and neutral mesons. The relationship between sources of VHE γ-ray ($E_\gamma > 100$ MeV) and neutrinos is the meson-decay channel. Neutral mesons decay in photons (observed at Earth as γ-rays):

$$\pi^0 \rightarrow \gamma\gamma \tag{1.5}$$

while charged mesons decay in neutrinos:

$$\begin{aligned} &\pi^+ \rightarrow \nu_\mu + \mu^+ \\ &\qquad\qquad \hookrightarrow \mu^+ \rightarrow \overline{\nu}_\mu + \nu_e + e^+ \\ &\pi^- \rightarrow \overline{\nu}_\mu + \mu^- \\ &\qquad\qquad \hookrightarrow \mu^- \rightarrow \nu_\mu + \overline{\nu}_e + e^- \end{aligned} \tag{1.6}$$

Therefore, in the framework of the hadronic model and in the case of *transparent sources*, the energy escaping from the source is distributed between CRs, γ-rays and neutrinos. A transparent source is defined as a source of a much larger size that the proton mean free path, but smaller than the meson decay length. For these sources, protons have large probability of interacting once, and most secondary mesons can decay.

Because the mechanisms that produce cosmic rays can produce also neutrinos and high-energy photons (from eqs. 1.5 and 1.6), candidates for neutrino sources are in general also γ-ray sources. In the hadronic model there is a strong relationship between the spectral index of the CR energy spectrum $E^{-\alpha_{CR}}$, and the one of γ-rays and neutrinos. It is expected [29] that near the sources, the spectral index of secondary γ and ν should be almost identical to that of parent primary CRs: $\alpha_{CR} \sim \alpha_\nu \sim \alpha_\gamma \sim 2.2$.

Protons also interact in *pp* and *pn* interactions and the energy escaping from the source is distributed between CRs, γ-rays and neutrinos. This implies that the observed CR flux will limit the expected neutrino flux, since the neutrino energy generation rate will never exceed the generation rate of high energy protons. The upper bound derived from a generic transparent sources is of $E_\nu^2\ \Phi_\nu < 4.5 \times 10^{-8}$ GeV cm^{-2} s^{-1} sr^{-1}, which is often referred to as the *Waxman-Bahcall* (WB) flux [30; 31]. See §1.5.1 for a more detailed explanation about the WB upper limit.

1.4 Astrophysical ν sources

In this section the neutrino emitter candidates are reviewed, according to the classification in extragalactic and galactic sources.

1.4.1 Extragalactic sources

The extension of the CR spectrum above the ankle is assumed to be the result of an extragalactic contribution in the CR components. Therefore, the existence of extragalactic high energy neutrino sources is directly implied by the CR observations. If hadronic particles (protons or any other nuclei) are accelerated in extragalactic objects it is reasonable to think that a neutrino flux will be also produced in such environments. The most plausible sources of Ultra High Energy Cosmic Rays (UHECR) are Active Galactic Nuclei (AGN) and Gamma Ray Bursters (GRB).

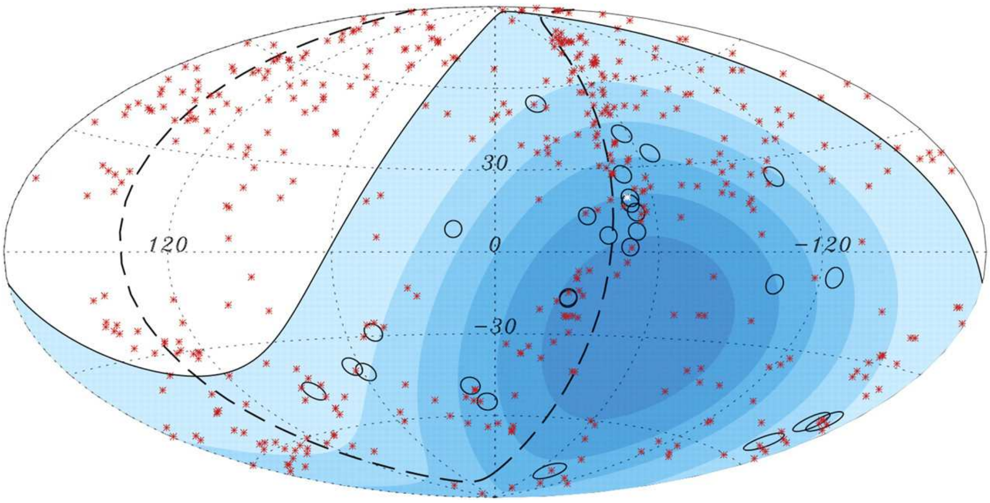

Figure 1.6: Aitoff projection of the celestial sphere in galactic coordinates with circles of radius 3.1° centred at the arrival directions of the 27 cosmic rays with highest energy detected by the Pierre Auger Observatory. The positions of the 472 AGN (318 in the field of view of the Observatory) with distances $< 75Mpc$ are indicated by red asterisks. The solid line represents the border of the field of view (zenith angles smaller than 60). Darker colour indicates larger relative exposure. Each coloured band has equal integrated exposure. The dashed line represents the super-galactic plane. [32].

The search for UHECR sources must take into account the GZK cutoff, which imposes a theoretical upper limit on the energy of CRs from distant sources. At present, the largest experiment that performs measurements at energies above 10^{18} eV is the Auger observatory. Auger has published the results of the analysis of the first data set, rejecting the hypothesis that the cosmic ray spectrum continues in the form of a power law above $10^{19.6}$ eV with 6 sigma significance. In Fig. 1.6 the first hints of association of CRs with $E > 6 \times 10^{19}$ eV and nearby AGN is shown [32]. Although the results do not exclude any other CR sources distributed among the nearby galaxies (in a similar way to AGN), the data suggest that AGN are the most promising candidates for CR emission and therefore an accompanying neutrino flux is expected.

1.4.1.1 Active Galactic Nuclei

Galaxies with a very bright core of emission in their centre are called Active Galactic Nuclei. Models of AGN concentrate on the possibility of a supermassive black hole which lies at the centre of the galaxy.

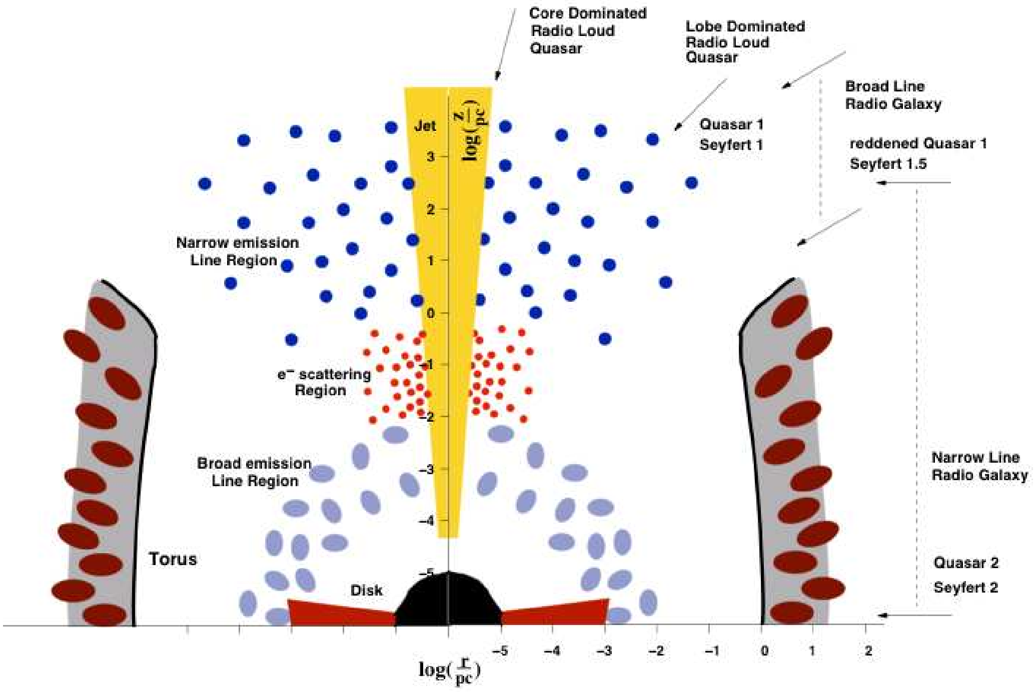

Figure 1.7: Scheme of a cylindrically symmetric AGN shown in the r-z-plane. It is indicated which objects are believed to be seen from particular directions.

A schematic view of the general picture of an AGN is shown in Fig. 1.7.

The supermassive black hole ($10^6 \div 10^9$ solar masses) at the centre of the AGN would attract material onto it, releasing a large amount of gravitational energy. The accretion disk is fed by matter from a dust torus. Typically, two jets are observed, emerging perpendicular to the accretion disc. In these jets particles can be accelerated. These particle beams can interact with the ambient matter and photons. An AGN appears especially bright when one of the jets is oriented along our line of sight. In this case the AGN is called *blazar* and represents the best chance to be detected as an individual point source of neutrinos because of a significant flux enhancement in the jet.

According to some models, this mechanism can generate an energy rate greater than $L > 10^{47}$ erg s^{-1}, which makes AGN the brightest steady sources.

1.4.1.2 Gamma Ray Bursts

Photon eruptions of unknown origin were detected in the 1960s by both America and Soviet military satellites, which aimed to detect banned atomic bomb tests; it was immediately clear that these events were not man made. These phenomena are characterised by a brief flash of gamma-rays, often followed by X-ray, optical and radio emission carrying most of their energy in > 1 MeV photons, with a duration typically from milliseconds to tens of seconds.

There is not a single model to describe these spectacular events. The most accepted is the *fireball* model (Fig. 1.8), which assumes that matter moving at relativistic speed powered by radiation pressure collides with other material in the vicinity. The likely origin is the collapse of massive objects to a black hole. This assumes that a fireball expanding with a highly relativistic velocity (Lorentz factor $\Gamma \sim 300$) is produced in the collapse, powered by radiation pressure. Protons accelerated in the fireball shocks lose energy through interactions with ambient photons. The interaction rate between photons and protons is very probably due to the high density of ambient photons and yields a significant production of pions, which decay in neutrinos carrying typically 5% of the proton energy. Hence, neutrinos with $E_\nu \sim 10^{14}$ eV are expected [33]. Depending on models, a different neutrino contribution is expected at every step of the GRB evolution.

Being transient sources, GRBs detection has the advantage to be practically background free, since neutrino events coming from GRB are correlated both in time and direction with γ-rays. Some calculations of the neutrino flux [34] from GRB show that a kilometre-scale neutrino telescope can be sufficient to allow detection. The average energy of these neutrinos (~ 100 TeV) corresponds to a value for which neutrino telescopes are highly efficient.

1.4.2 Galactic sources

Sources of the CRs for energies up to the ankle are supposed to be galactic. These sources can be very interesting for a neutrino telescope. Their main advantage, with respect to the extragalactic ones, is their relatively close distance to the Earth (orders of 10 kpc). A list of the most promising Galactic sources of neutrino are presented in the following. Some of them seem to be almost *guaranteed* neutrino sources since

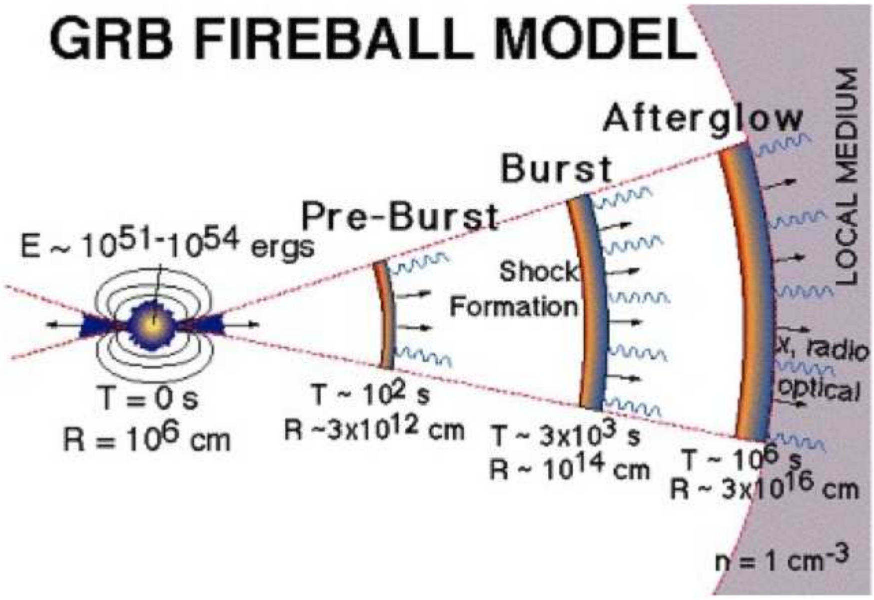

Figure 1.8: The GRB *fireball* model. Moving material at relativistic speeds ($\Gamma \sim 300$) which interacts with the surrounding medium produces γ-rays and the afterglow.

complementary observations from γ-ray telescopes can not be explained by leptonic models alone.

1.4.2.1 Supernova remnants

The CR spectrum at energies below the *knee* is commonly believed to be produced by the shock fronts in expanding shells of supernova remnants (SNR). When a star perishes in a supernova (SN) explosion, the emitted material encounters the interstellar medium, building a shock front. Charged particles are accelerated in the shockwaves of the expanding shells via the Fermi mechanism. In spite of the low expected explosion rate (2-4 per century), significant flux of high energy neutrinos can be produced during the short period after the explosion. In addition, these events will arrive in a short time window, which makes their detection easier.

If the final product of the SN is a neutron star, already accelerated particles can gain additional energy due to its strong magnetic fields. SNRs are considered to be the most likely sites of Galactic CRs acceleration [16].

1.4.2.2 Pulsar Wind Nebulae

A Pulsar Wind Nebula (PWN) is a nebula believed to be powered by a relativistic wind of particles and magnetic fields from a pulsar, which blows out jets of very fast-moving material into the nebula. The radio, optical and X-ray observations suggest a synchrotron origin for these emissions. The HESS telescope [26] has also detected TeV γ-ray emission from the Vela PWN, named Vela X, claiming that this emission is likely produced by the inverse Compton mechanism, but the possibility of an hadronic origin for the observed γ-ray spectrum, with the consequent flux of neutrinos, was also considered [35].

Neutrino fluxes have been calculated in [36] (considering hadronic production) for a few PWNe observed in TeV γ-rays (such as the Crab, the Vela X, the PWN around PSR1706-44 and the nebula surrounding PSR1509-58) with the conclusion that all these PWNe could be detected by a kilometre-scale neutrino telescope.

1.4.2.3 Micro-quasars

Micro-quasars are one of the most promising Galactic candidates for neutrino astronomy. They are galactic X-ray binary systems composed of an accreting massive object such as a black hole or a neutron star and a companion star which provides mass to the firs one (Fig. 1.9). They display relativistic radio-emitting jets, probably fed by the accretion of matter from the companion star. Micro-quasar resemble AGN (see §1.4.1.1), but at a much smaller scale.

The best candidates as neutrino sources are the steady micro-quasars SS433 and GX339-4. Assuming reasonable scenarios for TeV neutrino production, a km^3 scale neutrino telescope in the Mediterranean sea could identify micro-quasars in a few years of data taking, with the possibility of a 5σ level detection. In case of no observation, it would strongly constrain the neutrino production models and the source parameters.

1.4.2.4 Neutrinos from the Galactic Centre (GC)

The GC is specially appealing for a Mediterranean neutrino telescope since it is within the sky view of a telescope located at such latitude.

Early HESS observations of the GC region detected a point-like source at the gravitational centre of the Galaxy (HESS J1745-290 [38]) coincident with the supermassive

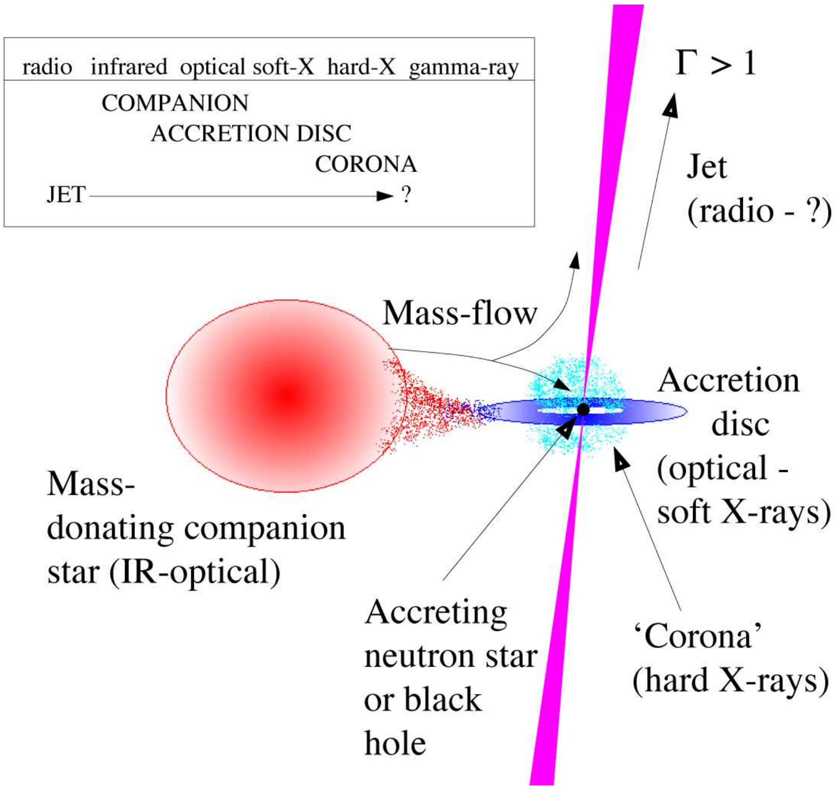

Figure 1.9: Sketch illustrating a micro-quasar. A compact object (neutron star or black hole) accretes material from a binary companion. The typical size of the accretion disk is $\sim 10^3$ km and the length of the jets is order of light years [37].

black hole Sagittarius A* and the SNR Sgr A East. In 2004, a more sensitive campaign revealed a second source, the PWN G 0.9+0.1 [39].

The measured γ-ray spectrum in the GC region is well described by a power law with index of ~ 2.3. The spectral index of the γ-rays, which closely traces back the spectral index of the CRs, indicates in the Galactic centre a local CR spectrum that is much harder and denser than that as measured at Earth. It is thus likely that an additional component to the CR population is present in the Galactic Centre, above the diffuse CR concentration which fills the whole Galaxy.

1.5 Diffuse ν fluxes and upper bound

The most direct way to prove the existence of the high energy neutrino sources described in the previous section is to perform a pointing search to individual sources. The possibility to detect point-like sources could be very small in detectors with a volume < 1 km^3, like ANTARES, even though some sources should generate guaranteed fluxes of neutrinos. Because of the very low ratio of events from individual sources, the measurement of the cumulative flux represented by extraterrestrial neutrinos from unresolved sources is a proper way to find the evidence of high energy neutrino sources. This is known as the diffuse neutrino flux and the main topic of this work is to study the ANTARES sensitivity to detect it and to search for diffuse neutrino events in the ANTARES collected data.

The search of diffuse neutrino events is performed without the use of any directional information; the only way to detect them is looking for an excess of high energy events in the energy spectrum. In fact, diffuse fluxes have a much harder spectrum than the atmospheric neutrino background.

The observation of diffuse flux of gamma-rays and of UHECRs can be used to set theoretical upper bounds on the total flux of neutrinos from extragalactic sources. High energy gamma-rays are produced in astrophysical acceleration sites by the decay of neutral pions. Neutrinos are produced in parallel from the decay of charged pions and they will escape from the source without further interactions, due to their low cross section. High energy photons from π^0 decay, on the contrary, will interact with the intergalactic radiation field, developing electromagnetic cascades. The energy of these γ-rays will be made available in the 1 MeV $\div$ 100 GeV range. Hence, the observable neutrino flux is limited by the observation of the gamma ray flux in this energy band, within a factor of two due to the branching ratios and kinematics at production.

The diffuse γ-ray background spectrum above 30 MeV was measured by the EGRET experiment as [40]:

$$E^2 I_\gamma(E) = (1.37 \pm 0.06) \times 10^{-6}\ [\mathrm{GeV\ cm^{-2}\ sr^{-1}\ s^{-1}}] \tag{1.7}$$

so the upper theoretical bound of the neutrino flux can be estimated to be of the same order of magnitude.

If nucleons escape from a cosmic source, a similar bound can be derived from the measured flux of CRs of extragalactic origin. Fermi acceleration mechanism can take place when protons are magnetically confined near the source. Neutrons produced by photo-production interactions of protons with radiation fields can escape from transparent sources and decay into cosmic protons outside the region of the magnetic field of the host accelerator.

Some additional factors have to be considered before establishing a relationship between CR and neutrino fluxes. These factors take into account the production kinematics, the opacity of the source to neutrons and the effect of propagation. Larger uncertainties are connected with the propagation factor, because it strongly depends on galactic evolution and on the poorly-known magnetic fields in the Universe. There is some controversy about how to use relationships to constrain the neutrino flux limit. Two of the most relevant predictions are described here.

1.5.1 The Waxman-Bachall upper bound

The upper bound proposed by Waxman and Bahcall (WB) [30; 31] takes the cosmic-ray observations at $E_{CR} \sim 10^{19}$ eV to constrain the neutrino flux. In the computation of the upper bound, several hypotheses are made: it is assumed that neutrinos are produced by interaction of protons with ambient radiation or matter; that the sources are transparent to high energy neutrons ($E_n \sim 10^{19}$ eV); that the 10^{19} eV CRs produced by neutron decay are not deflected by magnetic fields; finally (and most important) that the spectral shape of CRs up to the GZK cutoff is $\mathrm{d}N/\mathrm{d}E \propto E^{-2}$, as typically expected from the Fermi mechanism. The upper limit that they obtain is:

$$E_\nu^2 \frac{\mathrm{d}\Phi}{\mathrm{d}E_\nu} < 4.5 \times 10^{-8} \text{ GeV cm}^{-2} \text{ sr}^{-1} \text{ s}^{-1}. \tag{1.8}$$

Although this limit may be surpassed by hidden or optically thick sources for protons to $p\gamma$ or $pp(n)$ interactions, it represents the "reference" threshold to be reached by large volume neutrino detectors (Fig. 1.10).

1.5.2 The Mannheim-Protheroe-Rachen upper bound

The WB limit was criticised as not completely model independent. In particular, the main observation was about the choice of the spectral index $\alpha = 2$. The upper bound proposed by Mannheim et al. (MPR98) [41] was derived using as a constraint not only the CRs observed on Earth, but also the observed gamma-ray diffuse flux. The two cases of sources *opaque* or *transparent* to neutrons are considered; the intermediate case of source partially transparent to neutrons give intermediate limits.

The limit for sources *opaque* to neutrons is:

$$E_\nu^2 \frac{\mathrm{d}\Phi}{\mathrm{d}E_\nu} < 2 \times 10^{-6}\ \mathrm{GeV\ cm^{-2}\ sr^{-1}\ s^{-1}} \tag{1.9}$$

This is two orders of magnitude higher than the WB limit, because a source opaque to neutrons produces very few CRs (neutrons cannot escape and cannot decay outside the source), but it is transparent to neutrinos and γ-rays. This limit was already excluded in a wide energy range by the AMANDA-II experiment, as shown in Fig. 1.10.

The limit for sources *transparent* to neutrons decreases from the value of eq. 1.9 at $E_\nu \sim 10^6$ GeV to the value set by Waxman and Bahcall at $E_\nu \sim 10^9$ GeV. Above this energy, the limit increases again due to poor observational information.

The WB and the MPR limits for neutrino of one flavour are reported in Fig. 1.10. The original values are divided by two, to take into account the neutrino oscillations from the source to the Earth (see §1.6). Experimental upper limits are indicated as solid lines, IceCube 90% C.L. sensitivities for 3 years as dashed line. Frejus [42], MACRO [43], Amanda-II 2000-03 [44] limits refer to muon neutrinos. Baikal [45] and Amanda-II UHE 2000-02 [46] refer to neutrinos of all-flavours. In this case, the original upper limits are divided by three. Considering neutrino oscillations, a flux of cosmic neutrinos of all flavours is expected at Earth in the same proportion. The red line inside the shadowed band represents the Bartol [47] atmospheric neutrino flux. The lowest limit of the band represents the flux from the vertical direction, with a negligible contribution from prompt neutrinos, while the upper limit of the band represents the flux from the horizontal direction, with one of the prompt model which gives the maximum contribution [48].

1.6 The effect of neutrino oscillations

In recent years, neutrino oscillation became a well known phenomenon, which plays also an important role on determining the flavour on Earth of neutrinos of cosmic

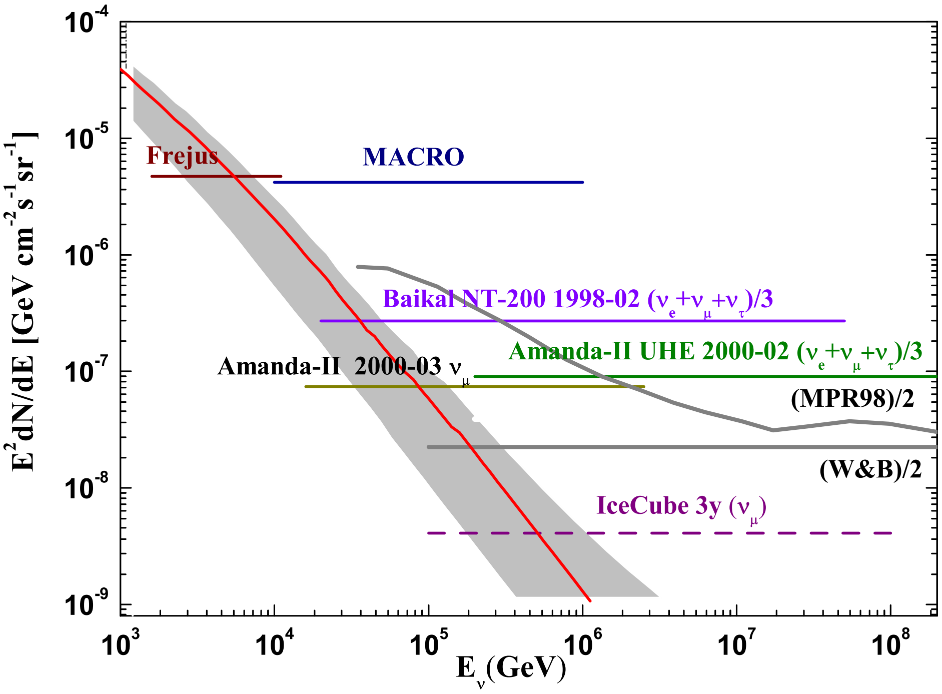

Figure 1.10: Sensitivities and upper limits for a E^{-2} diffuse flux of high energy neutrinos of one flavour. Experimental upper limits are indicated as solid lines, IceCube 90% C.L. sensitivities with dashed lines. Upper limits obtained from all-flavour analyses (Baikal and Amanda-II UHE 2000-02) are not directly comparable to the ν_μ upper limits. However, for the assumed astrophysical neutrino production models and for a wide range of neutrino oscillation parameters (§1.6), the flavour flux ratio at Earth can be assumed to be $\nu_e : \nu_\mu : \nu_\tau = 1 : 1 : 1$. In that case, either a single flavour limit can be multiplied by three (and compared to an all-flavour result) or an all-flavour limit can be divided by three and compared to a single-flavour result, as it is done in the figure. For reference, the WB and MPR98 limits for transparent sources are also shown. Both upper bounds are divided by two, to take into account the neutrino oscillation effects [16].

origin. Neutrino oscillations were observed in atmospheric neutrinos, in solar neutrino experiments and on Earth based accelerator and reactor experiments.

As already mentioned, high energy neutrinos are produced in astrophysical sources mainly through the decay of charged pions, in $p\gamma$, pp, pn interactions (eq. 1.6). Therefore, neutrino fluxes of different flavours are expected to be at the source in the ratio:

$$\nu_e : \nu_\mu : \nu_\tau = 1 \; : \; 2 \; : \; 0 \tag{1.10}$$

Due to the long distances between the source and the Earth, the flavours of the arriving neutrinos will be completely mixed:

$$\nu_e : \nu_\mu : \nu_\tau = 1 \; : \; 1 \; : \; 1 \tag{1.11}$$

Theoretical predictions which does not take into account neutrino oscillations must be corrected to include this effect. In particular, the predicted fluxes of muon neutrinos are reduced by a factor of two at Earth. This effect could not be so negative at very high energies, since it could allow the observation of electron and tau neutrinos.

Chapter 2

Neutrino detection principle

2.1 Neutrino interaction

The detection of high energy neutrinos is severely constrained by the fact that the expected fluxes and the neutrino interaction cross-sections are very low. Therefore, very large detectors are needed, typically $\sim$ GTon. Underground detectors would be too small, so the use of large volumes of sea/lake water or antarctic ice was proposed for the first time be M.A. Markov in 1960 [49].

The basic idea for a neutrino telescope is to build a matrix of light detectors inside a transparent medium. This medium, such as deep ice or water:

- offers large volume of free target for neutrino interactions;
- provides shielding against secondary particles produced by CRs;
- allows transmission of Cherenkov photons emitted by relativistic particles produced by the neutrino interaction.

The detection of acoustic or radio signals generated by EeV (10^{18} eV) neutrinos in a huge volume of water or ice has been also proposed [50; 51; 52].

High energy neutrinos interact with a nucleon N of the nucleus, via either charged current (CC) weak interactions

$$\nu_l + N \rightarrow l + X \tag{2.1}$$

or neutral current (NC) weak interactions

$$\nu_l + N \rightarrow \nu_l + X \ . \tag{2.2}$$

At energies of interest for neutrino astronomy, the leading order differential cross-section for the $\nu_l N \rightarrow lX$ CC interactions is given by [53]

$$\frac{\mathrm{d}^2\sigma_{\nu N}}{\mathrm{d}x\mathrm{d}y} = \frac{2G_F^2 m_N E_\nu}{\pi} \frac{M_W^4}{(Q^2 + M_W^2)^2}[xq(x,Q^2) + x(1-y)^2\overline{q}(x,Q^2)] \tag{2.3}$$

where Q^2 is the square of the momentum transferred between the neutrino and the lepton, m_N is the nucleon mass, M_W is the mass of the W boson, G_F is the Fermi coupling constant, and $q(x,Q^2)$ and $\overline{q}(x,Q^2)$ are the parton function distributions for quarks and antiquarks. The so-called scale variables or Fenyman-Bjorken variables are given by:

$$x = Q^2/2m_N(E_\nu - E_l) \tag{2.4}$$

and

$$y = (E_\nu - E_l)/E_\nu \tag{2.5}$$

Fig. 2.1 shows the ν_μ and $\overline{\nu}_\mu$ cross-sections as a function of the neutrino energy. As can be seen, at energies from 10^{10} to 10^{15} eV ($E_\nu \ll M_W^2/2m_N \approx 5$ TeV) the cross-section grows linearly with the energy as [54]:

$$\sigma_{\nu N} = (0.677 \pm 0.014) \times 10^{-38} \left(\frac{E_\nu}{1\ \mathrm{GeV}}\right) \mathrm{cm}^2 \tag{2.6}$$

$$\sigma_{\overline{\nu} N} = (0.334 \pm 0.008) \times 10^{-38} \left(\frac{E_\nu}{1\ \mathrm{GeV}}\right) \mathrm{cm}^2 \tag{2.7}$$

For higher energies, the invariant mass $Q^2 = 2m_N E_\nu xy$ could be larger than the W-boson rest mass, reducing the increase of the total cross-section. Since there is no data which constrain the structure functions at very small x, outside the range measured with high precision at the HERA collider, a 10% uncertainty is estimated on the total cross-section at $E_\nu \sim 100$ PeV [55]. From 10^{16} to 10^{21} eV it can be approximated as [56]:

$$\sigma_{\nu N} \simeq 5.53 \times 10^{-36} \left(\frac{E_\nu}{1\ \mathrm{GeV}}\right)^{0.363} \mathrm{cm}^2 \tag{2.8}$$

$$\sigma_{\overline{\nu} N} \simeq 5.52 \times 10^{-36} \left(\frac{E_\nu}{1\ \mathrm{GeV}}\right)^{0.363} \mathrm{cm}^2 \tag{2.9}$$

Computer libraries [57] provide a collection of parton distribution function (PDF) to model the neutrino cross-section also at very high energies.

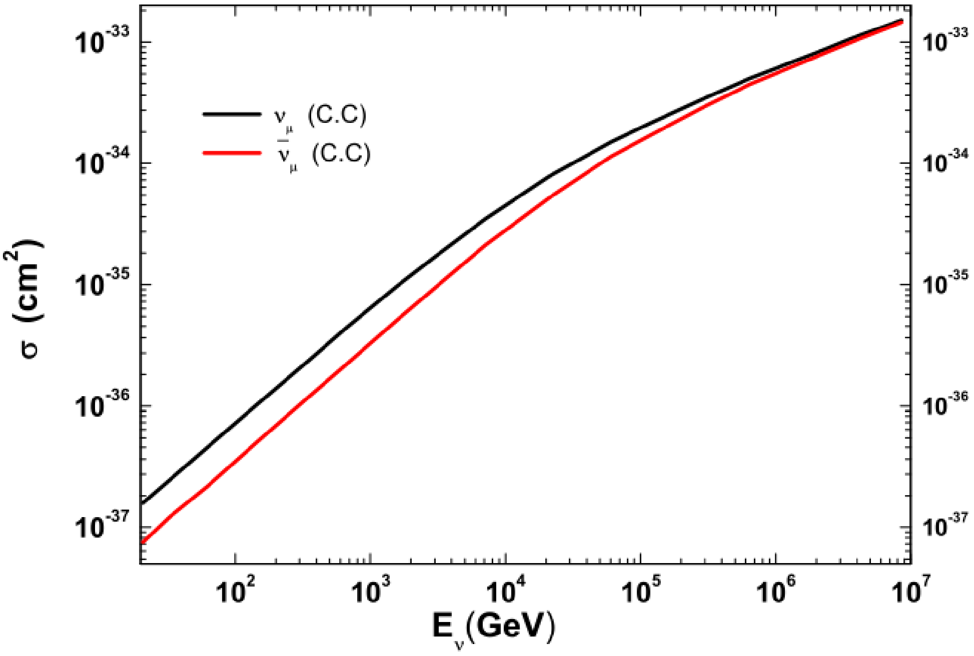

Figure 2.1: Cross-section for ν_μ and $\overline{\nu}_\mu$ as a function of the (anti)neutrino energy according to CTEQ6-DIS [55] parton distributions.

The increase of the interaction cross-section with the neutrino energy enlarges the effective volume of the detector. This effect is enhanced by the fact that the muon range also increases with the energy ($\sim$ 1 km at 300 GeV and $\sim$ 25 km at 1 PeV). Nevertheless, at very high energies ($>$ 1 PeV), the Earth becomes opaque to the neutrinos, and consequently the effective volume decreases.

Most of the tools to simulate these interactions are available within the CERNlib [58] package. For the Deep Inelastic Scattering (DIS) part of the neutrino interaction, the LEPTO [59] code provides the following facilities:

- Integration of the differential cross-sections over a specified kinematic range to give the total cross-section.
- Sampling of the kinematic properties of the outgoing muon from the differential cross-section.
- Hadronisation of the quark-gluon system in the target nucleus using the Lund string model via calls to the PYTHIA 5.7 / JETSET 7.4 package [60] to give the

initial particles in the hadronic shower.

This is done using a particular PDF, either taken from those built into LEPTO or via calls to the Parton Distribution Function library PDFlib 8.04 [61] for access to up-to-date calculations of PDFs using recent accelerator data.

Only the DIS contribution to the total cross-section is included in LEPTO. In DIS, the neutrino interacts with an individual parton within the nucleus to produce a muon. The inter-parton interactions only become important in the hadronisation of the coloured interaction products after the charged current exchange. The LEPTO code integrates the differential cross-section of eq. 2.3 over a specified range of the kinematic variables, giving a total cross-section for interactions within this kinematic range. LEPTO reproduces the published cross-sections and kinematics in Gandhi et al. [53] to better than 5% in the main region of interest.

The LEPTO code is accurate up to lepton energies of 10 TeV [59]. Above this energy, an extrapolation of the model to calculate the cross-section and kinematics is needed. The ANTARES software [62] contains an extrapolation for neutrino energies up to 10^8 GeV without running close to these limits.

The choice of PDF enters into both the cross-section and kinematics calculations via the quark distribution functions $q(x, Q^2)$. These PDFs are extracted from electron-proton collision data at HERA and fixed target experiments [63]. The ANTARES software uses the CTEQ6-D [64]. For high energy neutrino interactions, most neutrino interactions correspond to the low-x and high-Q^2 region of the kinematic phase space which is unfortunately the region of greatest uncertainty in the calculations and fitting of PDFs.

The dominant uncertainty from this section arises from the choice of PDF which affects the neutrino interaction cross-sections and the event kinematics in a non-trivial way. The effect of this, though relatively small in terms of the interaction cross-section below 1 PeV, cannot necessarily be neglected. Above 1 PeV, the uncertainty in the neutrino cross-section notably increases.

2.2 Muon neutrino detection

Muon neutrinos are especially interesting in a search for cosmic point sources of neutrinos with energies larger than ~ 1 TeV. In this energy range, the ν_μ interaction can occur outside the detector volume, while in most cases muons are energetic enough to completely traverse the detector. This gives a clean experimental signal which allows accurate reconstruction of muon direction, closely correlated with the neutrino direction.

The relation between neutrino and muon directions is essential for the concept of a neutrino telescope. Since neutrinos are not deflected by (extra-)galactic magnetic fields, it is possible to trace the muon back to the neutrino source. This is equivalent to traditional astronomy where photons point back to their source. The average angle $\theta_{\nu\mu}$ between the incident neutrino and the outgoing muon can be approximated by:

$$\theta_{\nu\mu} \leq \frac{0.6^o}{\sqrt{E_\nu[\mathrm{TeV}]}} \tag{2.10}$$

where E_ν is the neutrino energy expressed in TeV.

There are a number of different processes by which high energy muons lose energy as they propagate through matter (Fig. 2.2). The energy losses can be divided into the following categories [65]:

- **ionisation:** Muons traversing matter produce atomic excitations and ionizations. Ionisation is the dominant process of muon energy loss at low energies ($<$ 1 TeV). The energy transfer to the electrons is usually modest, but occasionally the electrons obtain a non-negligible fraction of the muon energy (δ-rays).

- **bremsstrahlung:** Charged particles emit radiation in the presence of an electromagnetic field giving rise to a deceleration. Concerning muon propagation in a dense medium, this deceleration is produced by the electromagnetic interaction with nuclei and electrons of surrounding atoms.

- **pair production:** An e^+e^- pair is produced. For muons with energy above $\sim$ 1 TeV is the dominant energy loss process.

- **photo-nuclear interactions:** Muons interact with an atomic nucleus through the exchange of a virtual photon.

The total energy loss by unit of length can be parametrized as:

$$-\left\langle \frac{\mathrm{d}E}{\mathrm{d}x} \right\rangle = \alpha(E) + \beta(E) \cdot E \tag{2.11}$$

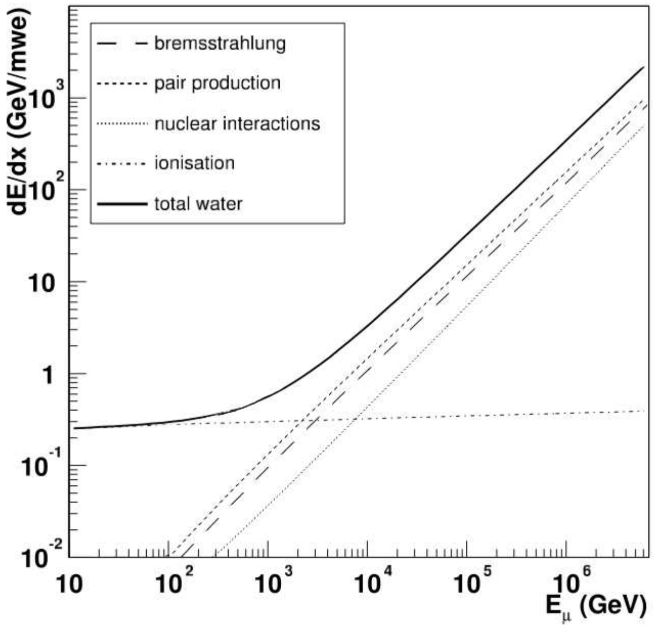

Figure 2.2: Average energy loss per meter of water equivalent (m.w.e.) for muons in sea water as a function of the muon energy. The contributions of the different processes are shown separately [66].

There is an almost constant term, $\alpha(E)$, due to ionisation and a term which grows linearly with the energy with slope $\beta(E)$ accounting for radiative loses. As a first approximation, they can be considered as energy independent. In water, $\alpha \simeq 2.67 \cdot 10^{-3}$ GeV g^{-1} cm^{-2} and $\beta \simeq 3.40 \cdot 10^{-6}$ g^{-1} cm^{-2}, for 30 GeV $< E_{\mu} <$ 35 TeV. The ionisation can be considered as a “continuos” process, while at high energy the muon loses energy via “stochastic” processes. This stochastic nature of radiative losses makes more difficult the muon energy reconstruction [67].

2.3 Cherenkov radiation

Any operating or proposed neutrino telescope in the TeV-PeV range is working by collecting the optical photons produced by the Cherenkov effect of charged relativistic particles. The light is collected by a three-dimensional array of photomultiplier tubes (PMTs). The information provided by the number of photons detected and their arrival times are used to infer the neutrino flavour, direction and energy.

Cherenkov radiation is emitted by charged particles crossing an insulator medium with speed exceeding that of light in the medium [68]. The charged particle polarises the molecules along the particle trajectory, but only when the particle moves faster than the speed of light in the medium, an overall dipole moment is present. Light is emitted when the electrons of the insulator restore themselves to equilibrium after the disruption has passed, creating a coherent radiation emitted in a cone with a characteristic angle θ_C given by

$$cos\theta_C = \frac{c/n}{\beta c} = \frac{1}{\beta n} \tag{2.12}$$

where n is the refracting index of the medium and β is the particle speed in units of c. For relativistic particles ($\beta \simeq 1$) in seawater ($n \simeq 1.364$) the Cherenkov angle is $\theta_C \simeq 43^o$.

The number of Cherenkov photons, N_γ, emitted per unit wavelength interval, $d\lambda$ and unit distance travelled, dx, by a charged particle of charge e is given by

$$\frac{d^2N}{dxd\lambda} = \frac{2\pi}{137\lambda^2}(1 - \frac{1}{n^2\beta^2}) \tag{2.13}$$

where λ is the wavelength of the radiation. From this formula it can be seen that the Cherenkov radiation gives a significant contribution at shorter wavelengths. Typically, in the wavelength range between 300-600 nm, the number of Cherenkov photons emitted per meter is about 3.5×10^4.

2.4 Physical background

Cosmic neutrino detectors are not background free. Showers induced by interactions of cosmic rays with the Earth's atmosphere produce the so-called *atmospheric muons* and *atmospheric neutrinos*. Atmospheric muons can penetrate the atmosphere and up to several kilometres of ice/water. Neutrino detectors must be located deeply under a large amount of shielding in order to reduce the background. The flux of down-going atmospheric muons exceeds the flux induced by atmospheric neutrino interactions by many orders of magnitude, decreasing with increasing detector depth, as is shown in Fig. 2.3. The previous generation of experiments which had looked also for astrophysical neutrinos (MACRO [69], Super-Kamiokande [70]) was located under mountains, and has reached almost the maximum possible size for underground detectors.

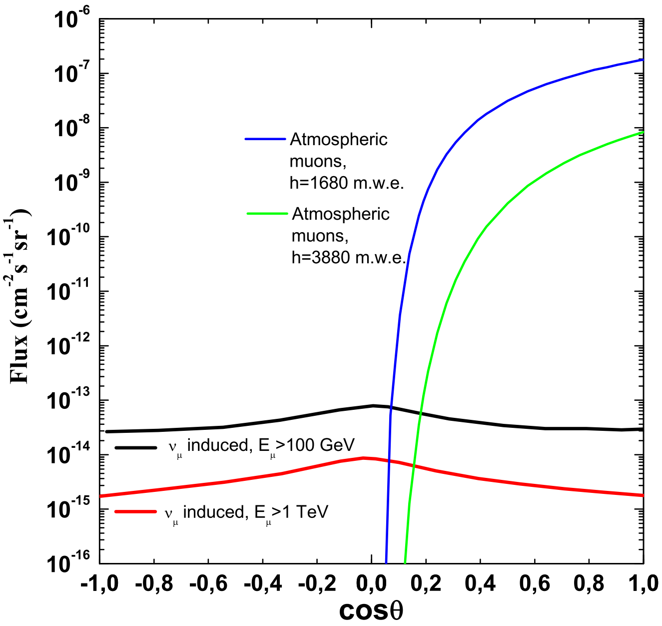

Figure 2.3: Different contributions (as a function of the cosine of the zenith angle) of the atmospheric muons (computed according to [71]) for two different depths; and of the atmospheric neutrino induced muons (from [47]), for two different muon energy thresholds.

Fig. 2.4 shows the reconstructed zenith angle of ANTARES data compared with MonteCarlo, from an analysis of 2007 data with 5 lines and an analysis of 2008 data with 9-12 lines. In the region of downward going events the contribution of atmospheric muons dominates over the atmospheric neutrinos.

Charged particles travel through the medium until they either decay or interact. The mean length of the distance travelled is called the *path length* of the particle and it depends on its energy loss in the medium. If the path length exceeds the spatial resolution of the detector, so that the trajectory of the particle can be resolved, one have a *track*. In a high energy neutrino detector, one can distinguish between two main event classes: events with a track, and events without a track (showers).

In order to behave as a neutrino *telescope*, a neutrino *detector* must be able to point at a specific celestial region if a signal excess over the background is found. Neutrino telescopes must have the same peculiarities of GeV-TeV γ-ray experiments (satellites, imaging Cherenkov) to associate some of the signal excesses to objects known in other electromagnetic bands. In order to achieve an angular resolution of a fraction of degree,

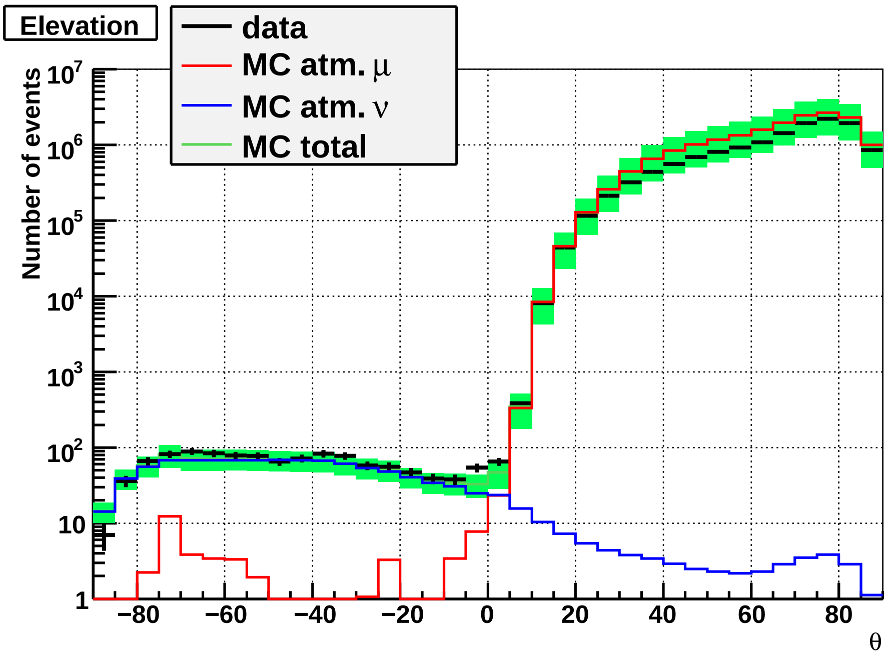

Figure 2.4: Reconstructed zenith angle of ANTARES data compared with MonteCarlo. The convention used here is $\theta = 90°$ vertically downward going events and $\theta = -90°$ vertically upward going events. The plot combines the results from an analysis of 2007 data with 5 lines and an analysis of 2008 data with 9-12 lines and corresponds to 341 days of detector livetime. The atmospheric (anti)neutrino MC sample is weighted according to the Bartol flux [47]; the atmospheric muons are simulated with CORSIKA [72] using Hörandel fluxes [73]. Data are black points, atmospheric muons red and atmospheric neutrinos blue. The total numbers for the upward going events ($\theta < 0$) are 1062 in data, 916 from atmospheric neutrinos and 40 from atmospheric muons. The error band of the "total MC" curve takes for neutrinos a combined theoretical and systematic error of 30% and for atmospheric muons of 50% [74].

only the CC ν_μ interaction can be used. The angular resolution for other flavours and for NC is so poor that there is no possibility to perform associations. For the same reason, the particle physics and general physics open questions which can be covered with a neutrino telescope largely rely on the ν_μ channel.

On the other hand, a high energy neutrino detector is motivated by discovery and must be designed to detect neutrinos of all flavours over a wide energy range and with the best energy resolution. This is of particular interest for the case of the neutrino diffuse flux from extragalactic sources. In addition, the neutrino oscillation changes the source admixture from $\nu_e : \nu_\mu : \nu_\tau = 1 : 2 : 0$ to $1 : 1 : 1$. While above hundreds of TeV muon and electron neutrinos become absorbed by the Earth, the tau neutrino is *regenerated* [75]: high energy ν_τ will produce a secondary ν_τ of lower energy, lowering its energy down to 10^{15} eV, where the Earth is transparent.

Neutrino telescopes, contrary to usual optical telescopes, are "looking downward". Up-going muons can only be produced by interactions of (up-going) neutrinos. From the bottom hemisphere, the neutrino signal is almost background-free. Only atmospheric neutrinos that have traversed the Earth, represent the irreducible background for the study of cosmic neutrinos. The rejection of this background depends upon the pointing capability of the telescope and its possibility to estimate the parent neutrino energy.

2.5 Electron and tau neutrino detection

Schematic views of a ν_e, ν_μ and ν_τ CC events and of a NC event are shown in Fig. 2.5. Neutrino and anti-neutrino reactions are not distinguishable; thus, no separation between particles and anti-particles can be made. Showers occur in all event categories shown in Figure. However, for CC ν_μ, often only the muon track is detected, as the path length of a muon in water exceeds that of a shower by more than 3 orders of magnitude for energies above 2 TeV. In this section, a brief review concerning the detection of electron and tau neutrinos is given.

2.5.1 Electron neutrino interactions

A high energy electron resulting from a charged current ν_e interaction has a high probability to radiate a photon via bremsstrahlung after few tens of cm of water/ice (the water radiation length is ~ 36 cm). The following process of e^+e^- pair productions, and subsequent bremsstrahlung, rapidly produce an electromagnetic (EM) shower until the energy of the constituents falls below the critical energy E_c and the shower production stops; the remaining energy is then dissipated by ionisation and excitation.

The EM shower is described by the longitudinal shower profile (a parametric formula is given in [54]). The longitudinal profiles are used to parameterise the total shower length L as a function of the initial shower energy. The shower length is defined as the distance within which 95% of the total shower energy has been deposited. For a 10 TeV electron traveling in salt water it is found that L_{shower} is 7.4 meter.

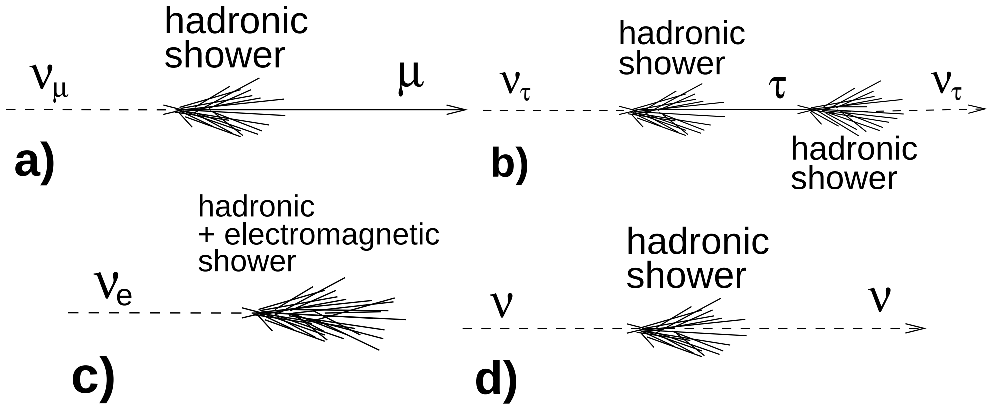

Figure 2.5: Some event signature topologies for different neutrino flavours and interactions: a) CC interaction of a ν_μ produces a muon and a hadronic shower; b) CC interaction of a ν_τ produces a τ that decays into a ν_τ, tracing the double bang event signature. c) CC interaction of ν_e produces both an EM and a hadronic shower; d) a NC interaction produces a hadronic shower. Particles and anti-particles cannot be distinguish in neutrino telescopes. From [76]

A showers length of the order of 10 m is small compared to the spacing of the PMTs in any existing or proposed detector. EM showers represent, to a good approximation, a point source of Cherenkov photons. Pointing accuracy for showers is inferior to that can be achieved for the ν_μ channel. Reconstruction of Monte Carlo simulated events performed in the framework of the IceCube and ANTARES collaborations shows a precision of the order of $\sim 10^\circ$, with the possibility to reduce it to few degrees for a small subsample of events.

2.5.2 Neutral currents interactions

The NC channel gives the same signature for all neutrino flavours. In this channel, a part of the interaction energy is always carried away unobserved by the outgoing neutrino, and therefore the error on the reconstructed energy of the primary neutrino increases accordingly. Even though EM and hadronic showers are different from each other in principle, the ν_e CC and the ν_x NC channels are not distinguishable in reality, because any proposed detector is too sparsely instrumented.

The dominant secondary particles in a hadronic shower are pions; kaons, protons or neutrons occur in variable fractions. Muons (from pions decay) can be present as well: they usually leave the shower producing long tracks.

Monte Carlo simulations (for instance, from the ANTARES collaboration [77]) shows that above 1 TeV of shower energy, the largest part of the Cherenkov light is generated by EM sub-showers. For what concerns the measurement of the incoming neutrino direction, the angular difference between the shower and the neutrino falls below 2^o for E_ν above $\sim$ 1 TeV. It is thus negligible with respect to the precision of the shower direction measurement.

2.6 Tau neutrino detection

For ν_τ CC interactions, the produced τ-lepton travels some distance (depending on its energy) before it decays and produces a second shower. The Cherenkov light emitted by the charged particles in the showers can be detected if both the ν_τ interaction and the τ decay occur inside the instrumented volume of the detector. Below 1 PeV, also the ν_τ CC channels (except for the case where the τ produces a muon) belong to the class of events without a track, because the τ track cannot be resolved.

The τ lepton has a short lifetime, and in the energy range of interest it travels from a few meters up to a few kilometres before it decays. Thus, if the track of the τ is long enough to distinguish between the primary interaction of the ν_τ and the decay of the tau (typically for τ energies above 1 PeV), the expected signatures for the ν_τ CC events are that of a shower, plus a track, plus another shower. This signature is called *double bang event*, if the Cherenkov light emitted by the charged particles in the first shower can be detected and separated from the light emitted by the particles produced in the τ decay.

Alternatively, if the τ starts or ends outside the instrumented volume, a track plus a shower can be detected. This signature is called *lollipop event*. In small size neutrino detectors (like ANTARES) the expected *lollipop* event rate above 1 PeV is far below 1 event per year. For larger detectors (IceCube or the 1 km^3 Mediterranean sea telescope) the optimal ν_τ energy value for *double bang* events is around $\sim 10^{16}$ eV, because the tau path length rapidly exceeds the dimensions of the detectors for increasing energies. If the τ decays into a muon, the event is presumably not distinguishable from an original ν_μ CC interaction.

Chapter 3

The ANTARES neutrino telescope

ANTARES (Astronomy with a Neutrino Telescope and Abyss environmental RESearch) is at present the largest Cherenkov neutrino observatory in the Northern hemisphere [78]. It is a project which involves today about 200 physicists, engineers and sea-science experts from 29 institutes of 7 European countries. The detector explores the Southern sky hemisphere, which represents the most interesting area of the sky due to the presence of the Galactic Centre, where neutrino source candidates are expected. ANTARES will contribute in the search for astrophysical neutrinos with a sensitivity much better than any other previous experiment.

3.1 The ANTARES detector

The ANTARES project has been set up in 1996 [79]. The first detector line was connected in March 2006 [80]. The ANTARES detector was completed on 29 May 2008 making it the largest Neutrino Telescope in the northern hemisphere and the first to operate in the deep sea. The technological developments made for ANTARES has extensively built on the experience of the pioneer DUMAND [81] project as well as the successful Baikal [82] detector in Siberia. Some of the aspects of the ANTARES design have common features with the AMANDA/ICECUBE detector at the South Pole. Recently, a method for the measurement of the muon flux in the ANTARES telescope has been published in [83].

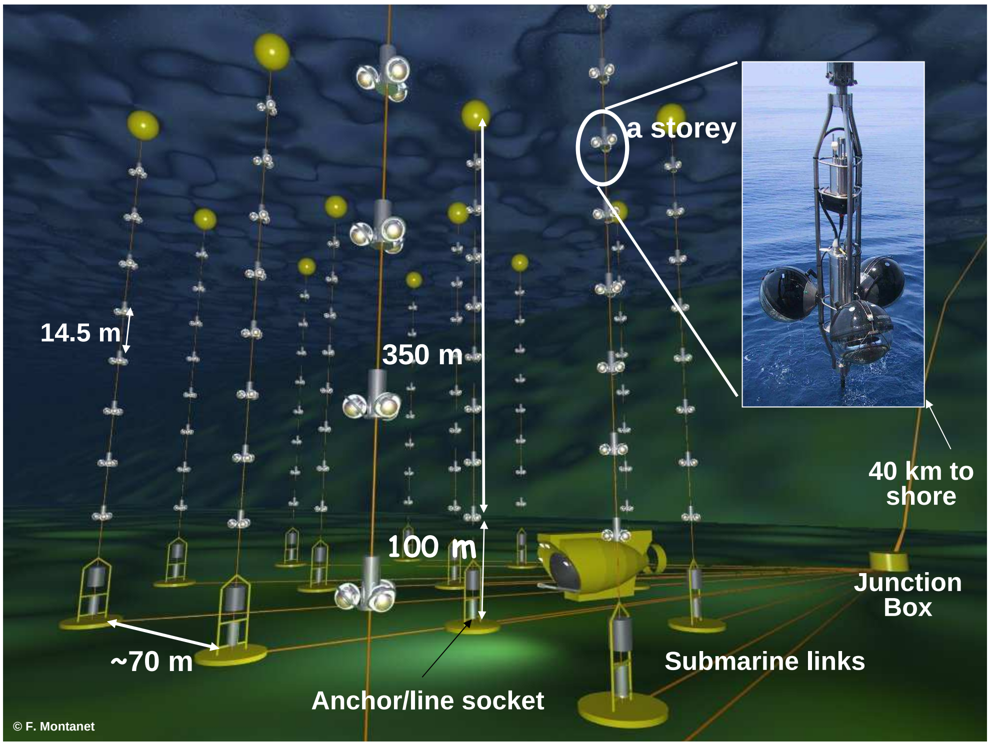

Figure 3.1: Schematic view of the ANTARES detector

The ANTARES detector is located at a depth of 2475 m in the Mediterranean Sea, 42 km from La Seyne-sur-Mer in the South of France. A schematic view of the detector layout is shown in Fig. 3.1. The infrastructure has 12 mooring lines holding light detectors designed for the measurement of neutrinos based on detection of the Cherenkov light emitted in water. The Neutrino Telescope extends the reach of neutrino astronomy in a complementary region of the universe to the South Pole experiments, in particular in the region of our galaxy. Further, by its location in the deep sea the infrastructure provides opportunities for innovative measurements in Earth and Sea Science. An essential feature of the infrastructure is the permanent connection to the shore with the capacity for high-bandwidth acquisition of data, providing the opportunity to install sensors for sea parameters giving continuous long term measurements. Such data is currently non-existent and the novel potential will create opportunities for discoveries and innovation in many sea science areas. Instruments for research in marine and Earth science are distributed on the 12 optical detector lines and are also located on a further 13th line specifically dedicated to monitoring of the sea environment.

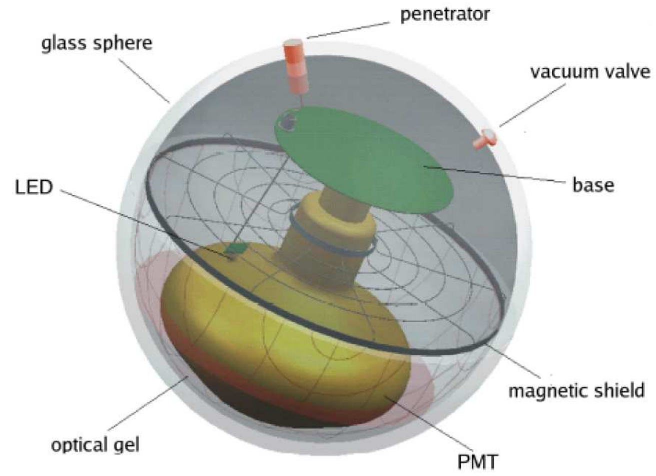

Figure 3.2: Schematic view of the OM of ANTARES

3.1.1 Detector Layout

The elementary detection unit is the Optical Module (OM) (Fig. 3.2) which consists of a glass sphere housing a photo-multiplier tube (PMT) [84]. The three-dimensional telescope matrix is made of groups of three OMs called storeys. Three OMs are mounted in the Optical Module Frame (OMF), a mechanical structure which also supports a titanium container, the Local Control Module (LCM), housing the offshore electronics and processors. A detector line is formed by a chain of 25 OMF linked by Electro-Mechanical Cable segments(EMC), 12.5 m long from storey to storey and 100 m long from the bottom to the first storey. The line is anchored on the sea bed with the Bottom String Socket (BSS) and is held vertical by a buoy at the top. The full neutrino telescope has 12 such lines arranged on the sea bed in an octagonal configuration (Fig. 3.3).

The data and the power are transmitted between the detector lines and the shore via an infrastructure on the sea bed which consists of the Junction Box (JB), the Main Electro-Optical Cable (MEOC) and Inter Link cables (IL). Onshore, the data arrive in PC farm located at the Shore Station (near Toulon, France) where the ANTARES control room is situated. The treatment includes filtering, triggering and communication with a data base. Data is stored remotely at a computer centre in Lyon.

The 13th additional line (IL07) contains an ensemble of oceanographic sensors for the dedicated measurement of environmental parameters. The twelfth line and the IL07

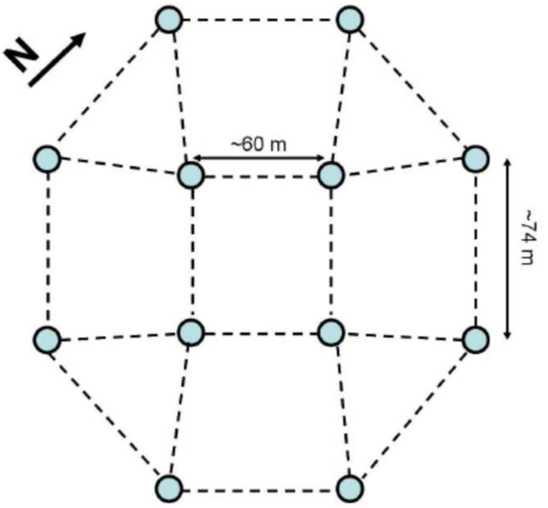

Figure 3.3: Layout of the detector shape. Each dot represents a line which is placed inside an octagonal shape.

also includes hydrophone-only storeys dedicated to the study of the ambient acoustic backgrounds.

3.1.2 Positioning system and Master Clock system

Each of the ANTARES 12 detector lines are anchored to the seabed and pulled taught by the buoyancy of the individual OMs and a top buoy. Due to the flexible nature of these detector lines, even a relatively small water current velocity of 5 cm/s can result in the top storeys being displaced by several meters from the vertical (Fig. 3.4). Therefore, real time positioning of each line is needed. This is achieved through two independent systems: an acoustic positioning system and a lattice of tiltmeters-compasses sensors. The shape of each line is reconstructed by performing a global χ^2 fit using information from both of these systems. The relative positions of each individual OM is then calculated from this line fit using the known geometry of each individual storey.

Precise timing resolution on the recorded PMT signals, of the order of 1 ns, is required to maintain the angular resolution of the telescope. An essential element to achieve this precision is a master clock system, based onshore, which delivers a common reference time to all the offshore electronics in the LCMs. This system delivers a time stamp, which is derived from GPS time, via a fibre optic network from the shore station

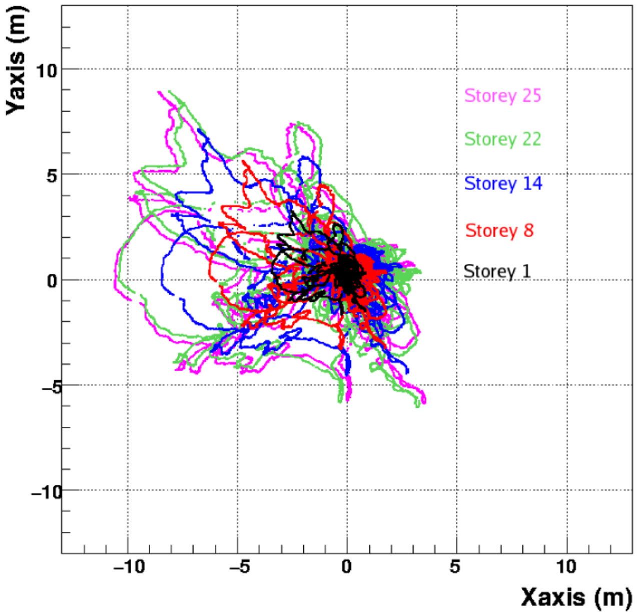

Figure 3.4: The horizontal movements measured with all hydrophones on Line 11 for a 6 month period. The dominant East-West heading of the line movements is due to the dominant Ligurian current which flows at the ANTARES site [85].

to the junction box, then to each line base and each LCM. This system, working at 20 MHz clock, is self calibrating and continually measures the time path from shore to the LCM by echoing signals received in the LCM back to the shore station.

3.2 Site evaluation

During the R&D phase of the experiment an extensive measurement program on the detector site has been carried out in order to evaluate some environmental parameters and the optical water properties. This section reviews the most relevant results concerning the water optical properties, the biofouling, the sedimentation and the optical background.

3.2.1 Water optical properties

The effects of the medium (water or ice) on light propagation are absorption and scattering of photons. These affect the reconstruction capabilities of the telescope.

In fact, absorption reduces the amplitude of the Cherenkov wavefront, i.e. the total amount of light on PMTs. Scattering changes the direction of propagation of the Cherenkov photons and the distribution of their arrival time on the PMTs; this degrades the measurement of the direction of the incoming neutrino. We define *direct photons* those which arrive on a PMT in the Cherenkov wavefront, without scattering; otherwise, we define them *indirect photons*.

The propagation of light in a transparent medium is quantified for a given wavelength λ, by the medium inherent optical properties: absorption $a(\lambda)$, scattering $b(\lambda)$ and attenuation $c(\lambda) = a(\lambda) + b(\lambda)$ coefficients, or, alternately, absorption $L_a(\lambda) = a(\lambda)^{-1}$, scattering $L_b(\lambda) = b(\lambda)^{-1}$ and attenuation $L_c(\lambda) = c(\lambda)^{-1}$ lengths. Each of these lengths represents the path after which a beam of initial intensity I_0 and wavelength λ is reduced in intensity by a factor of 1/e through absorption and scattering, according to the following relation:

$$I_i(x, \lambda) = I_0(\lambda) e^{-x/L_i(\lambda)}; \quad i = a, b, c \tag{3.1}$$

where x (in meters) is the optical path traversed by the light.

The effective attenuation length was measured in the ANTARES site using a collimated and a continuous LED source located at different distances from the optical module. The measured value for wavelength $\lambda = 466$ nm is [86]:

$$L_c(\lambda = 460 \text{ nm}) = 41 \pm 1_{stat} \pm 1_{syst} \text{ m} \tag{3.2}$$

The absorption and scattering lengths were measured separately using different experimental setups. A set of measurements has been recorded at different periods of the year and is shown in Fig. 3.5.

3.2.2 Biofouling and sedimentation

The detector elements are exposed to particle sedimentation and adherence of bacteria (biofouling) which reduce the light transmission through the glass sphere of the OMs. These effects on the ANTARES optical modules have been studied in [87].

The experimental setup consisted in two resistant glass spheres similar to those used for the OMs. One of them was equipped with five photo-detectors glued to the inner surface of the sphere at different inclinations (zenith angles θ) which were illuminated by two blue light LEDs contained in the second sphere. The measurements went on

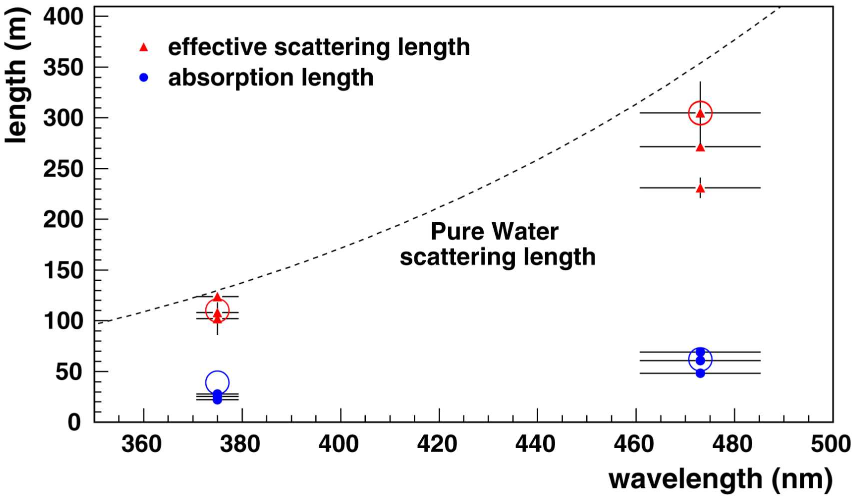

Figure 3.5: Absorption (dots) and effective scattering (triangles) lengths measured at the ANTARES site at various epochs for UV and blue data. Horizontal error bars illustrate the source spectral resolution. The large circles are estimates of the absorption and scattering lengths in pure sea water. The dashed curve is the scattering length for pure water, upper limit on the effective scattering length in sea water [86].

during immersions of several months and extrapolated to longer periods of time. In Fig. 3.6 is shown the light transmission as a function of immersion time for the the five photo-diodes. As can be expected there is a tendency in the fouling to decrease when the zenith angle on the glass sphere increases. After 8 months of operation, the loss of transparency in the equatorial region of the OM dropped only $\simeq 2.7\%$ and then it seems to saturate. Extrapolations indicate a global loss after 1 year of $\simeq 2\%$ (taking into account the two glass spheres used in the setup). Taking into account that the PMTs of ANTARES point 45°downward (zenith angle of 135°), the biofouling and the sedimentation do not represent a major problem for the experiment.

3.2.3 Optical background in sea water

The background in seawater has two main natural contributions: the decay of radioactive elements in water, and the luminescence produced by organisms, the so-called bioluminescence.

The ^{40}K is by far the dominant of all radioactive isotopes present in natural seawa-

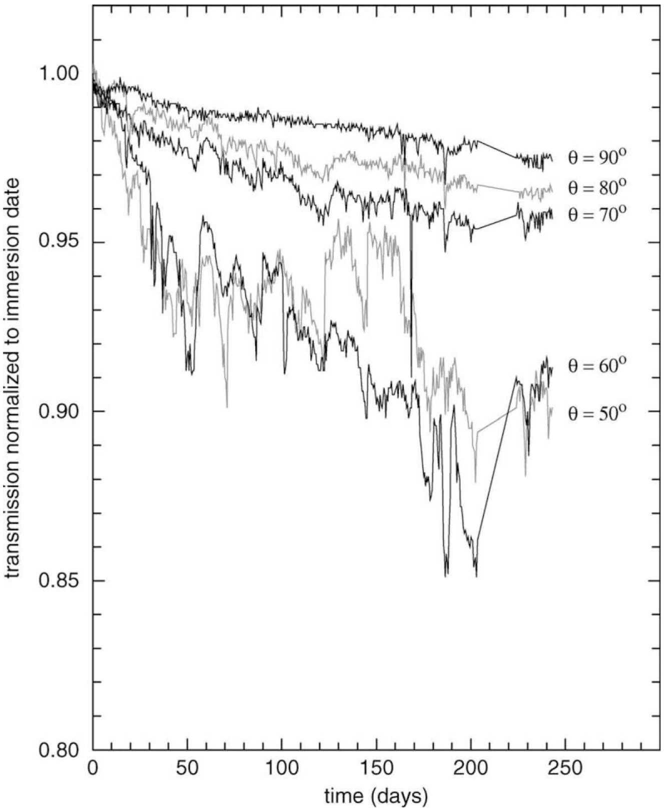

Figure 3.6: Light transmission as a function of time obtained from the immersion of the two glass spheres (see text for details). The measurements for each of the five photodiodes are normalised to unity at immersion day. Curves are labeled according to the photodiode zenith angle θ [87].

ter. The ^{40}K decay channels are:

$$\begin{aligned} ^{40}K &\rightarrow {}^{40}Ca + e^- + \bar{\nu}_e \text{ (BR = 80.3\%)} \\ ^{40}K + e^- &\rightarrow {}^{40}Ar + \nu_e + \gamma \text{ (BR = 10.7\%)} \end{aligned} \quad (3.3)$$

and both contribute to the production of optical noise. A large fraction of electrons produced in the first decay is above the threshold for Cherenkov light production. The photon originating in the second reaction has an energy of 1.46 MeV and can therefore lead (through Compton scattering) to electrons above the Cherenkov threshold.

The intensity of Cherenkov light from ^{40}K radioactive decays depends mostly on the ^{40}K concentration in sea water. Since salinity in the Mediterranean Sea has small geographical variation, this Cherenkov light intensity is largely site independent.

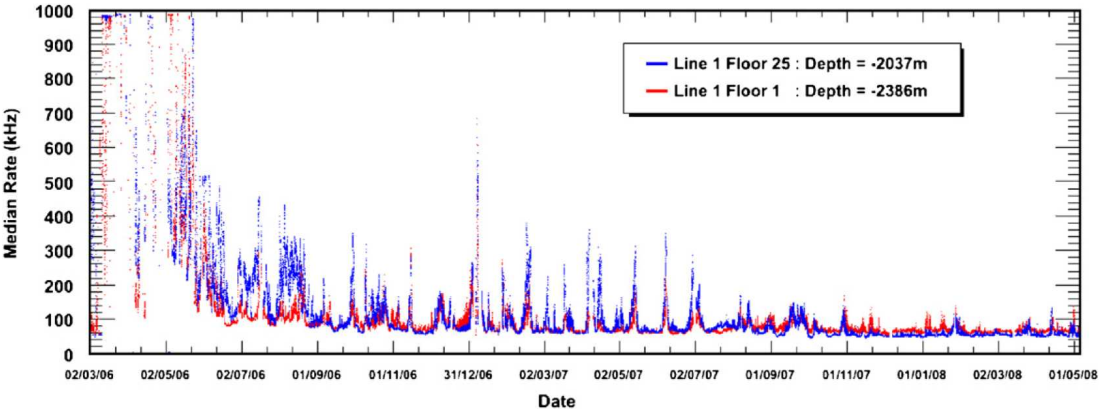

Figure 3.7: Median rates (in kHz) measured with the 10" PMTs of the ANTARES experiment, on optical modules at two different depths (2037 m and 2386 m). Data from March 2006 up to May 2008 [88]. The contribution of the ^{40}K decay is evaluated to be almost constant to $\sim 30 \div 40$ kHz.

Bioluminescence is found everywhere in oceans and there are two sources in deep sea: steady glow of bacteria and flashes produced by marine animals. These can give rise to an optical background up to several orders of magnitude more intense than the one due to ^{40}K (see Fig. 3.7). The two components of optical background described above are clearly visible. Bursts observed in the counting rates are probably due to the passage of light emitting organisms close to the detector.

Deep sea currents were monitored at the ANTARES, NEMO and Nestor sites for long time periods. ANTARES discovered that the baseline component is neither correlated with sea current, nor with burst frequency; however, long-term variations of the baseline were observed. Periods of high burst activity are not correlated with variations of the baseline component, suggesting that each of the two contributions is caused by a different population. Moreover, a strong correlation is observed between bioluminescence phenomena and the sea current velocity, as shown in Fig. 3.8.

3.3 Data acquisition system

The Data acquisition (DAQ) system of ANTARES is extensively described in [89]. The full-custom Analogue Ring Sampler (ARS) has been developed to perform the complex front-end operations [90]. This chip samples the PMT signal continuously at a tuneable

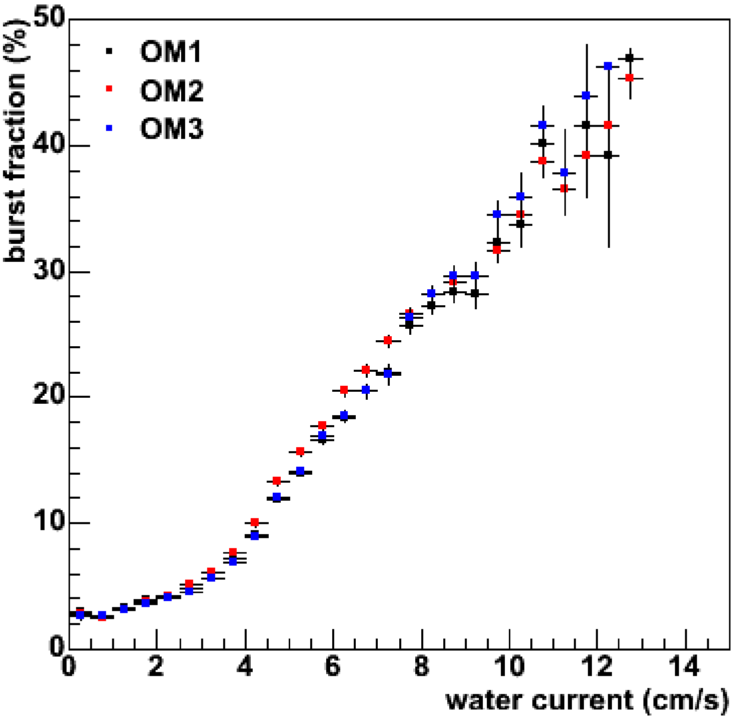

Figure 3.8: Correlation between the burst fraction and the seawater current velocity as measured by the ANTARES detector. The burst fraction is the fraction of time with count rates on OMs exceeding 120% of the baseline rate [16].

frequency up to 1 GHz and holds the analogue information on 128 switched capacitors when a threshold level is crossed. The information is then digitised, in response to a trigger signal, by means of two integrated dual 8-bit ADC. Optionally the dynamic range may be increased by sampling the signal from the last dynode. A 20 MHz reference clock is used for time stamping the signals. A Time to Voltage Converter (TVC) device is used for high-resolution time measurements between clock pulses. The ARS is also capable of discriminating between simple pulses due to conversion of single photoelectrons (SPE) from more complex waveforms. The criteria used to discriminate between the two classes are based on the amplitude of the signal, the time above threshold and the occurrence of multiple peaks within a time gate. Only the charge and time information is recorded for SPE events, while a full waveform analysis is performed for all other events. The ARS chips are arranged on a motherboard to serve the optical modules. Two ARS chips, in a “token ring” configuration, perform the charge and time information of a single PMT. A third chip on each board is used for triggering purposes. The settings of each individual chip can be remotely configured from the shore.

On each OM, the counting rates exhibit a baseline dominated by optical background due to sea-water ^{40}K decay and bioluminescence coming from bacteria, as well as bursts of a few seconds duration, probably produced by bioluminescent emission of macro-organisms. Fig. 3.7 shows the counting rates recorded by two OMs located on different storeys during the 2006-2008 runs. The average counting rate increases from the bottom to shallower layers. The baseline is normally between 50 to 80 kHz.

Differently from the ^{40}K background, bioluminescence suffers from seasonal and annual variations, see Fig. 3.7. There can be large variations of the rate, reaching hundreds of kHz in some periods. Since September 2006 to December 2008 the mean counting rate was 75% of the time below 100 kHz. A safeguard against bioluminescence burst is applied online by means of a high rate veto, most often set to 250 kHz.

The OMs deliver their data in real time and can be remotely controlled through a Gb Ethernet network. Every storey is equipped with a Local Control Module (LCM) which contains the electronic boards for the OM signal processing, the instrument readout, the acoustic positioning, the power system and the data transmission. Every five storeys the Master Local Control Module also contains an Ethernet switch board, which multiplexes the DAQ channels from the other storeys. At the bottom of each line, the Bottom String Socket is equipped with a String Control Module which contains local readout and DAQ electronics, as well as the power system for the whole line. Both the Master Local Control Modules and the String Control Modules include a Dense Wavelength Division Multiplexing (DWDM) system. The DWDM is used in data transmission to merge several 1Gb/s Ethernet channels on the same pair of optical fibres, using different laser wavelengths. The lines are linked to the junction box by electro-optical cables which were connected using an unmanned submarine. A standard deep sea telecommunication cable links the junction box with a shore station where the data are filtered and recorded.

All OMs are continuously read out and digitised informations (*hits*) sent to shore. In ANTARES, a *hit* is a digitised PMT signal above the ARS threshold, set around 1/3 of the single photoelectron level (Level 0 hits, L0). On-shore, a dedicated computer farm performs a global selection of hits looking for interesting physics events (DataFilter).

This on-shore handling of all raw data is the main challenge of the ANTARES DAQ system, because of the high background rates. The data output rate is from 0.3 GB/s to 1 GB/s, depending on background and on the number of active strings. Particular conditions define a subset of L0 for triggering purpose. This subset (called Level 1 hits, or simply L1) corresponds either to coincidences of L0 on the same OM triplet of a storey within 20 ns, or to a single high amplitude L0 (typically $>$ 3 p.e.). The DataFilter processes all data online and looks for a physics event by searching a set of correlated L1 hits on the full detector in a $\sim 4\ \mu s$ window. In case an event is found, all L0 hits of the full detector during the time window are written on disk, otherwise the hits are thrown away.

The trigger rate is between 1 to 10 Hz, depending on the number of strings in data acquisition. Most of the triggered events are due to atmospheric muons, successively reconstructed by track-finding algorithms. If ANTARES receives external GRB alerts [89], all the activity of the detector is recorded for few minutes. In addition, un-triggered data runs are collected on a weekly base. This un-triggered data subset is used to monitor the relative PMT efficiencies, as well as to check the timing within a storey, using the ^{40}K activity.

Chapter 4

MonteCarlo simulation and analysis tools

In this chapter the software tools used in this work are described. These programs have been developed by the ANTARES collaboration to reproduce the physical processes and the detector response. The main simulation steps are: the event generation, the particle propagation, the trigger and electronic simulations. At the end of this process, both MonteCarlo (MC) and real data can be considered to have the same structure. Hence the last step is the reconstruction of events, that is applied both on simulated and real data.

The event generators and the MC samples generated to reproduce signal and background events will be described in detail in this chapter. Two kinds of physics events have been generated: upward going (*upgoing*) neutrino events to simulate both the astrophysical signal and the atmospheric neutrino background, and downward going (*downgoing*) atmospheric muons.

4.1 Software packages for ν simulation

To study the performance of the ANTARES detector in detail and predict its response to a range of different neutrino sources, two distinct stages of simulation are required. Firstly, it is necessary to accurately model the interaction of neutrinos in the media in and around the instrumented volume of the detector and propagate the resulting particles until they are at a detectable distance from the PMTs. Secondly, the re-

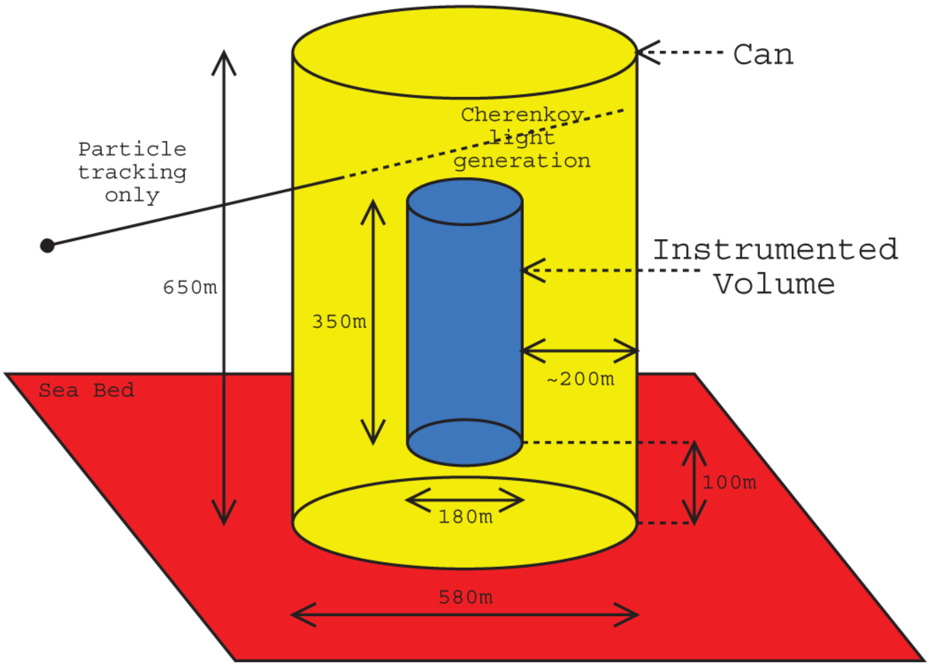

Figure 4.1: Definition of the ANTARES can. The can is built by extending the instrumented volume by three attenuation lengths (~200 m), except from below where it is bounded by the sea bed from which no Cherenkov light can emerge. If the interaction vertex is outside the can, only the muon is propagated up to the can surface, since the Cherenkov light produced by the other particles would not reach the detector [91].

sponse of the detector to the Cherenkov light produced by these particles within the instrumented volume must be determined.

4.1.1 Simulation overview and generation requirements

For the purposes of generating neutrino interactions, we treat the instrumented volume of the detector as a cylinder which contains all the PMTs. Surrounding this volume is a larger cylinder, which is called the “can”. The can defines the volume within which Cherenkov light is generated in the detector MonteCarlo (§4.3) to determine the detector response. Outside this volume, only particle energy losses in propagation are considered. Inside it, a full simulation including the generation of Cherenkov light must be performed. The geometry of this simulation scheme is shown in Fig. 4.1.

The dedicated GENHEN package [62] is suitable for the full range of neutrino studies in ANTARES from neutrino oscillations to high energy astrophysics with the majority of detected neutrinos in a range of energies from tens of GeV (limited by the energy threshold of muon detection of around 10 GeV) to a multi-PeV (where we must take into account the absorption of neutrinos in the Earth, which strongly attenuates the upward neutrino flux).

The typical uncertainties due to the statistics of the simulation should be at the level of $\sim 5\%$. To meet these aims, the following general requirements must be satisfied:

- The relevant neutrino interactions from energies of a few GeV must be correctly simulated to conservatively include the interesting energy range. At high energies this is dominated by Deep Inelastic Scattering (DIS) [92].
- Neutrinos interacting both inside the can (volume events) and outside the can (surface events) should be simulated in the same package in the correct proportions.
- For events inside the can, the production of the hadronic shower at the interaction vertex must be simulated as charged secondary particles can contribute to the total amount of Cherenkov light observed.
- For events outside the can, high energy muons must be tracked until they are stopped or reach the surface of the can.
- The effect of the different media (rock and water) around the detector must be taken into account in both the neutrino interactions and muon propagation.
- For high energy neutrinos, the probability of absorption in the Earth must be calculated given the neutrino interaction cross-section and an Earth density profile.

4.1.2 Event generation method

Neutrino interactions are generated in order to satisfy the requirements described in the previous section. A power law, $E^{-\gamma}$, is chosen for the generation spectrum of the neutrino interactions (which we will refer to as the “interacting neutrino spectrum” in the following description). This can then be weighted to different neutrino fluxes to give the event rates for specific models.

The general simulation method is to define a volume around the detector which will contain all potentially observable neutrino interactions for the given energy range

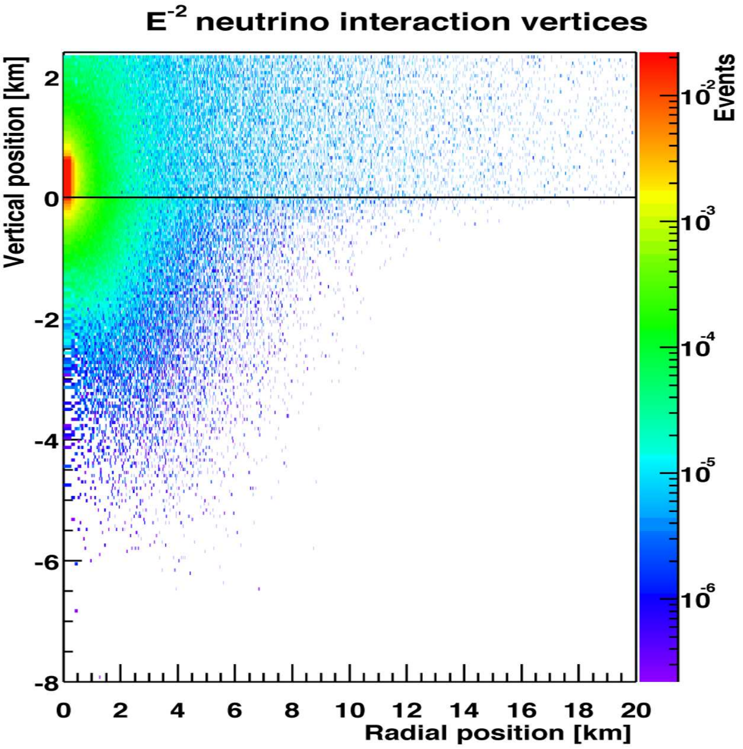

Figure 4.2: Distribution of neutrino vertices around the detector which produce a muon with $E_\mu > 20$ GeV at the "can" surface [91].

and simulate neutrino interactions within that volume. For those neutrino interactions outside the can, any muon produced is then propagated and stored if it reaches the surface of the can. To get meaningful statistics after the muon propagation stage, say a few thousand muons at or within the can, it is typically necessary to simulate $\sim 10^{10}$ neutrino interactions. Clearly, the simulation time required to completely process this number of events would be prohibitive.

The largest possible muon energy in the simulation corresponds to the upper limit on the neutrino energies specified by the user, E_{max}. Hence, the maximum muon range at this energy is R_{max} (water). The interaction vertex distribution in the xz plane for an E^{-2} input spectrum between 100 GeV and 1 PeV is shown in Fig. 4.2. Zero on the vertical axis denotes the sea bed.

No neutrino interacting further away from the detector than these distances can possibly produce a muon which will reach the detector. Hence we can use these distances to define our total simulation volume. Starting with this information, the full simulation then proceeds as follows:

- A cylindrical volume around the instrumented volume of the detector of radius R_{max} (water) is defined.
- The total interacting neutrino spectrum is divided between E_{min} and E_{max} into equal bins in $log_{10}(E_{\nu})$ and the number of events, N, to generate in each bin is calculated.
- For each energy bin, a maximum range in rock and water using the maximum energy in that bin can be calculated.
- Now, for each energy bin the numerical integration of the cross-section in LEPTO is performed and the generation for just this energy range is initialised.
- Looping over the number of events to generate in this scaled volume, N^{i}_{scaled}:
    1. The energy of the interacting neutrino is sampled from the $E^{-\gamma}$ spectrum within the energy range of this bin.
    2. The neutrino position is chosen from within the scaled volume.
    3. Whether or not the vertex is inside the can is determined. If it is outside, the shortest distance from the neutrino vertex position to the can is calculated. If this distance is greater than the maximum muon range at that neutrino energy, no muon produced by this neutrino will ever reach the can and the event is rejected with no further processing.
    4. The neutrino direction is sampled from an isotropic distribution. For events outside the can, it is calculated whether the distance of closest approach of the neutrino direction to the can is greater than some user specified distance.
    5. For each event, the neutrino interaction is simulated using the appropriate code to get the final state particles at the neutrino interaction vertex.
    6. For events inside the can, all these particles are recorded (position, direction, energy, etc) for further processing. For events outside the can, only the muons are kept.

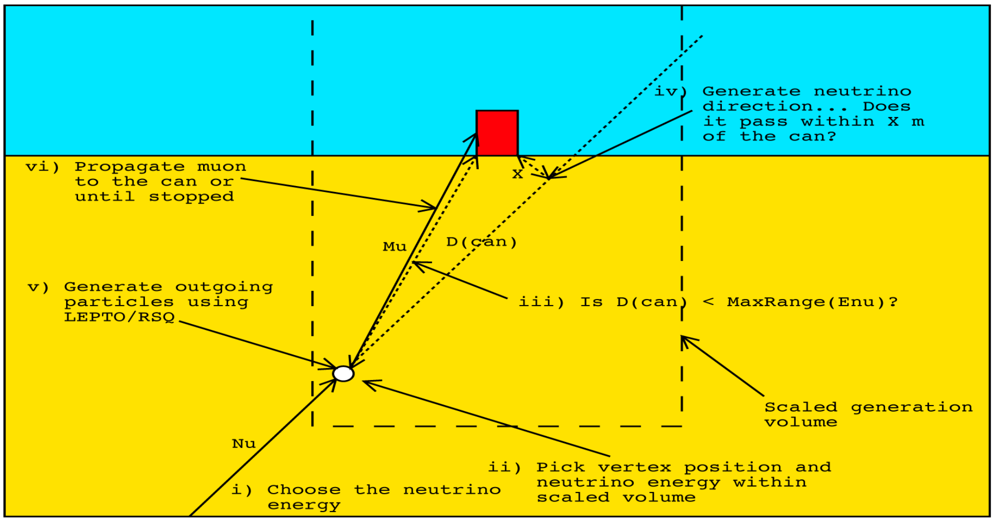

Figure 4.3: Schematic overview of the event generator algorithm [91].

7. For those events which are kept, the "event weights" are calculated and all the event informations written on disk.

- On completion of all the stages above, we get a record of every one of the $\sim 10^{10}$ neutrino interactions which produced at least one particle at or inside the can.

A schematic overview of this method for a neutrino interaction outside the can is shown in Fig. 4.3.

4.1.3 Neutrino fluxes and event weights

The above method generates events for a user input power-law energy spectrum for the neutrino interaction rate. We explain here how to directly re-weight individual events to a particular differential neutrino flux.

To be able to derive the appropriate event weight, we need to define the following parameters (from the original ANTARES definition [93]):

- V_{gen} (m^3): Total generation volume.

- I_θ (sr) $= 2\pi(\cos\theta_{max} - \cos\theta_{min})$: Angular phase space factor depending on the specified range of $\cos\theta_\nu$. It is the integral of the solid angle.

- I_E: Energy phase space factor depending on the input spectral index, γ, for the neutrino interaction rate. If $\gamma = 1$, $I_E = \ln(E_{max}/E_{min})$ otherwise $I_E = (E_{max}^{1-\gamma} - E_{min}^{1-\gamma})/(1-\gamma)$. It is the integral of the generation spectrum between the minimum and maximum energies.
- $\sigma(E_\nu)$ (m^2):Total neutrino cross-section of the charged current neutrino interaction.
- ρN_A (m^3): Total number of target nucleons per unit volume (ρ is the target density and N_A the Avogadro's number).
- $P_{Earth}(E;\theta)$: Probability of neutrinos to penetrate the Earth.
- N_{total}: Total number of generated events.
- t_{gen} (s): The (arbitrary) time represented by the simulation.

Now, the generated events correspond to a rate, Γ_ν^I, of interacting neutrinos (with units of $\mathrm{GeV}^{-1}\ \mathrm{m}^{-3}\ \mathrm{s}^{-1}\ \mathrm{sr}^{-1}$) with the following distribution:

$$\frac{\mathrm{d}\Gamma_\nu^I}{\mathrm{d}E_\nu \mathrm{d}V \mathrm{d}t \mathrm{d}\Omega} = \frac{E^{-\gamma}}{I_E} \cdot \frac{1}{I_\theta} \cdot \frac{N_{total}}{V_{gen}} \cdot \frac{1}{t_{gen}}. \tag{4.1}$$

Integrating this over the range of angles, energy, time and volume simulated correctly gives the total number of generated events, N_{total}. The rate of interacting neutrinos depends on the incoming neutrino flux ϕ_ν (per unit area $\mathrm{d}S$), the target density and the neutrino cross-section. Hence, to convert from the above interaction rate to give the neutrino the events we generated correspond to, we divide the interaction rate by the target nucleon density and neutrino interaction cross-section:

$$\frac{\mathrm{d}\phi_\nu}{\mathrm{d}E_\nu \mathrm{d}S \mathrm{d}t \mathrm{d}\Omega} = \frac{\mathrm{d}\Gamma_\nu^I}{\mathrm{d}E_\nu \mathrm{d}V \mathrm{d}t \mathrm{d}\Omega} \cdot \frac{1}{\sigma(E_\nu)\rho N_A} = \frac{E^{-\gamma}}{I_E} \cdot \frac{1}{I_\theta} \cdot \frac{N_{total}}{V_{gen}} \cdot \frac{1}{t_{gen}} \cdot \frac{1}{\sigma(E_\nu)\rho N_A}. \tag{4.2}$$

This is the flux of neutrinos arriving at the detector which is in turn just the flux of neutrinos arriving at the surface of the Earth times the probability of transmission through the Earth, $P_{Earth}(E;\theta)$, for a particular E_ν and θ_ν. Hence, the flux of simulated neutrinos arriving at the Earth is:

$$\frac{\mathrm{d}\phi_\nu}{\mathrm{d}E_\nu \mathrm{d}S \mathrm{d}t \mathrm{d}\Omega} = \frac{N_{total}}{V_{gen}\ I_\theta\ I_E\ E^\gamma\ \sigma(E_\nu)\ \rho N_A\ t_{gen}\ P_{Earth}(E;\theta)}. \tag{4.3}$$

For a flux corresponding to a particular model:

$$\frac{\mathrm{d}\phi_\nu^{model}}{\mathrm{d}E_\nu \mathrm{d}S \mathrm{d}t \mathrm{d}\Omega} \equiv \phi(E_\nu \theta_\nu) \tag{4.4}$$

we must re-weight the events in each interval $\mathrm{d}E_\nu \mathrm{d}\theta_\nu$ by the ratio of the two fluxes at that point. To obtain a rate of events per second (setting t_{gen} equal to 1) corresponding to a specific neutrino flux model described by $\phi(E_\nu \theta_\nu)$, we take each of our sample of events in each interval $\mathrm{d}E_\nu \mathrm{d}\theta_\nu$ from the simulation and weight them by the ratio of the model neutrino flux to the generated flux. This then gives us the weight, W_{event}, with a flux independent part, $W_{generation}$, associated with each individual event for a particular model:

$$W_{generation} = \frac{V_{gen}\ I_\theta\ I_E\ E^\gamma\ \sigma(E_\nu)\ \rho N_A\ P_{Earth}(E;\theta)}{N_{total}} \tag{4.5}$$

$$W_{event} = W_{generation} \cdot \phi(E_\nu \theta_\nu). \tag{4.6}$$

For convenience, $W_{generation}$ is calculated for each event during the generation phase. This allows for a range of different fluxes to be applied without recalculating all the individual elements of the weight. To obtain distributions or event rates corresponding to a particular model we then just multiply each event by its weight when filling histograms.

Neutrino absorption in the Earth

The neutrino interaction cross-section and the density of matter through the Earth determine the probability of a neutrino being absorbed along its path. The Earth is therefore opaque to very high energy neutrinos.

The amount of matter $\rho(\theta)$ that the neutrino encounters while traversing the Earth was taken from [53]; it is shown in Fig. 4.4 (left) as a function of the zenith angle θ. The column density seen by neutrinos with $\theta > 145°$ is enhanced due to the increased density of the Earth core. The probability that the neutrino survives its journey through the Earth is given by:

$$P_{Earth}(E_\nu;\theta_\nu) = \mathrm{e}^{-N_A \sigma(E_\nu)\rho(\theta)} \tag{4.7}$$

and is shown in Fig. 4.4 (right) as a function of the energy and zenith angle of the neutrino. This probability is taken into account in the calculation of the expected event

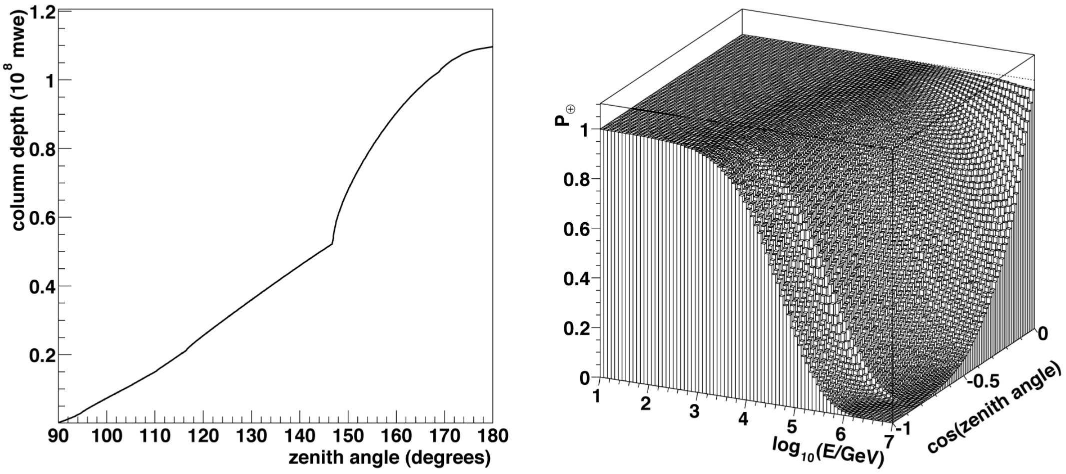

Figure 4.4: Left: The density of the Earth, integrated over the path of the neutrino as a function of the direction of the neutrino expressed in meters of water equivalent. The kink in the figure is caused by the density discontinuity associated with the boundary of the Earths core. Right: The probability of a neutrino to traverse the Earth without undergoing an interaction as a function of its direction (zenith angle) and its energy [66].

rate. For neutrino directions close to vertically upwards, $\cos\theta = -1$, absorption in the Earth starts to be significant for neutrino energies above 10 TeV. Above 1 PeV, only neutrinos close to the horizontal remain unattenuated.

Atmospheric neutrino flux

The principal neutrino signal in ANTARES will be that from "conventional" atmospheric neutrinos. There are a number of different calculations of the atmospheric neutrino flux depending on measurements of the primary cosmic ray flux and different interaction models in the atmosphere. The main models of interest are Honda (HKKM) [94] and Bartol [47].

These calculations depend on the measured cosmic ray spectrum and extrapolation of hadronic interaction models to high energies. The overall uncertainty on the high energy atmospheric neutrino flux is estimated [95] to be of order 20% based on the uncertainties in the two inputs above. It should be noted that the close agreement between the Honda and Bartol calculations is a result of a cancellation between the differences in the primary cosmic ray spectrum used and the hadronic interaction models and that the actual uncertainty is much larger than the difference between these two models suggests. In our analysis as a default we use the Bartol flux, with the extension at energies up to $\sim$ 100 TeV taken from tables in [96].

In addition to the conventional neutrino flux produced by decaying pions and kaons in cosmic ray showers, there is the so-called “prompt” neutrino flux from the decay of charmed mesons which dominates the total flux above 10^5 GeV with a range of different predictions depending on the extrapolation of charm production cross-sections from accelerator energies. C.G.S. Costa describes in [97] three general models of charm production: Quark-Gluon String Model (QGSM), Recombination Quark Parton Model (RQPM), Perturbative QCD (pQCD). For this thesis we consider the prompt models reported in §4.6.2.

4.2 Atmospheric muon simulation

The most abundant signal for a neutrino telescope is due to high energy muons resulting from the extensive air showers produced by interactions of CRs in the upper atmosphere. Although the ANTARES telescope is located at large depth under the sea, taking advantage of the shielding effect offered by the water, a large flux of high energy atmospheric muons will reach the active volume of the detector.

The atmospheric muons represent an insidious background for track reconstruction as their Cherenkov light can mimic fake upgoing tracks. This kind of signatures can be confused with the cosmic neutrino signal that we are searching for. In addition, atmospheric muons are a useful tool to test offline analysis software, to check the understanding of the detector and to estimate uncertainties.

Atmospheric muon bundles can be accurately reproduced by a full MC simulation, starting from primary CR interactions with atmospheric nuclei (e.g. CORSIKA [72]), generating the resulting air showers and propagating the muons through sea water. A full MC requires a large amount of computing time and therefore the production of a large statistical sample cannot be easily obtained. In the AMANDA-II search for a diffuse flux of neutrinos [44], the use of a full MC simulation limited the equivalent time of generated atmospheric muons at 63 equivalent days in spite of a background for 807 active days of data.

In order to save computing time, a fast MC generator is essential. The software used here is the MUPAGE package [71]. The program was developed from parametric formulas derived in [98], that describe the flux, the angular distribution and the energy spectrum of underwater muon bundles. The muon flux and energy spectrum are parametrized in terms of the bundle multiplicity m. The program output contains the kinematics of atmospheric muon bundles on the can surface. The event generation in MUPAGE is done without any kind of weights: the software automatically calculates the livetime corresponding to the simulated events. In other words, the user does not have the possibility to change the primary energy spectrum. This limits the possibility to simulate different models, with the advantage of a very-low time consuming tool.

4.3 Particle propagation and generation of light in water

All long-lived particles which are stored as output of the physics generators are tracked through the water in the can volume using GEANT-based [99] packages, denoted in ANTARES as KM3 [100] and GEASIM. The composition and density of the water is adjusted to the values at the experimental site.

GEASIM is responsible for all particles but muons tracking. All relevant physics processes activated (energy loss, multiple scattering, radiative processes and hadronic interactions). At each tracking step the Cherenkov cone which is produced by charged particles is calculated. For all optical modules (OM) which are in the cone the hit probability is determined and converted into a photo-electron number using Poisson statistics. A wavelength window of $300 \div 600$ nm is considered and the wavelength dependent absorption length, quantum efficiency and transmission coefficients of the glass sphere and the gel are used to evaluate the hit probability. The relative orientation of the PMT with respect to the Cherenkov front and its angular acceptance is also taken into account. The uncertainty on the angular acceptance of OMs is the main systematic source of uncertainty for the simulated flux of atmospheric νs and μs.

The arrival time is calculated based on the group velocity of the photon front and includes smearing factors from the TTS (transit time spread) of the PMT as well as from the wavelength dispersion, where the latter depends on the distance between track segment and OM. This makes the Cherenkov cone “fuzzy”; in Fig. 4.5 it is shown the angular distribution of the Cherenkov light emitted by an electromagnetic shower. The Cherenkov peak is well visible but the tails extend over the whole angular range. This allows to parametrize the Cherenkov light production of electromagnetic showers which

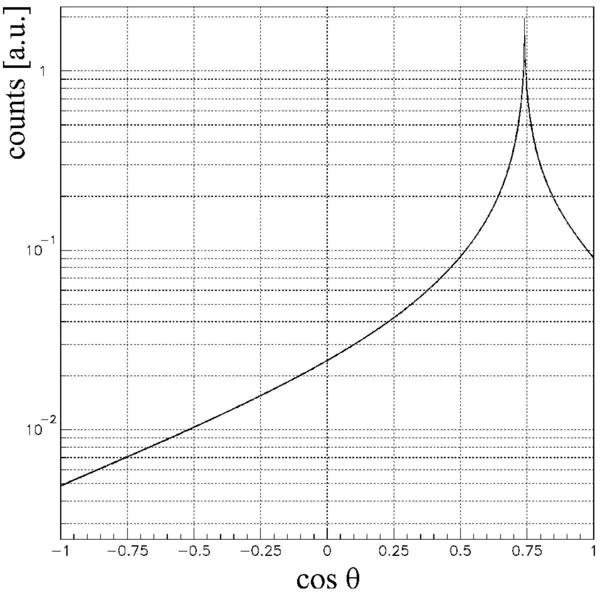

Figure 4.5: Angular distribution of Cherenkov light for electromagnetic showers with respect to the shower axis [77].

in turn economises a significant amount of CPU time. No parametrisation is used for hadronic showers because they exhibit much larger fluctuations and lead occasionally also to secondary muons. The simulation of hadronic interactions is done with the package GHEISHA which is integrated in GEANT [99].

Muons are treated differently to include also the effect of light diffusion. Before simulating physics events one has to create a set of “scattering tables”. Muon tracks with a length of 1 meter are sent to a dedicated GEANT-based program within a large water volume. Energy loss, multiple scattering and radiative process below a given energy threshold (typically $0.1 \div 1$ GeV) are enabled. Individual Cherenkov photons are created and tracked in the water. A diffusion and absorption model has been implemented and allows to track each photon through various scattering processes until it gets absorbed or leaves the volume. Each time a photon penetrates one of several concentric spheres around the muon track origin, its position, direction and time is stored (Fig. 4.6). This photon field is then convoluted with possible orientations of OMs in these spheres which leads to hit probability tables in a 5 dimensional parameter space: R – distance from muon origin, θ – latitude on the sphere, $(\vartheta; \varphi)$ – orientation of OM with respect to muon direction, t – photon arrival time. These scattering tables are

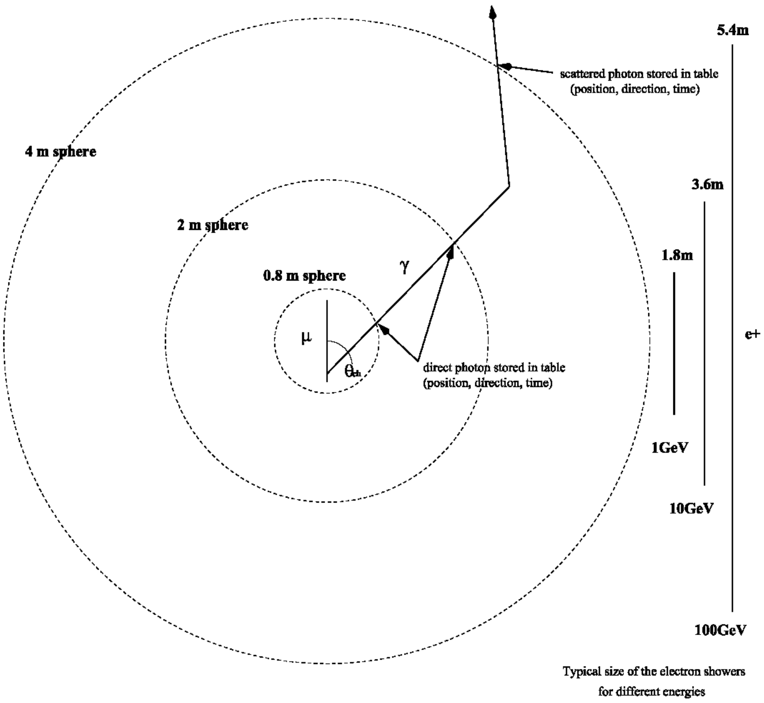

Figure 4.6: Scheme for creation of scattering tables [77].

also created for electromagnetic showers and stored for the next processing step. Now muons from physics generator events are tracked in the usual can volume by MUSIC [101]. After each tracking step the hit probabilities for all OMs are evaluated using the scattering tables. No Cherenkov photon tracking is necessary at this step. One set of scattering tables can be reused as long as the underlying scattering and absorption model does not have to be changed.

4.4 Detector response and trigger simulation

The detector response is simulated using the TriggerEfficiency program [102]. This software consists of the addition of the optical background to the hits generated by physical events, the simulation of the electronics, and the triggering of events.

The optical background can be generated and added to the MC events, according to a Poisson distribution, using a fixed background rate specified by the user (e.g. a mean optical rate of 60 kHz), or using a real data run. With this second option the TriggerEfficiency program adds to the PMTs a background which corresponds to a counting rate taken from real detector situation. In other words, it takes into account not only the background due to the radioactive salt decay but also any kind of biological activities that can occur in sea water (e.g. bioluminescence, bio-fouling) and temporary problems related with the electronics (e.g. charge saturations, temporary power off of single PMTs, "sparks").

The front-end ARS chip integrates the analogue signal from the PMT over a typical time window of 25 ns. This is simulated by summing the number of detected photons in that window. After the integration, the ARS cannot take data for about 250 ns. A second ARS, connected to the same PMT, digitises signals arriving afterwards. The time resolution for single photo-electron signals is 1.3 ns and decreases for higher amplitudes. To simulate this effect, the hit times are smeared using a Gaussian function with a width $\sigma = 1.3\ \text{ns}/\sqrt{N_\gamma}$, where N_γ is the number of simultaneously detected photons. The so-called "level zero" (L0) trigger selects hits that have a charge greater than a low threshold – typically 0.3 photo-electrons (p.e.). The amplitude measurement is then simulated by smearing the integrated number of photons with an empirical function. This function results in a (roughly Gaussian) smearing of about 30% [102]. The dynamic range of the charge integration has a saturation level which corresponds to about 20 photo-electrons.

MC events are triggered with the same trigger algorithm used for real data. The first level trigger (L1) is built up of coincidence hits in the same storey within a 20 ns time window, and single hits with a large charge amplitude, grater than a "high threshold" tuneable from 2.5 p.e. to 10 p.e. A trigger logic algorithm, a level 2 trigger (L2), is then applied to data and operates on L1 hits. The main physics triggers are the 3D-directional scan logic trigger "3N" and cluster logic trigger "2T3".

The 3N trigger processes all data and declares an event as soon as a minimum number of L1 hits are found within a 2.2 μs time interval. In addition, each pair of L1 hits should verify the causality relation:

$$\Delta t_{ij} \leq \frac{d_{ij}}{c/n} + 20\ \text{ns} \tag{4.8}$$

where Δt_{ij} and d_{ij} are the time difference and the spatial distance between $(\text{hit})_i$ and $(\text{hit})_j$ respectively, c is the speed of light and n the index of refraction of the sea water. Eventually an extra scan of directions (1D trigger) is applied. The 1D trigger implements a standard 1-dimensional trigger looking for time correlated hits from a muon in a given direction.

The 2T3 trigger is based on the definition of a "T3 cluster" of hits [103]. A T3 cluster is defined when two L1 hits among three adjacent storeys are in coincidence. The coincidence time window is set to 100 ns in case that the two storeys are adjacent, and to 200 ns in case of next to adjacent storeys. The 2T3 trigger logic requires at least two T3 clusters within a time window of 2.2 μs.

The generated output of TriggerEfficiency is in the same format (*.root) [104] than real raw data. The real data sample analysed in this thesis corresponds to a period in which the high threshold was set equal to 3 p.e., and both the 3N and 2T3 triggers were used.

4.5 Track reconstruction

The algorithm used to estimate the direction and position of the muon from the arrival times and amplitudes of the hits is discussed here. The reconstruction algorithm – we refer to it as the "*Aart* strategy" – consists of four consecutive fitting procedures [66].

The muon trajectory can be characterised by the direction $\overrightarrow{d} \equiv (d_x, d_y, d_z)$ and the position $\overrightarrow{p} \equiv (p_x, p_y, p_z)$ of the muon at some fixed time t_0 (Fig. 4.7). At energies above the detection threshold ($\sim$ 10 GeV) the muon is relativistic. Hence, the speed of the muon is taken to be equal to the speed of light in vacuum. The direction can be parameterised in terms of the azimuth and zenith angles θ and ϕ: $\overrightarrow{d} = (\sin\theta\cos\phi, \sin\theta\sin\phi, \cos\theta)$. There are thus five independent parameters that are estimated by the reconstruction algorithm. For a given track (i.e. a given $\overrightarrow{d}$ and $\overrightarrow{p}$) and an OM at position $\overrightarrow{q}$, whose field of view is oriented in the direction $\overrightarrow{w}$, the relevant properties of a Cherenkov photon emitted from the muon track are: the theoretical arrival time of the photon, the expected photon path length and the expected cosine of the angle of incidence of the photon on the OM, i.e. the angle between the direction of the photon and the pointing direction of the PMT. These three quantities are calculated under the assumption that the light is emitted under the Cherenkov angle w.r.t. the muon and travels in a straight line to the OM. The true arrival time, path length and angle of incidence may differ from these values, since photons are also emitted from secondary electrons and their path is influenced by scattering.

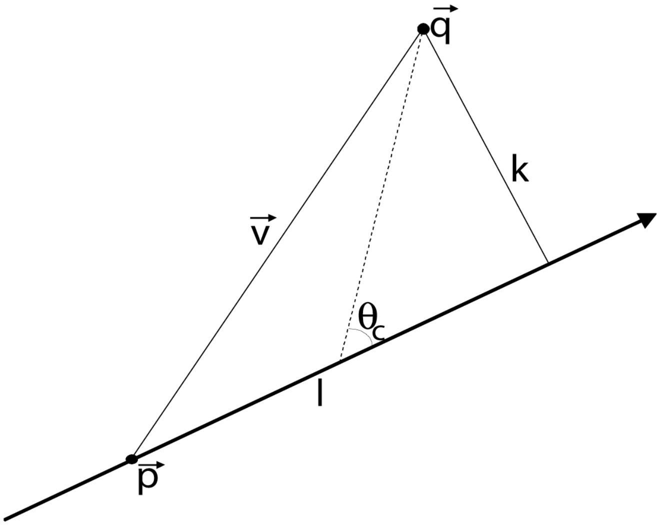

Figure 4.7: Description of the geometry of the detection of the Cherenkov light. The muon goes through point p in the direction d. The Cherenkov light is emitted at an angle θ_C with respect to the muon track and is detected by an OM located in point q. The dashed line indicates the path of the light [66].

The full reconstruction algorithm may be summarised as follows:

1. **Pre-selection of hits:** In order to make the algorithm insensitive to the amount of optical background, a rough, first selection is made. All hits are selected for which $|\Delta t| \leq \frac{d}{v} + 100$ ns, where Δt is the time difference between a hit and the hit with the largest amplitude in the sample and d is the distance between the OMs of the two hits.

2. **Linear prefit:** Although not very accurate, it has the advantage that it requires no starting point. Only hits in local coincidences and hits with amplitudes larger than 3.0 p.e. are used. A local coincidence is defined as a combination of 2 or more hits on one floor within 25 ns.

3. **M-estimator fit:** The hits used for this fit are selected on the basis of the result of the prefit. In order to be selected, a hit must have a time residual w.r.t. the t^{th} calculated from the parameters obtained with the linear prefit between -150 and 150 ns and a distance from the fitted track of less than 100 m.

4. **Maximum likelihood fit with original PDF:** This fit is performed with hits

that are selected based on the result of the M-estimator fit. Hits that are part of a coincidence, or that have an amplitude larger than 2.5 p.e. are also selected.

5. **Repetition of steps 3 and 4 with different starting points:** It was found that the efficiency of the algorithm is improved by repeating steps 3 and 4 with a number of starting points that differ from the prefit. The result with the best likelihood per degree of freedom, as obtained in step 4, is kept.

6. **Maximum likelihood fit with improved PDF:** Finally, the preferred result obtained in step 5 is used as a starting point for the ML fit with the improved PDF. The hit selection is also based on this result: hits are selected with residuals between -250 and 250 ns and with amplitudes larger than 2.5 p.e. or in local coincidences.

The rejection of mis-reconstructed tracks can be made using two reconstruction quality related variables: the log-likelihood per degree of freedom ($\log(L)/N_{DOF}$) and the number of compatible solutions (N_{comp}) found by the reconstruction program. It has been evaluated in [66] that cutting on a dedicated variable Λ, which combines $\log(L)/N_{DOF}$ and N_{comp}, is the best selection criteria of well reconstructed tracks:

$$\Lambda \equiv \frac{\log(L)}{N_{DOF}} + 0.1(N_{comp} - 1). \tag{4.9}$$

4.6 MonteCarlo samples

The MonteCarlo neutrino sample used for this analysis is generated and processed with the tools described in §4.1-4.5. Neutrino events have been generated in the energy range $10 \leq E_\nu \leq 10^7$ GeV, with an energy spectrum $\gamma = -1.4$. Their zenith angle is in the interval $0° \leq \theta \leq 90°$ (upgoing events). The same MC sample can be differently weighted to reproduce the different flux of the Bartol atmospheric neutrinos and the astrophysical signal, with weights defined in §4.1.3. For the signal it is only considered a spectral index of E^{-2}. Harder/softer spectra predicted by different astrophysical neutrino models are not taken into account here. Concerning the background from mis-reconstructed downgoing atmospheric muons, we used the MUPAGE atmospheric muon generator.

4.6.1 Muon neutrinos from astrophysical sources

The signal we are searching for is represented by extraterrestrial neutrinos from unresolved sources. Due to the strong relationship between CRs, γ-rays and cosmic neutrinos described in Chapter 1, the observation of diffuse flux of gamma-rays and of UHE CRs can be used to set theoretical upper bounds on the total flux of neutrinos from extragalactic sources (diffuse neutrino flux).

The upper bound proposed by Waxman-Bahcall (WB) has a E^{-2} dependence, as described in §1.5.1. In this thesis, we used as a test spectrum the value:

$$E^2 \ \Phi_{test} = 1.0 \times 10^{-7} \ \mathrm{GeV \ cm^{-2} \ s^{-1} \ sr^{-1}}. \tag{4.10}$$

The normalisation of the flux is irrelevant when defining cuts, optimising procedures, and calculating the sensitivity of the ANTARES detector, as explained in the next chapter. For comparisons, in the published AMANDA-II paper [44] the reference flux is a factor of 10 higher than the value in eq. 4.10.

4.6.2 Atmospheric muon neutrinos

The only way to detect the diffuse flux of high energy neutrinos is looking for an excess of high energy events in the measured energy spectrum induced by atmospheric neutrinos. The upward going muons induced by atmospheric neutrinos represent an irreducible background. Atmospheric muons are produced by the interaction of high-energy cosmic rays in the atmosphere. The muon (anti)neutrino events were generated with the software chain described in §4.1.2; they were weighted to reproduce the “conventional” atmospheric neutrino flux, due to the pion and kaon decay induced fluxes (§4.1.3).

Above 10 TeV, the semi-leptonic decay of very-short lived charmed particles becomes to be a significant source of atmospheric neutrinos, despite their low production rate. The main contribution comes from the decay mode:

$$D \rightarrow K + \mu + \nu. \tag{4.11}$$

Muon and neutrino thus generate are called “prompt leptons”, and they exhibit a flatter energy spectrum with respect to the conventional atmospheric neutrinos. The lack of precise information on high-energy charm production in hadron-nucleus collisions leads to a great uncertainty in the estimate of the leptonic flux above 100 TeV. The predictions of resulting fluxes span up to several orders of magnitude [97]. For this analysis we parametrized two models taken from [97].

4.6.2.1 Recombination Quark Parton Model (RQPM)

The Recombination Quark Parton Model is a phenomenological non-perturbative approach, that takes into account the contribution of the intrinsic charm to the production process, in which a $c\bar{c}$ pair is coupled to more than one constituent of the projectile hadron, as described by Bugaev *et al.* [105].

In Fig. 4.8 it is shown the component of atmospheric neutrino background due to the conventional atmospheric neutrino computation of the Bartol group, plus the prompt neutrinos generated with RQPM. For energies $E_\nu < 10^5$ GeV the contribution due to prompt neutrinos is negligible.

4.6.2.2 Quark Gluon String Model (QGSM)

The Quark Gluon String Model is a semi-empirical model of charm production based on the non-perturbative QCD calculation by Kaidalov and Piskunova [106], normalised to accelerator data, and applied to the prompt muon calculation by Volkova *et al.* [107].

The component of atmospheric neutrino background due to the QGSM is shown in Fig. 4.9, again with the Bartol conventional atmospheric neutrinos.

The energy above which the charm particle decay production dominates over the conventional pion and kaon decay induced fluxes, is an uncertain quantity around $\sim 10^5$ GeV. Comparing the two different prompt models, we can emphasise that the RQPM model is more efficient at higher energies ($> 10^{5.5}$ GeV), while the QGSM model gives a large number of events integrated over all the energy spectrum.

4.6.3 Atmospheric muons

Atmospheric muons were simulated with the MUPAGE package [71]. Atmospheric muons reconstructed as up-going are the main background for neutrino signal in the ANTARES detector. Due to the huge amount of data, the rejection of wrongly reconstructed muon events is a crucial point in this analysis. The signal we are searching for (high-energy astrophysical neutrinos) is order of units of events per year. For this

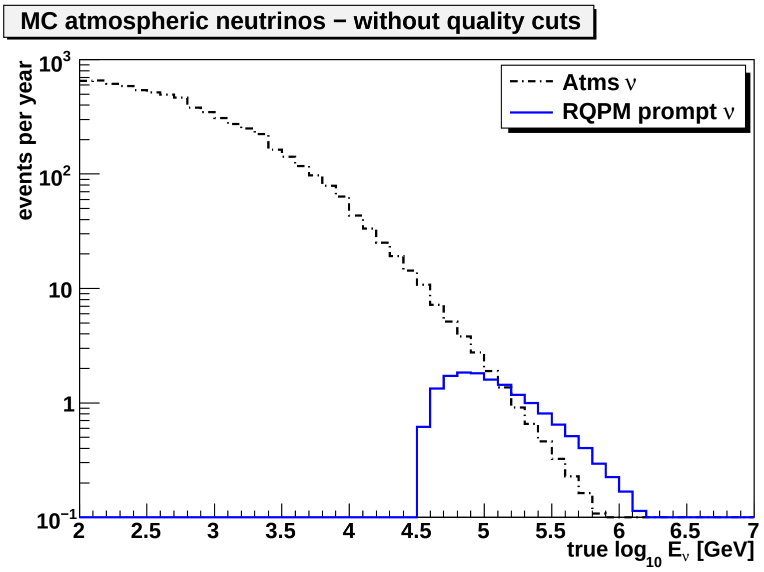

Figure 4.8: Differential rate of events per year as a function of the $log_{10}E_\nu$, where E_ν is the true (i.e. from MC) energy of the neutrino. The prediction of the RQPM prompt neutrinos is compared with the Bartol atmospheric flux. The events have been reconstructed with the Aart strategy without any cuts.

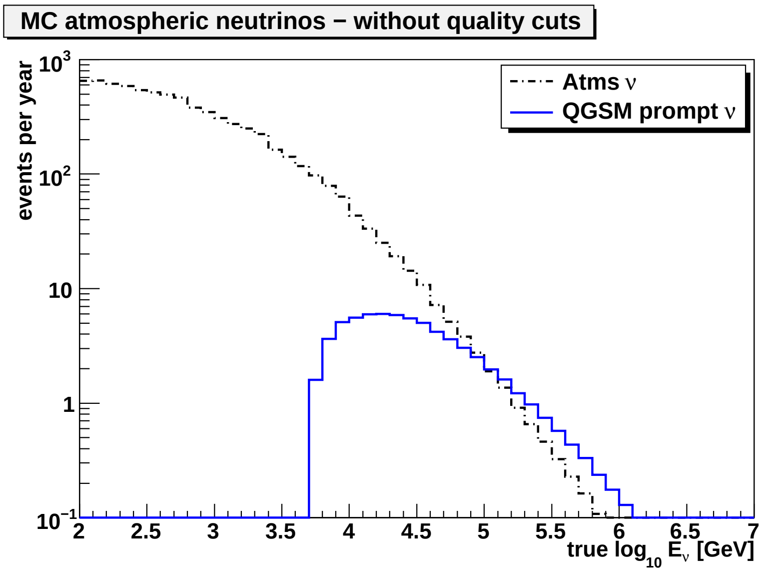

Figure 4.9: As in Fig. 4.8, for the QGSM prompt neutrino model.

Sample	**time**	**$E_{th.}$**	**m_{bundle}**	**Gen. evs**	**Trig. evs**	**Rec. evs**
A	30 days	1 GeV	$1 \div 100$	1.6×10^9	2.1×10^7	2.0×10^7
B	365 days	1 TeV	$1 \div 1000$	1.8×10^9	1.2×10^8	1.2×10^8

Table 4.1: Properties of the MUPAGE MC samples used to simulate the atmospheric muon background. The number of generated, triggered, and reconstructed events is reported. The two samples differs in the equivalent livetime, in the simulated muon bundle multiplicity and in the threshold energy.

reason, we need at least one year of simulated equivalent livetime for the MUPAGE production, to prove via MC our capability to reject the background. To save CPU time, we managed to use two different MC sample and compare results:

- **A – "Standard" MUPAGE production:** one month of equivalent livetime; threshold energy equal to 1 GeV (it represent the sum of the energy of individual muons in the bundle); bundle multiplicity $m = 1 \div 100$. This production ensure the simulation of both low and high energy events, but with a limited statistics.
- **B – "Dedicated" MUPAGE production:** one year of equivalent livetime; threshold energy equal to 1 TeV; multiplicity $m = 1 \div 1000$. This MC sample guarantee a higher statistics, neglecting all the events with energy < 1 TeV. In the next chapter, it will be shown that with "soft" cuts on appropriate observables most of low energy events are rejected, validating the choice of this energy threshold.

In the Table 4.1 the main properties of the MUPAGE simulations are reported. As it is explained in §4.2, the MonteCarlo samples produced by MUPAGE do not have any weight. The user can not change the generation model, and the livetime is given directly by the software. Events are produced as if they should come from real data acquisition. More details about these simulations are in [108].

Chapter 5

Diffuse flux analysis

The search method for very-high energy extraterrestrial muon neutrinos from unresolved sources is presented in this chapter. The signal we are searching for corresponds to an excess of events, produced by astrophysical sources, over the expected atmospheric neutrino background without any particular assumptions on the source direction. As explained in the previous chapter, an overall $\Phi \propto E^{-2}$ spectrum resulting from shock acceleration processes is assumed. This $\Phi \propto E^{-2}$ spectrum is derived from the Fermi acceleration mechanism, as explained in §1.1.2.

The first step of this analysis is the rejection of the background due to atmospheric muons (Chapter 2). The requirement that the event is reconstructed as "upgoing" is necessary to reject the atmospheric muon background (only neutrinos can produce an upgoing muon in the detector), but it is not sufficient. The fraction of atmospheric "downgoing" muons that can be mis-reconstructed as upgoing is in fact not negligible. These mis-reconstructed atmospheric muon events are several orders of magnitudes more abundant than true upgoing neutrino events. The criteria to completely reject these fake events is presented in §5.1.1 and 5.1.2.

The second step is the statistical selection of very-high energy astrophysical events (our signal) from a large amount of atmospheric neutrino events (our background). This kind of background is more complicated to discriminate than the previous one, since in this case both signal and background events are true upgoing events. Only the differences in the energy spectrum shapes allow to separate the expected signal. Astrophysical sources should produce a flatter spectrum ($\propto E^{-2}$) than the atmospheric neutrinos ($\propto E^{-3.7}$). For this reason, an energy-related observable is defined in §5.2 to separate upgoing astrophysical neutrinos from upgoing atmospheric neutrinos. Various neutrino energy estimators have been tested; some results about their properties are shown (§5.2.1). Finally, using the Model Rejection Potential (MRP) technique [109] (§5.2.2), the sensitivity of the ANTARES telescope to diffuse neutrinos is calculated for 1 year of data taking (§5.4).

5.1 Rejection of atmospheric muon background

The mandatory requirement of the analysis is to completely reject the atmospheric muon background, as presented in this section. The Earth stops totally upgoing atmospheric muons produced by cosmic rays in the opposite hemisphere, but a relevant amount of downgoing events can mimic (due to mis-reconstruction) an upgoing track. The flux of downgoing muons is approximately ~ 6 orders of magnitude greater than the neutrino flux, hence also a small fraction of mis-reconstructed events must be considered as a dangerous source of background.

In order to reject the background of atmospheric muons while keeping the HE neutrino-induced events, we defined two selection steps. Firstly, we establish some preliminary cuts to reject most downgoing muon events (§5.1.1). Using an intermediate cut, we then select event classified as upgoing with very high confidence (§5.1.2).

The MonteCarlo samples defined in the previous chapter are: the MUPAGE sample "A" ($E_{th} = 1$ GeV, 1 month of equivalent livetime) and MUPAGE sample "B" ($E_{th} = 1$ TeV, 1 year of equivalent livetime). The sample "A" describes better the physics at low energies, but with poor statistics at high energies. The sample "B" shows a clear deficit of events at low energies (the threshold energy is 1 TeV). When simple quality and energy cuts are applied, the simulation "B" represents a better sample to characterise the response of our detector for high energy events.

5.1.1 Preliminary cuts

The reconstruction of the events is performed with the "Aart strategy" (see §4.5 and [66]), a software tool developed by the ANTARES collaboration. This algorithm has been optimised in order to give a good angular resolution[1] by cutting in the "Λ" vari-

---

[1] The angular resolution is defined as the median value of the difference, in absolute value, between the reconstructed direction and the true MC direction ($|\theta_{rec} - \theta_{true}|$) evaluated through MC simulation.

able. This variable is a combination of likelihood and number of compatible solutions found by the algorithm itself. Cuts stronger in Λ will select better reconstructed events, reducing the mis-reconstructed event rate, but at the same time it will reduce the number of accepted events.

We define here four simple conditions (*Preliminary cuts*) which remove most of the atmospheric muons:

- $\boldsymbol{\theta_{\mathbf{rec}} < 80^\circ}$: The reconstructed zenith angle must be between $0^\circ \div 80^\circ$. Only events reconstructed as upgoing are selected.
- $\boldsymbol{\Lambda > -6}$: Cut on the reconstruction quality parameter. Very bad reconstructed tracks are rejected.
- $\mathbf{N_{hit} > 60}$: N_{hit} is the number of hits selected in the last step of the reconstruction algorithm. The fit performed with the Aart strategy uses hits that have time residuals between -250 and +250 ns (see §4.5). The minimum number request ensures the rejection of low energy events.
- $\mathbf{L_{prefit} > 1}$: L_{prefit} is the number of lines used in the linear prefit (see §4.5). Events reconstructed with only one line suffer from geometrical problems [110].

Fig. 5.1 and Fig. 5.2 show the effect of the Preliminary cuts on the “A” and “B” MUPAGE samples. The rate of events per year per bin is shown as a function of the $\log E_{bundle}$, where E_{bundle} is the total energy of all atmospheric muons in the bundle. Detected atmospheric muon events mainly consist of multiple muons with multiplicity m originated in the same primary CR interaction. The range of muon multiplicity m which were simulated is: $m = 1 \div 100$ in the sample “A”, $m = 1 \div 1000$ in the sample “B”. The total energy is the sum of single muons in a bundle.

The “B” sample does not simulate at all events with energy below 1 TeV; but after the Preliminary cuts the distributions of sample “A” and “B” become quite similar. The sample “A” shows poor statistic at energies > 100 TeV.

Fig. 5.3 and 5.4 show the rate of events per year per bin as a function of the reconstructed value of the zenith angle for the two atmospheric muon samples before and after the Preliminary cuts. For reference, the distribution of the same quantity as a function of the “true” (simulated) atmospheric muon direction is also shown. Without any cuts a large fraction of atmospheric muons are reconstructed us upgoing ($\theta = 0$

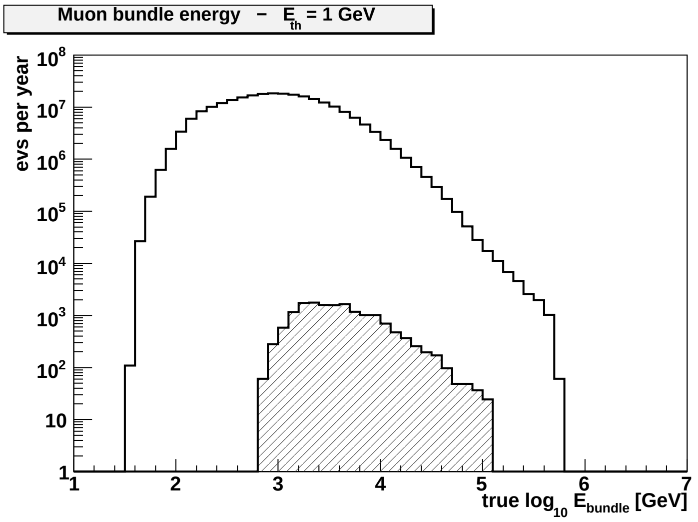

Figure 5.1: Rate of events per year per bin as a function of the $\log E_{bundle}$ for the MUPAGE sample "A" ($E_{bundle} > E_{th} = 1$ GeV, 1 month of equivalent livetime). Events reconstructed without any cuts are represented by the upper line, the filled area represents the events after the Preliminary cuts.

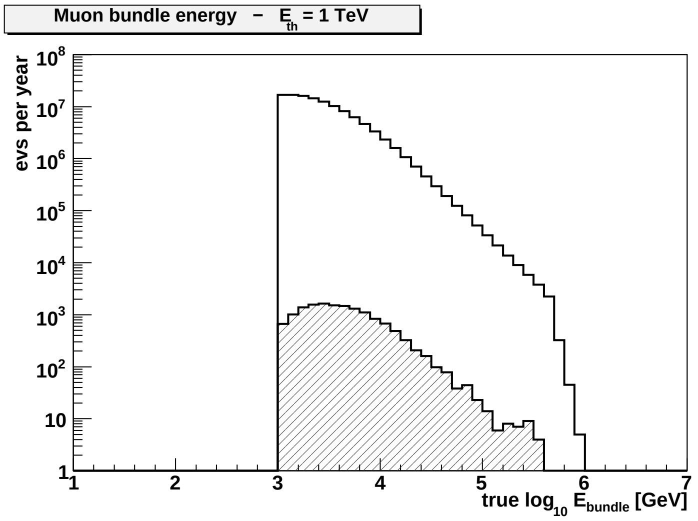

Figure 5.2: Rate of events per year per bin as a function of the $\log E_{bundle}$ for the MUPAGE sample "B" ($E_{bundle} > E_{th} = 1$ TeV, 1 year of equivalent livetime). Events reconstructed without any cuts are represented by the upper line, the filled area represents the events after the Preliminary cuts.

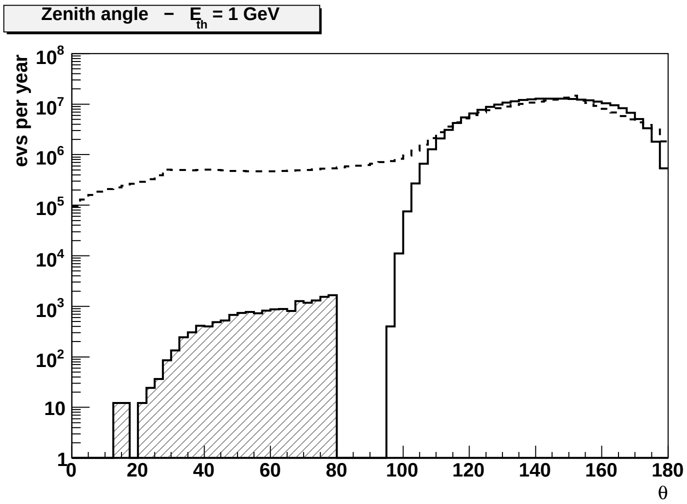

Figure 5.3: Rate of events per year per bin as a function of the reconstructed zenith angle for the MUPAGE sample "A" (E_{th} = 1 GeV, 1 month of equivalent livetime). The dashed line represents events reconstructed without any cuts, the filled area represents the events after the Preliminary cuts. The continuous line represents the rate of events as a function of the simulated (true) zenith angle.

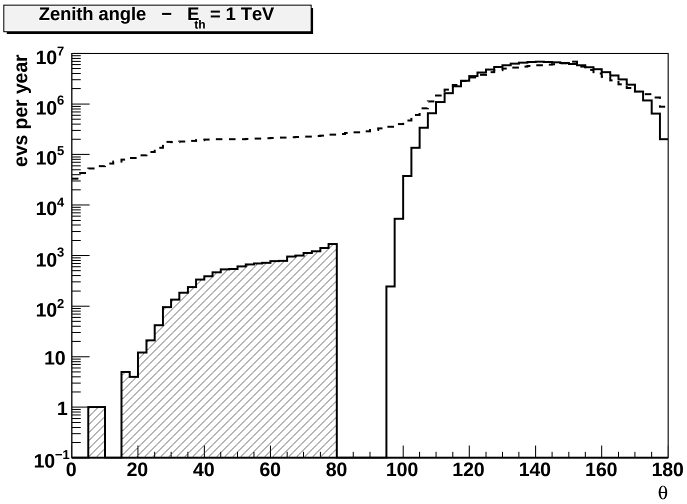

Figure 5.4: Rate of events per year per bin as a function of the reconstructed zenith angle for the MUPAGE sample "B" (E_{th} = 1 TeV, 1 year of equivalent livetime). The dashed line represents events reconstructed without any cuts, the filled area represents the events after the Preliminary cuts. The continuous line represents the rate of events as a function of the simulated (true) zenith angle.

Rate (yr^{-1})	MUPAGE “A”	MUPAGE “B”	atm. Bartol ν	astr. ν
Rec. evs	2.4×10^8	1.2×10^8	1.2×10^4	141
Rec. as upgoing	1.3×10^7	5.2×10^6	1.1×10^4	114
Prelim. cuts	1.6×10^4	1.5×10^4	321	39

Table 5.1: Comparison of the reconstruction event rate (year^{-1}) for the four MC samples before and after the Preliminary cuts. Neutrino events are weighted with the procedure described in 4.1.3. The rate shown for MUPAGE “B” is the effective number of events, while the event rate for MUPAGE “A” is obtained rescaling the number of event to 1 year.

vertically upgoing event, $\theta = 180$ vertically downgoing event). The Preliminary cuts reduce the rate of mis-reconstructed event by about 3 orders of magnitude, as indicated in table 5.1.

The rate of neutrino events that survive the Preliminary cuts is shown in table 5.1. Neutrino MC events are reconstructed with the same algorithm used for atmospheric muons. Atmospheric neutrino events are weighted with the “conventional” Bartol flux described in §4.6.2; “prompt” contribution is not considered yet. Astrophysical neutrinos are weighted with the test flux described in §4.6.1, reported here for clarity:

$$E^2\ \Phi_{test} = 1.0 \times 10^{-7}\ \mathrm{GeV\ cm^{-2}\ s^{-1}\ sr^{-1}}. \tag{5.1}$$

We want to stress some points:

- After Preliminary cuts, there is a large reduction of atmospheric muon events related with the cut on the quality parameter Λ, but the event rate of mis-reconstructed events is still about 2 orders of magnitude greater than true upgoing atmospheric neutrinos.
- The cuts have different impact over the two neutrino spectra. The signal we are searching for has a spectrum flatter with respect to the atmospheric neutrino one; the cut over the number of hits selected by the reconstruction algorithm ensures a pre-selection of high-energy events.

Fig. 5.5 shows the Λ distributions for the four MC samples after Preliminary cuts. The green line represents “A” atmospheric muons and the red one represents “B” atmospheric muons. All events represented in Fig. 5.5 are reconstructed as upgoing. Only

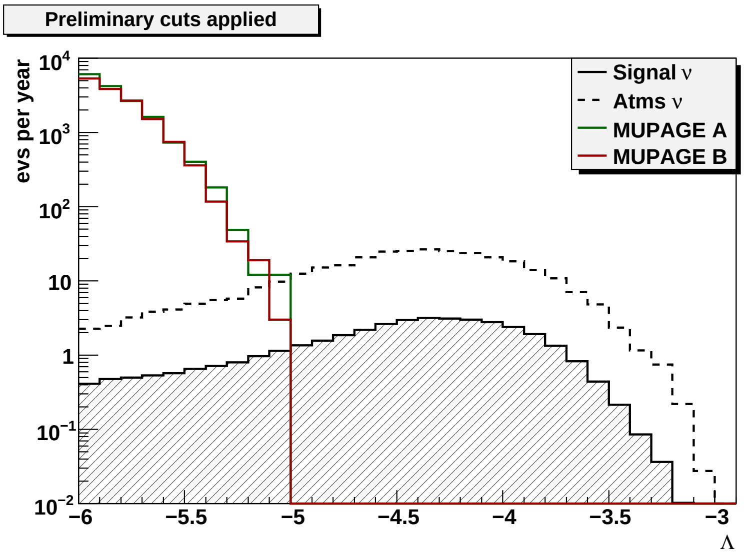

Figure 5.5: Rate of events per year per bin as a function of the reconstruction quality parameter Λ after the Preliminary cuts. The four MC samples are shown. Events are weighted per 1 year of equivalent time. The total number of events in each histogram is the last raw of table 5.1.

the neutrinos are really upgoing. This explains why the distribution of Λ for atmospheric muons is shifted towards smaller values of Λ (i.e. worse reconstruction quality parameter). The red line is under the green in all the interval, because events with total bundle energy below 1 TeV are missing. The Λ distribution for the astrophysical neutrinos is always below that of the atmospheric neutrinos: a cut on the quality reconstruction parameter does not discriminate high energy events with respect to low energy ones for true upgoing events.

The number of hits, N_{hit}, on the contrary, is an energy-related observable: for $N_{hit} \gtrsim 170$ the flux of astrophysical neutrinos is above the flux of atmospheric neutrinos (Fig. 5.6). Unfortunately, the background due to atmospheric muons cannot be removed simply by cutting on this observable. In the next sub-section it is shown that a cut on the Λ variable as a function of N_{hit} will reject all simulated atmospheric muons.

5.1.2 Intermediate cut

At this step of the analysis most of very bad reconstructed events are removed ($\Lambda > -6$) and the accepted events are characterised by a large number of N_{hit}. Still a large number

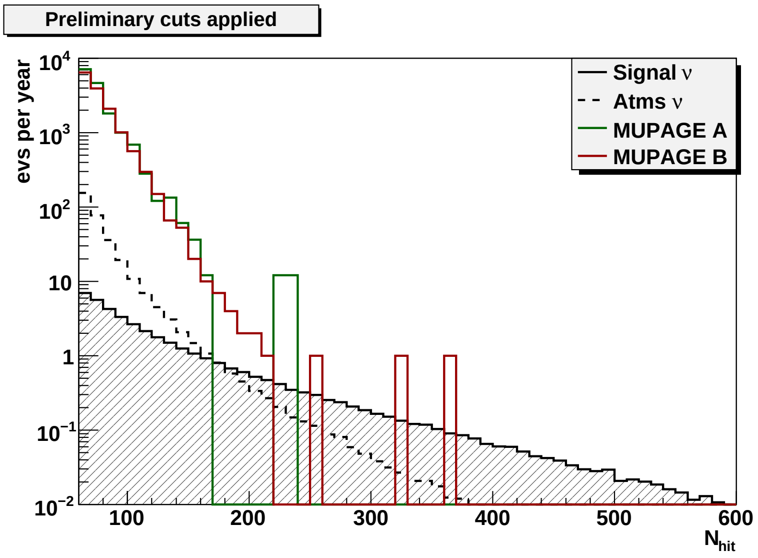

Figure 5.6: Rate of events per year per bin as a function of the number of hits related to tracks selected by the Aart strategy after the Preliminary cuts. The four MC samples are shown. Events are weighted per 1 year of equivalent time. The total number of events in each histogram is reported in the last raw of table 5.1.

of atmospheric muons is reconstructed as upgoing with $\Lambda > -6$, but the quality of the reconstruction decreases with increasing number of hits (Fig. 5.7). The reason is quite simple: it is very difficult that downgoing events which produce a large amount of light in water (and consequently a large amount of hits in the detector) would be mis-reconstructed as upgoing with a high value in Λ. Fig. 5.7 shows the scatter plot of Λ versus the number of hits for the MUPAGE "B" sample (that simulates 1 year of livetime[1]). No events are present above the pink line. The second cut needed to suppress the background from wrongly-reconstructed atmospheric muons is defined using the correlation between the quality reconstruction parameter Λ and the number of hits used in reconstruction N_{hit}:

$$\Lambda > \begin{cases} -4.59 - 5.88 \cdot 10^{-3} N_{hit} & \text{for} \quad N_{hit} \leq 172 \\ -5.6 & \text{for} \quad N_{hit} > 172 \end{cases} \tag{5.2}$$

The correlated cut in eq. 5.2 is referred from now as the *Intermediate cut*. After the Intermediate cut, no atmospheric muon events survives neither in the "A" sample nor

---

[1] An analogous plot (not shown here) is obtained for the MUPAGE "A" sample, but with less statistical significance.

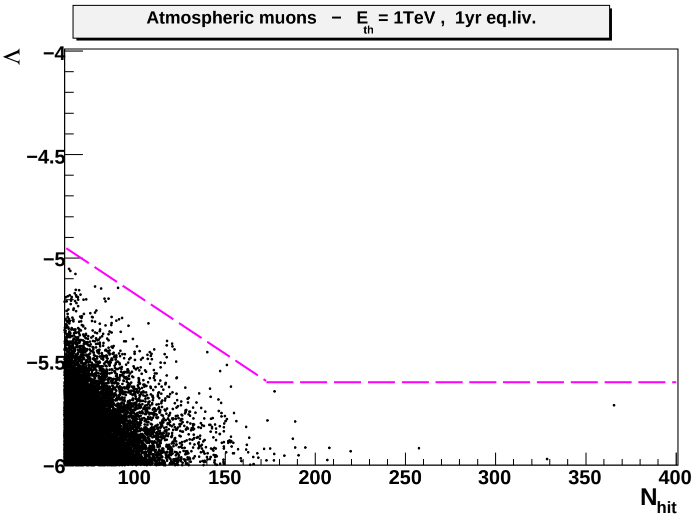

Figure 5.7: MUPAGE "B" sample. Scatter plot of the reconstruction quality parameter Λ versus the number of hits N_{hit} after Preliminary cuts. The quality reconstruction parameter for mis-reconstructed events decreases with increasing number of hits. The pink line represents the cut described by eq. 5.2.

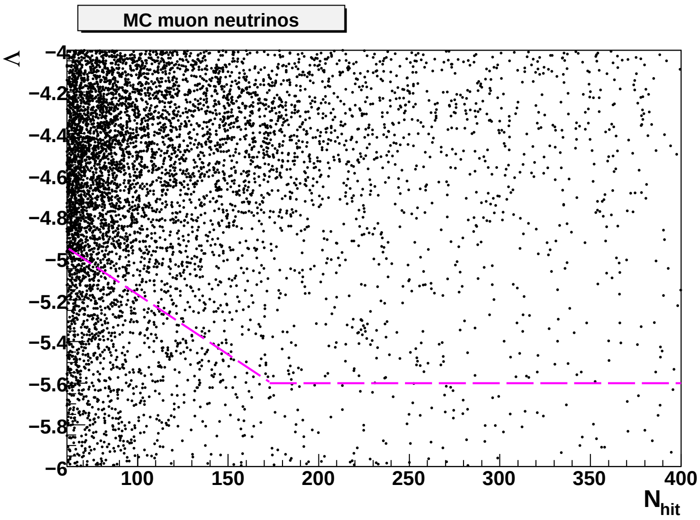

Figure 5.8: MC neutrino signal sample. Scatter plot of the reconstruction quality parameter Λ versus the number of hits N_{hit} after Preliminary cuts. In this plot, the events are not weighted in order to reproduce an event rate, but each point represents one simulated event. The pink line represents the cut described by eq. 5.2.

Rate (yr^{-1})	MUPAGE “A”	MUPAGE “B”	atm. Bartol ν	astr. ν
Rec. as upgoing	1.3×10^7	5.2×10^6	1.1×10^4	114
Prelim. cuts	1.6×10^4	1.5×10^4	321	39
Interm. cuts	0	0	273	34

Table 5.2: Comparison of the reconstruction event rate ($year^{-1}$) for the four MC samples. After the Intermediate cut no atmospheric muon events are selected.

in the “B” sample. Fig. 5.8 shows the effect of this cut on the neutrino signal events.

Table 5.2 shows the event rate (ev/year) of the four MC samples after the selection of upgoing events, the Preliminary cuts and the Intermediate cut. No atmospheric muons survive in the region above the L-shaped line shown in Fig. 5.7 and 5.8. The region below the pink line will be be referred to as the “L” region.

In the next chapter a comparison with a small fraction of ANTARES data will be presented. The ANTARES collaboration has specific rules concerning the treatment of real data. These rules, the so-called *blinding policy*, limit the use of data during the optimisation steps of analyses to avoid that the selection procedure is tuned (inadvertently) on the data sample (optimise the analysis without using the data). A totally “blind” analysis is not applicable when using MC simulations, but we decide to define a “blind region” for ANTARES data avoiding to look into it before the optimisation of all the analysis parameters. The region above the “L” corresponds to our “black box” for the real data: all the comparison plots between data and MC will be produced only in the region below the Intermediate cut (i.e. outside the black box). We continue to have no information about the number and characteristic of events inside the black box.

5.2 Astrophysical event selection

After the Intermediate cut, no fake atmospheric muons survive, and the only background for the cosmic neutrino signal is due to the atmospheric neutrinos. Fig. 5.9 and 5.10 show the effect of the cuts on the reconstructed zenith angle for the two MC neutrino samples.

Upgoing atmospheric neutrinos induced by cosmic rays in the atmosphere represent an irreducible background. They are upgoing, like cosmic neutrinos, and the discrim-

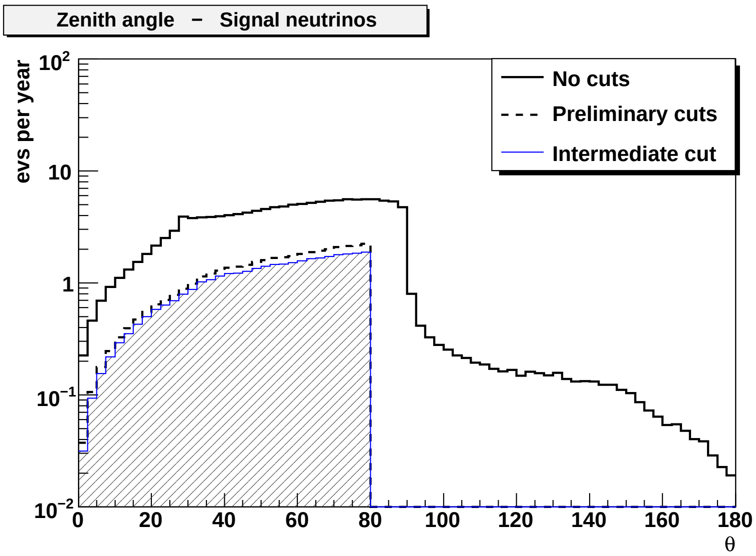

Figure 5.9: Rate of events per year per bin as a function of the reconstructed zenith angle for the sample of cosmic neutrinos. Full line: no cuts. Dashed line: after Preliminary cuts. Dashed histogram: after Intermediate cut.

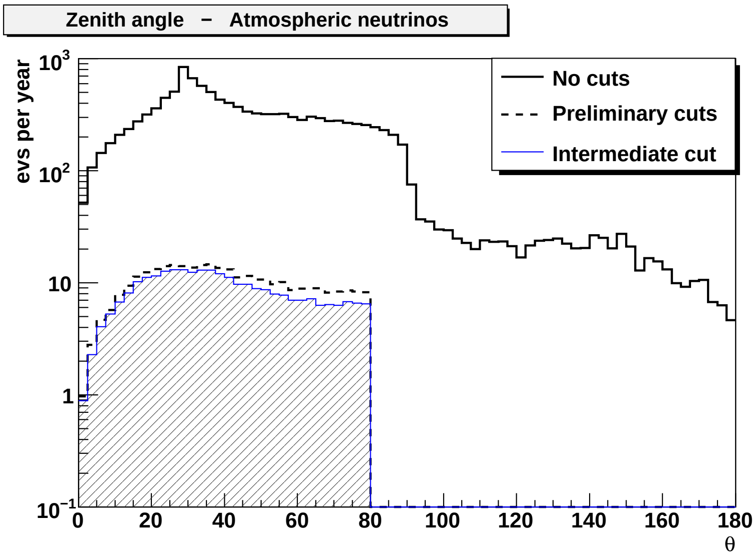

Figure 5.10: Rate of events per year per bin as a function of the reconstructed zenith angle for the sample of atmospheric neutrinos. Full line: no cuts. Dashed line: after Preliminary cuts. Dashed histogram: after Intermediate cut.

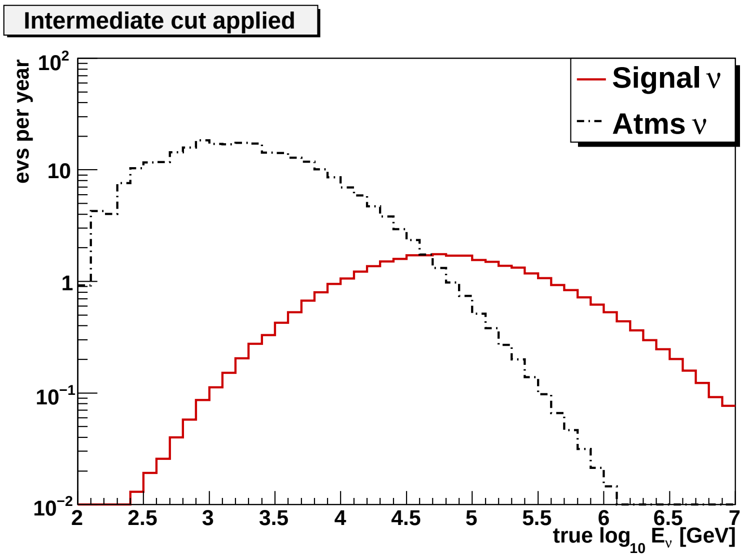

Figure 5.11: Expected event rate per year per bin as a function of the true neutrino energy for cosmic (full red line) and background neutrino (dot-dashed line) events after the Intermediate cut. The contribution of prompt to the atmospheric neutrinos is not yet included (§5.5).

ination between the samples is based on statistical criteria on an energy-correlated variable. The difference between the two samples is that the cosmic signal is characterised by a larger average neutrino energy, see Fig. 5.11. Since atmospheric neutrinos follow a power law steeper than cosmic neutrinos, an excess of events at high energies would be evidence of a cosmic diffuse flux.

5.2.1 Energy estimators

To separate atmospheric neutrinos from astrophysical neutrinos an event energy estimator is needed. Unfortunately, in real conditions the ANTARES detector can not measure directly the muon energy: energy-correlated variables are inevitably distorted by the limited detector resolution. We have investigated two different variables which are correlated with the energy:

- The total number of hits N_{hit} used in the reconstruction.

- The “mean number of repetitions” R.

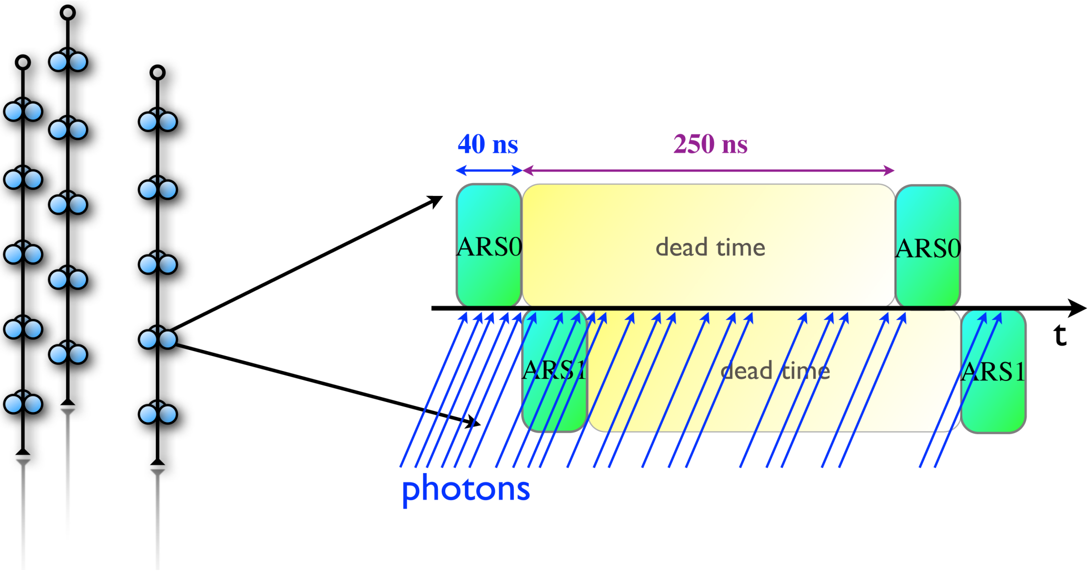

Figure 5.12: Definition of the variable R_i on the i-th OM. In this example, both ASR0 and ARS1 are fired; after the integration dead-time, both chips collected light again. In this example, $R_i = 4$.

The number of hits as energy estimator was used by the AMANDA collaboration [44], and it was also proposed by J.D. Zornoza [67] to estimate the ANTARES sensitivity.

The mean number of repetitions R is defined as follows (Fig. 5.12). The front-end electronics consists of custom built analogue ring sampler (ARS) chips which digitise the charge and the time of the analogue signals from the PMTs. Each OM of the ANTARES telescope contains 2 ARS chips. When a signal from the PMTs passes a preset threshold (typically 0.3 photo-electrons) the first ARS (ARS0) digitises it and sends it to shore. The ARS0 integrates the signal in a time window of 40 ns and then returns the total charge value. If a very-high energy muon is traveling through the detector, it will produce Cherenkov light as well as electromagnetic showers. Secondary electrons and positrons will generate Cherenkov radiation too, and there will be a significant probability that photons can reach the OM with a time delay greater than 40 ns. If this happens, we expect that both ARS in the same OM will be fired; the second ARS (ARS1) will integrate the signal for the following 40 ns, producing a second hit on the same OM. After the integration, every ARS has a dead-time – typically 250 ns.

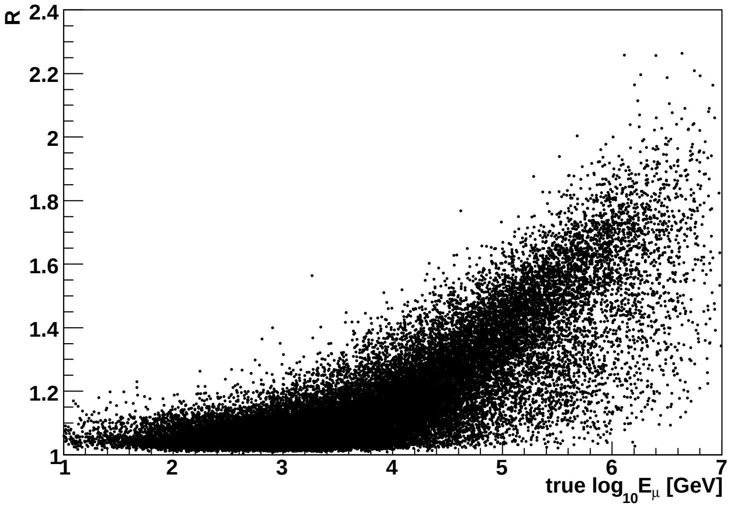

Figure 5.13: The scatter plot shows the correlation between the R variable and the neutrino-induced muon energy.

Let us define the number of repetitions R_i for the i-th OM as the number of hits given by the same OM, in the same event. This value typically will be one or two (the Aart strategy selects hits with time residuals between -250 ns and 250 ns §4.5), but for large signals it could be also 3 or 4. The mean number of repetitions on the event is defined:

$$R = \frac{\sum R_i}{N_{OM}} \tag{5.3}$$

where N_{OM} is the number of OMs interested in the event, and the sum is counting the repetitions on each fired OM. All the hits we consider are used by the tracking algorithm. In Fig. 5.13 a scatter plot displays the correlation between R and the true neutrino-induced muon energy.

5.2.2 Model Rejection Potential technique

The effect of the different energy-dependent estimators mentioned in §5.2.1 on the separation of the signal from the background is evaluated by computing the sensitivity. The sensitivity is estimated using the Model Rejection Potential (MRP) technique [109] which optimises the cuts on the energy estimators itself in order to place the strongest constraints (upper limits) on theoretical signal models. The model relies only on signal and background expectations derived from MC simulations.

Let $\Phi(E)$ be the theoretical source flux in units of GeV^{-1} cm^{-2} s^{-1} sr^{-1}, n_s the number of expected signal events, n_b the expected background, and n_{obs} the number of events observed in a hypothetical experiment. If the number of observed events is compatible with the background, the upper limit for the flux at a 90% confidence level (CL) is:

$$\Phi(E)_{90\%} = \Phi(E)\ \frac{\mu_{90}(n_{obs}, n_b)}{n_s}. \tag{5.4}$$

$\mu_{90}(n_{obs}, n_b)$ is the Feldman-Cousins upper limit [111].

In order to avoid any bias when setting cuts on the energy-related observable, this choice must be done without any information about the data. Only MC predictions must be used to calculate the "average upper limit" that would be observed by an ensemble of hypothetical experiments with no true signal ($n_s = 0$) and expected background n_b. Taking into account all the possible fluctuation for the estimated background, weighted according to their Poisson probability of occurrence, the average upper limit can be estimated as:

$$\overline{\mu}_{90}(n_b) = \sum_{n_{obs}=0}^{\infty} \mu_{90}(n_{obs}, n_b) \frac{(n_b)^{n_{obs}}}{(n_{obs})!} \mathrm{e}^{-n_b}. \tag{5.5}$$

This average upper limit is independent from the observed number of events. The average upper limit is a function of the number of background events only, as shown in Fig. 5.14.

The best upper limit is obtained with the best cut that minimises the so-called Model Rejection Factor (MRF):

$$MRF = \frac{\overline{\mu}_{90}(n_b)}{n_s} \tag{5.6}$$

and hence minimises the average flux upper limit:

$$\overline{\Phi}(E)_{90\%} = \Phi(E) \frac{\overline{\mu}_{90}(n_b)}{n_s}. \tag{5.7}$$

In the next section the sensitivity of the energy estimators is calculated with the method of the MRF minimisation.

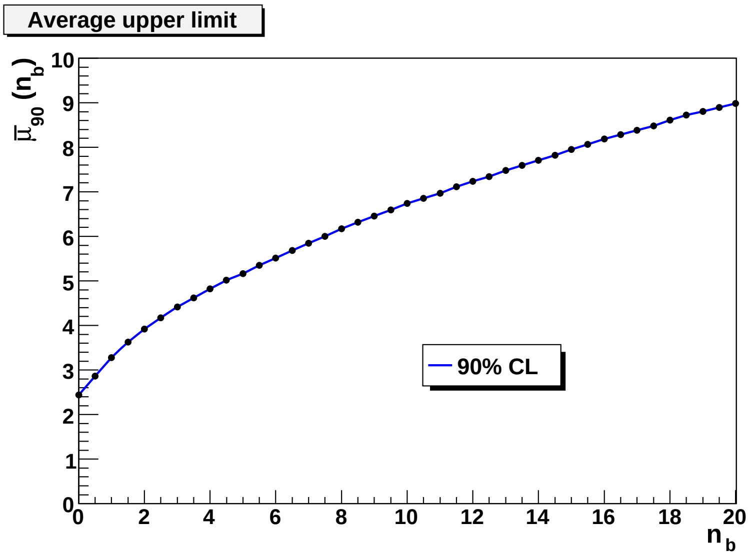

Figure 5.14: Average upper limit $\overline{\mu}_{90}(n_b)$ as a function of the number of background events n_b. The upper limits are calculated using the Feldman-Cousins method at the 90% CL and weighted according to their Poisson probability.

5.3 Comparison between estimators

The ANTARES sensitivity for 1 year of livetime with 12 lines is calculated using 4 different energy estimators:

- The true MC neutrino energy – ideal case in which we know the neutrino energy (hypothetical experiment).
- The true MC neutrino-induced muon energy – sensitivity that would be obtained by an experiment with perfect energy resolution (again an unrealistic situation).
- The number of reconstructed hits.
- The mean repetition rate R.

Also if the first two estimators are idealistic cases, we use them in order to have an idea of the best possible result. In fact, the sensitivity that is obtained using the true secondary muon energy can be seen as a “limit value” for the ANTARES telescope. If an observable will be found in the future, working better as an energy estimator than the variables proposed in this thesis, in any case its sensitivity will be worst than the limit imposed by the use of the MC value of the muon energy. The neutrino energy gives the best result for the sensitivity; unfortunately, there in no way to get informations about the energy of the interacting neutrino. Only the secondary muon is detected by the ANTARES telescope.

1 year of equivalent livetime is assumed for all the 4 different cases. Each time, the value of the estimator for which the Model Rejection Factor (MRF) reaches the minimum defines the cut value. Hence the use of the cut minimises the flux upper limit, setting the sensitivity of the detector with respect to the signal flux. The upper limit on the source spectrum is assumed equal to:

$$\Phi_{90\%} = \Phi_{test} \cdot MRF. \tag{5.8}$$

The cut in energy is chosen as the value that minimises the quantity MRF $= \frac{\overline{\mu}_{90}(n_b)}{n_s}$ in each of the four considered cases. The test signal Φ_{test} spectrum is assumed to be that defined in eq. 5.1 while the background is the "conventional" Bartol atmospheric neutrino flux, without the "prompt" contribution.

5.3.1 True neutrino energy

In Fig. 5.15 it is shown the cumulative distribution of signal and atmospheric neutrino events as a function of the true MC neutrino energy. From the latter, the average upper limit is computed for each value of true neutrino energy. The MRF as a function of neutrino energy is shown in Fig. 5.16. The minimum value is obtained setting the cut $E_\nu > 10^{4.75}$ GeV = 56.2 TeV, with the MRF equal to 0.27.

5.3.2 True muon energy

In Fig. 5.17 it is shown the cumulative distribution of signal and atmospheric neutrino events as a function of the true (from MC) secondary muon energy. From the latter, the average upper limit is computed for each value of muon energy. The cut in energy is chosen by the minimisation of the MRF. The MRF as a function of muon energy is shown in Fig. 5.18. The minimum value is obtained setting the cut $E_\mu > 10^{4.25}$ GeV, with the MRF equal to 0.36.

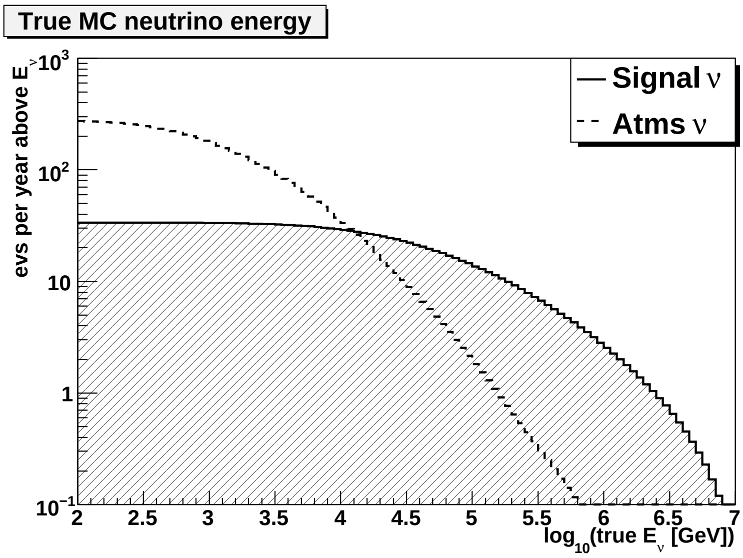

Figure 5.15: Integrated distributions of the true (i.e. from MC) neutrino energy for signal and atmospheric neutrino background.

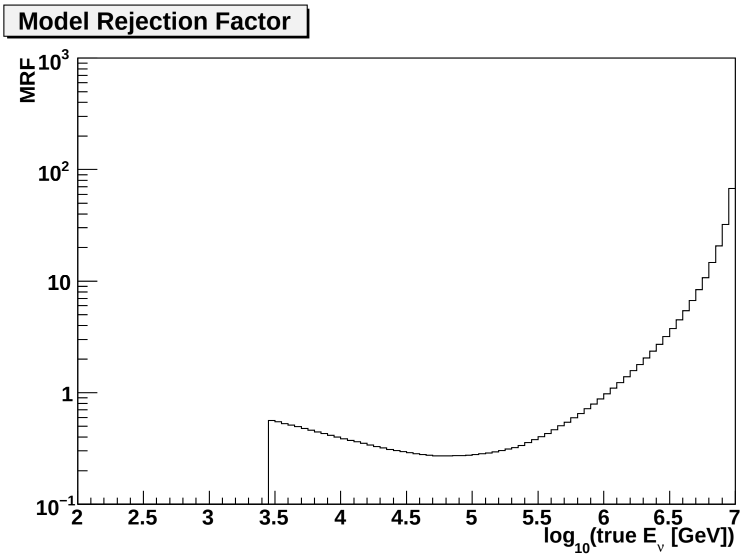

Figure 5.16: Model Rejection Factor as a function of the true neutrino energy. The MRF is computed using the Feldman-Cousins approach. The quantity is minimised by the value $E_\nu = 10^{4.75}$ GeV.

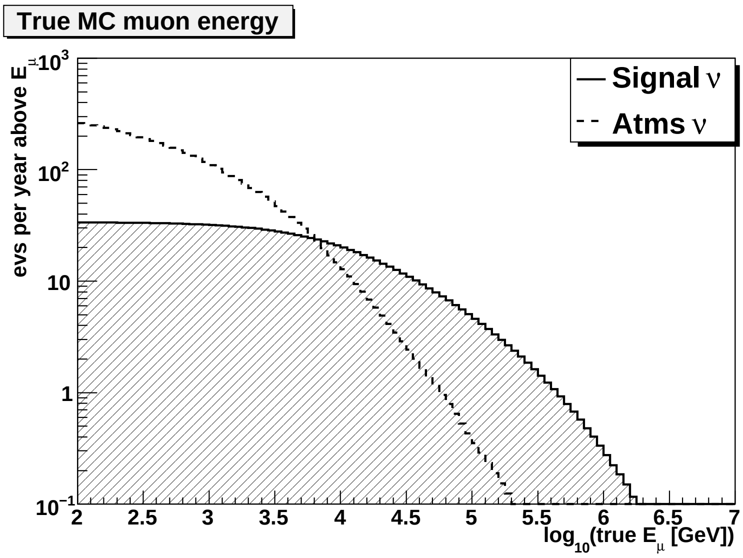

Figure 5.17: Integrated distributions of the true neutrino-induced muon energy for signal and atmospheric neutrino background.

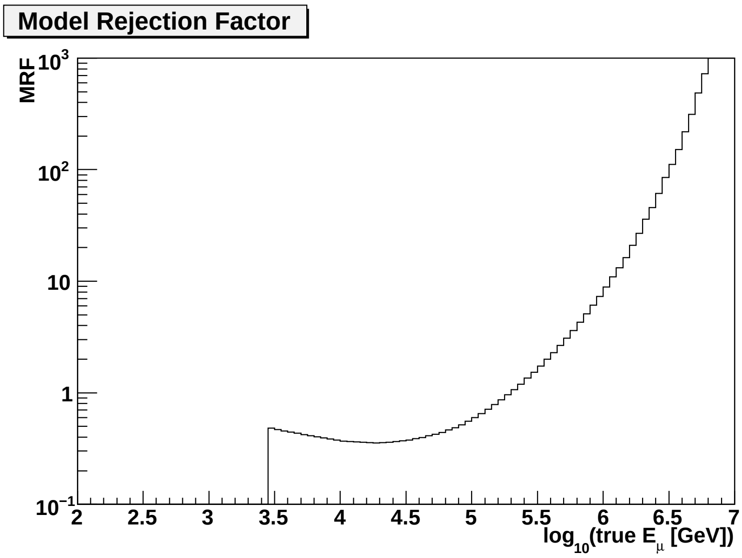

Figure 5.18: Model Rejection Factor as a function of the true neutrino-induced muon energy. The MRF is computed using the Feldman-Cousins approach. The quantity is minimised by the value $E_\mu = 10^{4.25}$ GeV.

5.3.3 Mean number of repetitions R

The cumulative number of signal and atmospheric neutrino events as a function of R is shown in Fig. 5.19. From the latter, the average upper limit (90% C.L.) that would be obtained by an ensemble of experiments with no true signal and only the expected atmospheric neutrino background is computed for each value of R. The minimum value of the MRF is 0.47, in correspondence of $R = 1.26$ (Fig. 5.20).

5.3.4 Number of hits

The cumulative number of signal and atmospheric neutrino events as a function of the number of hits, N_{hit}, is shown in Fig. 5.21. From the latter, the average upper limit (90% C.L.) that would be obtained by an ensemble of experiments with no true signal and only the expected atmospheric neutrino background is computed for each value of N_{hit}. The MRF as a function N_{hit} is shown in Fig. 5.22. The minimum value is obtained setting the cut $N_{hit} > 125$, with the MRF equal to 0.61.

1 year – 12 lines				
Variable	MRF	Best cut	Background	Signal
True neutrino energy	0.27	56.2 [TeV]	4.1	17.9
True muon energy	0.36	18.8 [TeV]	5.8	15.3
Mean repetitions R	0.47	1.26	6.1	11.7
Number of hits N_{hit}	0.61	125	12.5	11.9

Table 5.3: Model Rejection Factor obtained for the four different energy estimators. The “Best cut” is the threshold value for which the minimum is obtained. The number of background and signal events above the cut are also shown.

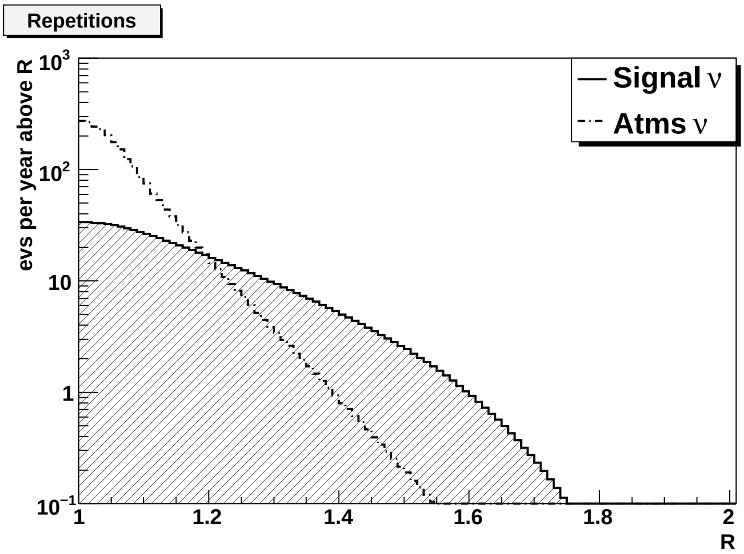

Figure 5.19: Integrated distributions of the mean number of repetitions R for signal and atmospheric neutrino background.

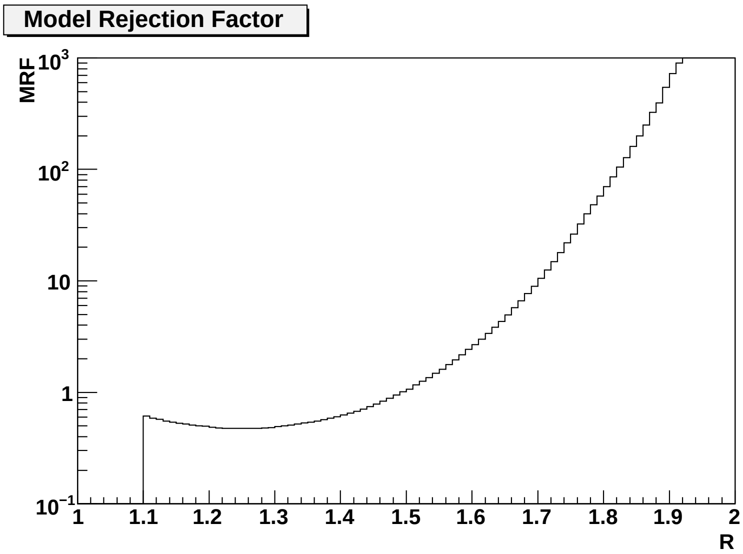

Figure 5.20: Model Rejection Factor as a function of the mean number of repetitions R. The MRF is computed using the Feldman-Cousins approach.The minimum is reached for $R = 1.26$.

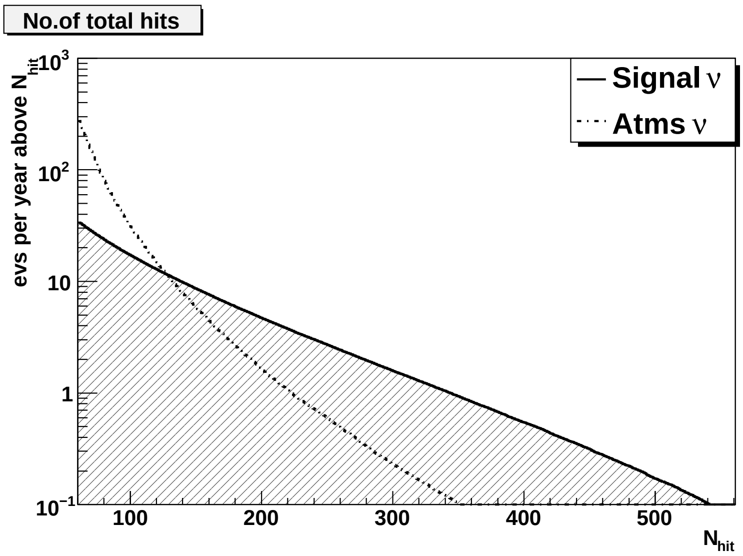

Figure 5.21: Integrated distributions of the hits selected by the reconstruction algorithm for signal and atmospheric neutrino background.

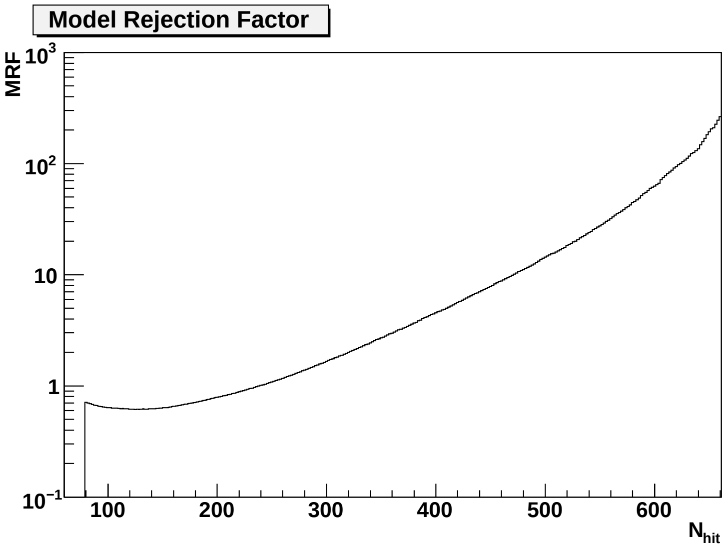

Figure 5.22: Model Rejection Factor as a function of the number of hits N_{hit}. The MRF is computed using the Feldman-Cousins approach. The minimum is for $N_{hit} = 125$.

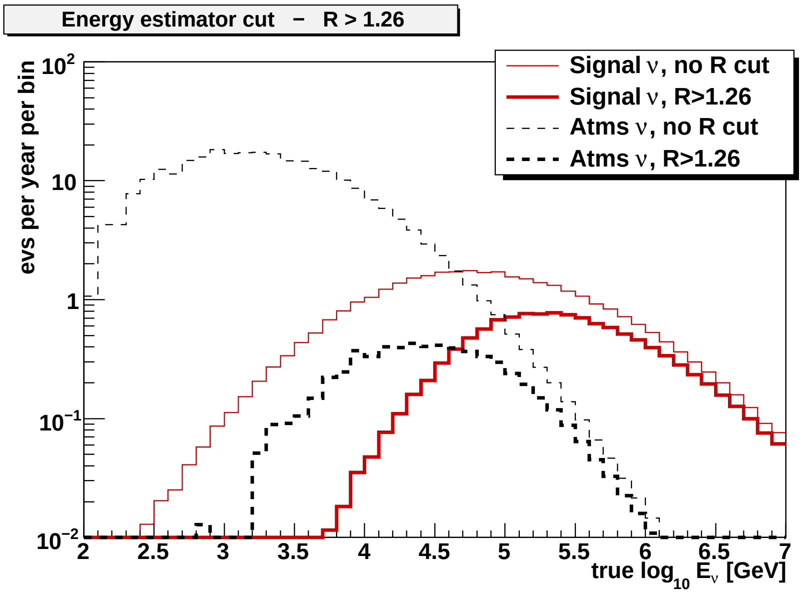

Figure 5.23: Distribution of the true neutrino energy for signal (red lines) and background (black dashed lines) before and after the cut $R > 1.26$. The interval $10^{4.4}$ GeV $< E_\nu <$ $10^{6.5}$ GeV contains the 90% of signal neutrino events.

5.4 Sensitivity results

Table 5.3 summarises the MRF values obtained for the neutrino and muon true energy and for the two energy estimators. Using the neutrino-induced muon true energy, the average upper limit for a flux in the limit of the Waxman-Bahcall bound would be:

$$E^2\Phi_{90\%} < 3.6 \times 10^{-8} \text{ GeV cm}^{-2} \text{ s}^{-1} \text{ sr}^{-1} \quad (1 \text{ year, ideal case}). \tag{5.9}$$

This limit could be reached by the ANTARES detector only with the use of a *perfect* energy estimator, as if the ANTARES telescope had a *perfect* energy resolution in the measurement of the energy of the muon produced by the neutrino interaction. This represent an unreachable limit for our sensitivity.

Considering real ANTARES observables, the mean number of repetitions R is the variable having the lowest MRF. In Fig. 5.23 the number of events per year as a function of the true MC neutrino energy is shown for the signal and background spectra before and after the cut $R > 1.26$. The energy range for the ANTARES sensitivity to muon diffuse flux neutrinos is the energy range defined by the central 90% of the signal events after the cut $R > 1.26$. For this analysis, the central 90% signal region extends from 25 TeV to 3.2 PeV $[4.4 < \log(\frac{E_\nu}{\mathrm{GeV}}) < 6.5]$.

Hence, the sensitivity of the ANTARES telescope to the diffuse fluxes of muon neutrino for 1 year of data acquisition can be evaluated in:

$$E^2\Phi_{90\%} < 4.7 \times 10^{-8}\ \mathrm{GeV\ cm^{-2}\ s^{-1}\ sr^{-1}} \quad \text{(1 year)} \tag{5.10}$$

in the energy range 25 TeV $< E_\nu <$ 3.2 PeV.

5.5 Prompt neutrino models

Above 50 TeV–1 PeV, the dominant component of the atmospheric neutrino flux becomes the semi-leptonic decay of short-lived charmed particles. The resulting neutrinos are called "prompt" neutrinos. Uncertainties in the atmospheric neutrino model can be estimated comparing different prompt models.

The "optimistic" cases estimated by C.G.S. Costa in [97] assuming both the charm production models denoted as RQPM and QGSM are considered. The contribution due to prompt neutrinos is added to the conventional Bartol flux. Fig. 5.24 and Fig. 5.25 show the cumulative distributions for the mean number of repetitions R for the two different prompt models. From the latter, using the MRP procedure cuts are defined and sensitivities (from the MRF) are calculated. The results are shown in table 5.4.

To make a comparison with previous sensitivity calculations done by the ANTARES collaborations, the prompt model that gives the larger background is selected. From the QGSM-optimistic, the ANTARES sensitivity to the diffuse fluxes of muon neutrino for 1 year of data acquisition can be evaluated as:

$$E^2\Phi_{90\%} < 5.6 \times 10^{-8}\ \mathrm{GeV\ cm^{-2}\ s^{-1}\ sr^{-1}} \quad \text{(1 year).} \tag{5.11}$$

The calculated sensitivity of the ANTARES telescope to a E^{-2} cosmic neutrino diffuse flux is around 40% better than the previous calculation [67]. Part of this improvement is due to the definition of the energy estimator R, that has a performance better than the previous estimator, the number of hits, by a factor $\sim 25\%$. Moreover the combined use of a correlated cut on the reconstruction quality parameter and the number of hits improves the capability to reject atmospheric muon background, giving a better efficiency in the selection of high-energy upgoing events. Finally, since the

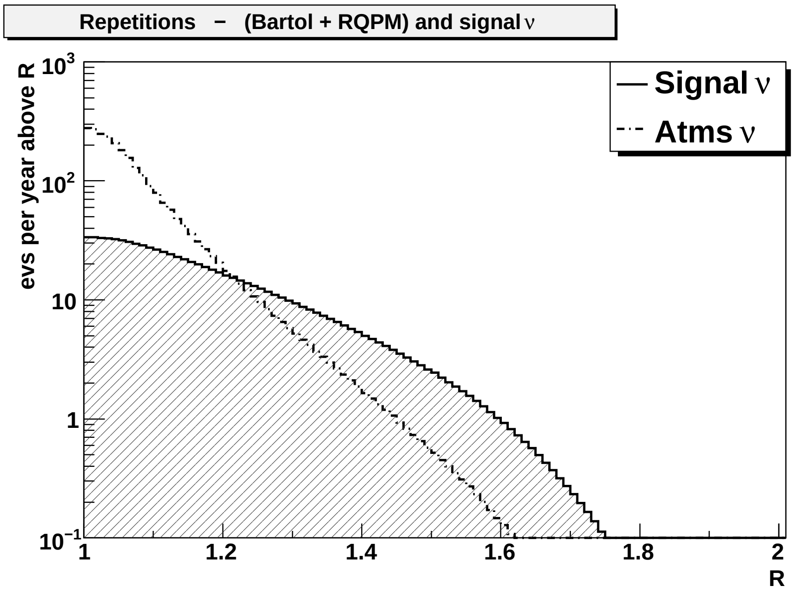

Figure 5.24: Cumulative distributions of the mean number of repetitions R for signal and atmospheric neutrino background(Bartol + RQPM-optimistic).

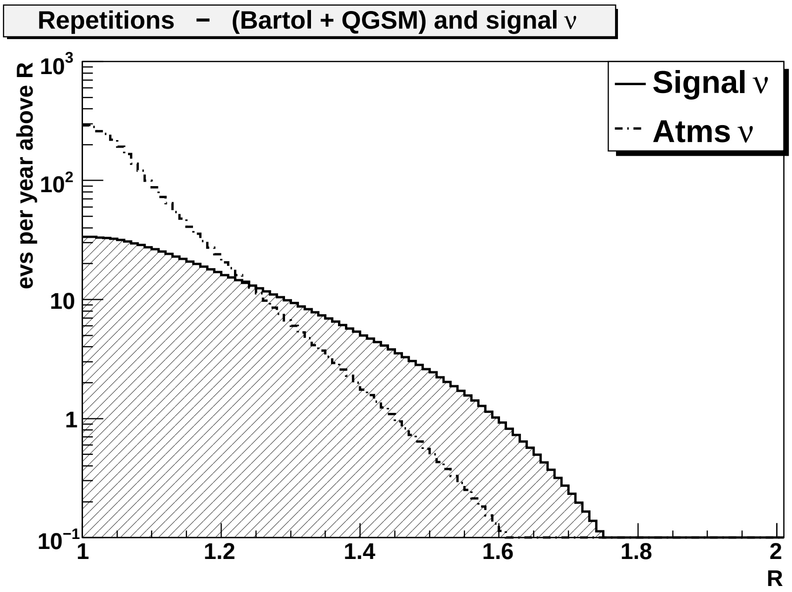

Figure 5.25: Cumulative distributions of the mean number of repetitions R for signal and atmospheric neutrino background (Bartol + QGSM-optimistic).

Repetitions – 1 year				
Model	MRF	Best cut	Background	Signal
Bartol only	0.47	1.26	6.08	11.7
Bartol + RQPM	0.53	1.23	12.1	13.8
Bartol + QGSM	0.56	1.23	14.2	13.8

Table 5.4: Model Rejection Factor obtained for the different atmospheric neutrino models. The "Best cut" is the R value for which the minimum is obtained. The number of background and signal events that remain after the cut are also shown.

time of the calculation in [67] the MC tools have been improved by the whole collaboration, from the simulation of water properties and OMs, to the trigger and electronic simulation.

Chapter 6

Energy estimator quality and real ANTARES data

To guarantee that the detector response to high energy muons is understood, it is important to study energetic events while simultaneously keeping the high energy upgoing candidates blind to the analyser. A cut in $R > 1.23$ (assuming the Bartol flux plus the RQPM-optimistic contribution for atmospheric neutrinos) has been defined through the minimisation of the MRF; the region above $R \gtrsim 1.2$ will mainly contain high energy candidates. In §6.1 an "inverted analysis" is performed over a sample of data corresponding to around 20 days of livetime. Events reconstructed as downgoing that passed the Preliminary cuts are well-reconstructed atmospheric muons: these events can be used to test our MonteCarlo simulation because of their high statistics both at low and high energies.

A first look at ANTARES data is presented in §6.2, excluding events that falls in the "blinding region". The number of active OMs in the ANTARES telescope during different data taking periods is not constant. In the considered period of data acquisition (December 2007 - December 2009) the ANTARES detector shows three main configurations: 12, 10, and 9-lines. In §6.3 the method used to combine data collected in different detector configurations is presented. Finally, the ANTARES sensitivity to diffuse flux muon neutrinos is calculated for real detector and for its effective livetime.

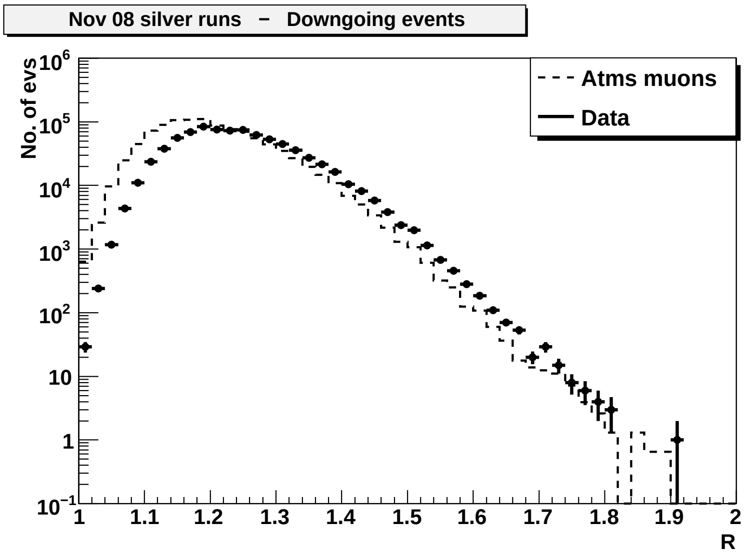

Figure 6.1: Differential distributions of the number of event as a function of the mean reconstruction rate R. Downgoing events ($\theta_{rec} > 90°$) are selected with the Preliminary cuts of the "inverted analysis". Data (equivalent to 19.6 days of livetime in November 2008) are points, dashed line is the atmospheric muon MC weighted for the effective livetime.

6.1 Mean number of repetitions in real data

The energy estimator of the neutrino-induced muon with the best behaviour that was found is the mean repetition rate R, characterised in the previous chapter using MC simulations. The correct simulation of this parameter was checked using a small subsample of data. This require a tuning of the input parameters which are needed to describe the simulation of the ARS electronic circuits. We select a sample of "silver runs" (the "silver run" definition is given in §6.3) from 12-line data taken in November 2008, with an equivalent livetime of 19.6 days.

According to the "blinding policy" described in §5.1.2 and to avoid biasing when defining cuts and procedures, all the plots for real data will not contain events in the region selected above the region in the $\Lambda - N_{hit}$ plane defined by the Intermediate cut (§5.1.2). Possible adjustments on MC will be done looking downgoing events or upgoing events in the "L" region below the pink line in Fig. 5.7.

Because most of the triggering events are atmospheric muons, they can be used to test the simulations and possibly to correct the MonteCarlo in case of discrepancies

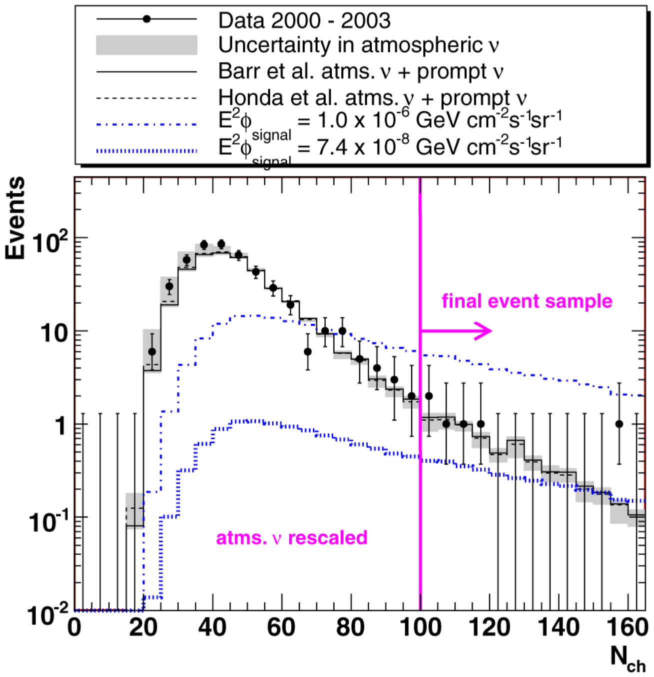

Figure 6.2: The muon neutrinos recorded by the AMANDA-II experiment in 2000-2003 as a function of the number of hits (here N_{ch}, number of channels). Prediction for both conventional and prompt atmospheric neutrinos are shown and their uncertainties are represented by the grey band. The energy-related cut was set to $N_{ch} \geq 100$. Due to the uncertainties in the atmospheric neutrino flux, the total atmospheric background was normalised to the number of data. Instead of renormalising the simulation based on all events with $N_{ch} < 100$, the renormalisation was only based on the region $50 < N_{ch} < 100$. The lower signal flux curve corresponds to the upper limit on a diffuse flux of muon neutrinos obtained in the paper [44].

using the following "inverted analysis".

For the "inverted analysis", all minimum event quality requirements described previously (Preliminary cuts, §5.1.1) were applied, but tracks reconstructed downgoing rather than upgoing were selected (the cut on zenith angle was changed from $\theta_{rec} < 80°$ to $\theta_{rec} > 90°$). The Nov.08 data reconstructed with a zenith angle $> 90°$ are shown in Fig. 6.1 as a function of the mean number of repetitions R. The variable R is an energy-correlated variable: at higher values of R correspond high-energy events and an agreement between data and MC is necessary in the region of high values of R. Small discrepancies in the low-energy region can be ignored for the purposes of this analysis

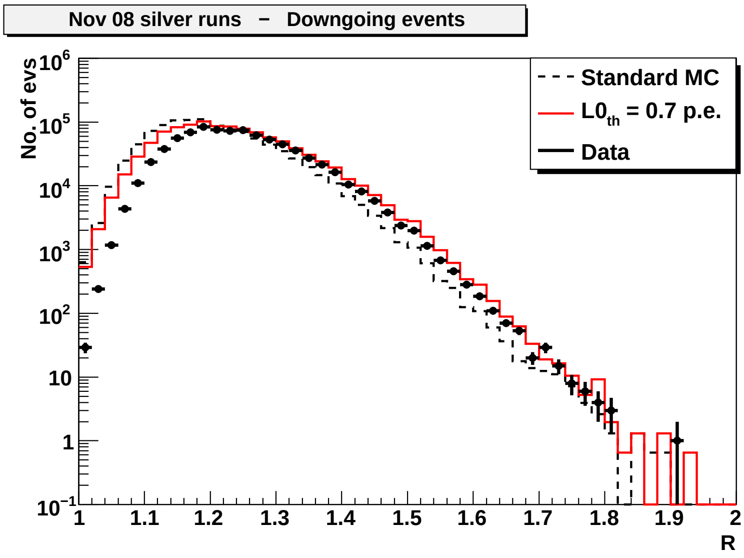

Figure 6.3: Differential distributions of the number of event as a function of R. Downgoing events ($\theta_{rec} > 90°$) are selected with the Preliminary cuts, obviously excluding the zenith cut. Data are points, dashed line is the atmospheric muon MC weighted for the effective livetime, red line is the same MC sample with the correction on the L0 threshold described in the text.

(for comparison, see the plot in Fig. 6.2 taken from [44], IceCube collaboration).

Fig. 6.1 shows that the shape of the data distribution is reproduced quite well by the MC, but there is a relative shift between the two distributions. This problem is probably connected with our simulation of the detector electronic response. As explained in §3.3 and §4.4, every OM has two Analogue Ring Sampler (ARS) that acquire the charge and time information in a “token ring” configuration. In particular, the L0 threshold for the ARS is simulated equal to 0.3 p.e. in the MC. In real detector this L0 threshold should be slightly different. In particular, the MC discrepancies were partially corrected in the high R region assuming that the L0 threshold is higher for the hit detected by the first ARS (ARS0), keeping unchanged the L0 threshold for the second ARS (ARS1). We apply an *a posteriori* correction to the subset of hits selected by the reconstruction algorithm, with the following criteria:

- ($\mathrm{L0}_{ARS0} > 0.7$ p.e.)
- ($\mathrm{L0}_{ARS1} > 0.7$ p.e.) OR [($\mathrm{L0}_{ARS1} \leq 0.7$ p.e.) AND ($\mathrm{L0}_{ARS0} > 0.7$ p.e.)].

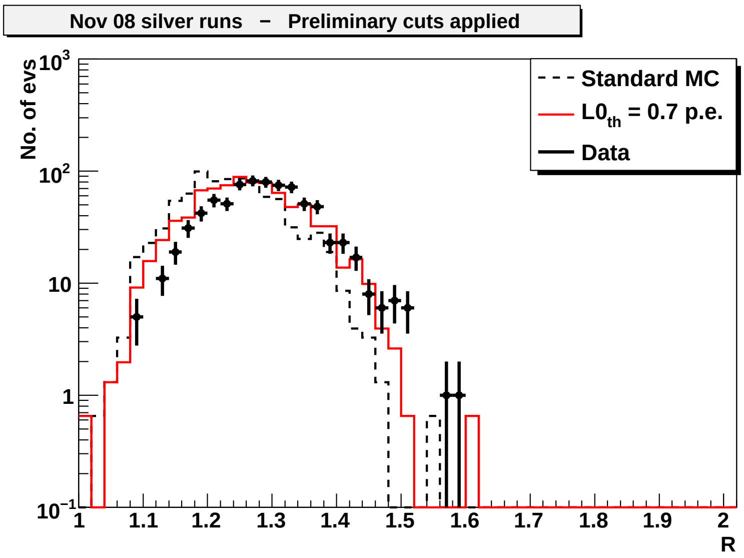

Figure 6.4: Differential distributions of the number of event as a function of the R variable. Upgoing events ($\theta_{rec} < 80°$) are selected with all the Preliminary cuts, excluding events in the "blinding region". Data are points, dashed line is the atmospheric muon MC weighted for the effective livetime, red line is the same MC sample with the correction on the L0 threshold described in the text.

With these assumption, a re-calculation of the mean number of repetition R is made. The distribution of the events rate as a function of the mean repetition rate, as obtained after the above correction for the ARS threshold, is shown in Fig. 6.3. The MC simulation reproduces better the data, after the correction applied to the hit selection, in the region $R \gtrsim 1.2$.

The data and MC comparison of the R distributions for mis-reconstructed as upgoing muons was also studied in the "L" region. These events pass the Preliminary cuts, but events that will pass the Intermediate cut are excluded. The same data sample is used (Nov. 08, "silver runs"). The data-MC distribution of R is shown in Fig. 6.4. As it is clear from table 5.2, these events are mainly mis-reconstructed (as upgoing) atmospheric muons. The contribution from atmospheric neutrinos in negligible in this region (2.6 events are expected in the "L" region for 19.6 days of livetime) with respect to the contribution from atmospheric muon events. The MC contribution of atmospheric neutrinos is not reported in Fig. 6.4.

As a conclusion of the data-MC comparison of the R variable, the agreement is satisfactory in both Fig. 6.3 and 6.4 for $R > 1.2$, while discrepancies are still evident for the low-energy region. This is probably due to a need of a fine-tune setting of the ARS threshold.

6.2 Data-MC comparison for Λ and N_{hit}

Besides the mean repetition rate, other observable variables used for the definition of the cuts were tested using real data. The same data set of 19.6 days was used. The comparison is done only in the “L” region: events that don’t pass Preliminary cuts were rejected and events that pass the Intermediate cut are excluded in the plots.

The event rate per bin as a function of the Λ variable for data and MC is shown in Fig. 6.5. The contribution of the two MUPAGE samples and the Bartol atmospheric neutrinos are presented. In Fig. 6.6 the number of events as a function of the number of hits is reported. In the “L” region, the MonteCarlo distributions of Λ and N_{hit} are in a good agreement with the data.

6.3 Real ANTARES detector

In the previous chapter, the ANTARES sensitivity to a diffuse flux of muon neutrinos was computed for 1 year of livetime with a 12-line detector. Real data that we want to analyse were collected from December 2007 to December 2009. In this period, the ANTARES detector changed its configuration several times. In the first months, the detector was not completly installed in the Mediterranean Sea: data start with a 10-line configuration. Due to some hardware problems, one line stopped to work after some months (9-line configuration). In June 2008, this line was repaired and the last remaining two lines were deployed and connected to the Junction Box (12-line configuration). The remaining time of data acquisition was not taken with all lines active, but some lines had shown problems, some others were disconnected and repaired. Only runs with at least 9 lines are considered.

Data runs are selected according to particular data-quality conditions, that ensures a reduced optical background due to biological activities and natural radioactivity, and requesting a minimum percentage of active detector. The runs that passed the quality

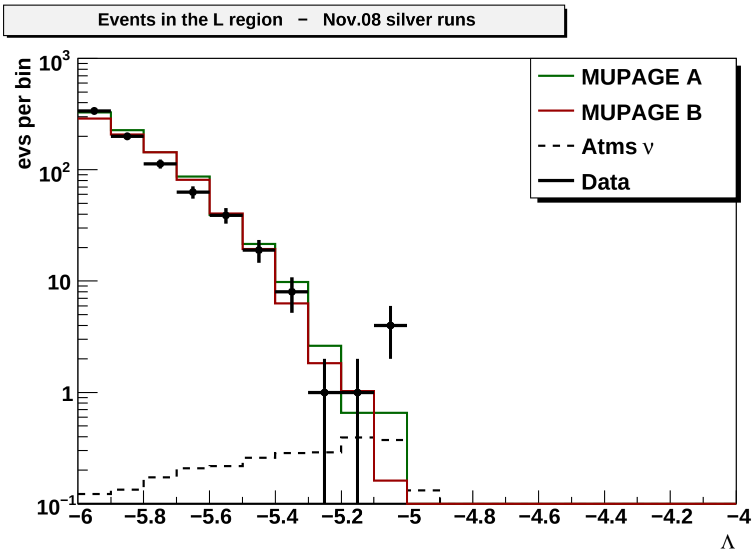

Figure 6.5: Number of events for 19.6 days of equivalent livetime as a function of the quality reconstruction parameter Λ. The events which are included are in the "L" region (events in the the blinding region are excluded). Data are points. Atmospheric muons (MUPAGE "A" green, MUPAGE "B" red) are mis-reconstructed as up-going. The integral number of atmospheric neutrinos (dashed line) is 2.6 events.

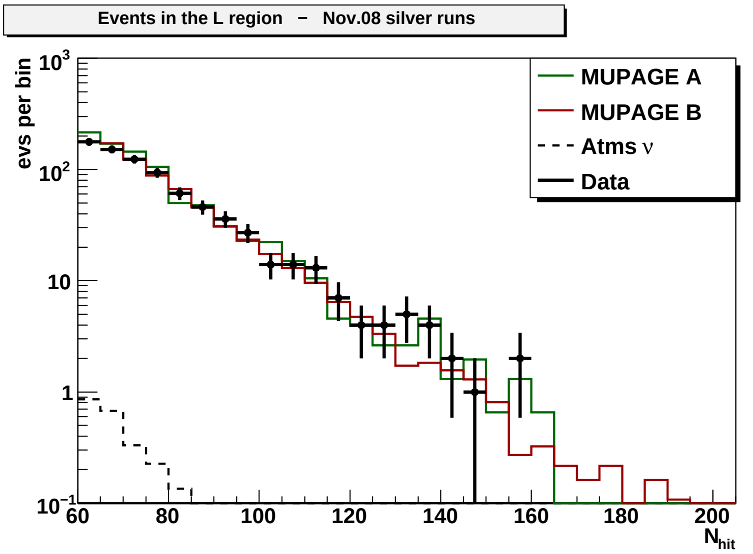

Figure 6.6: Number of events for 19.6 days of equivalent livetime as a function of the number of hits N_{hit}. Same colour conventions as Fig. 6.5

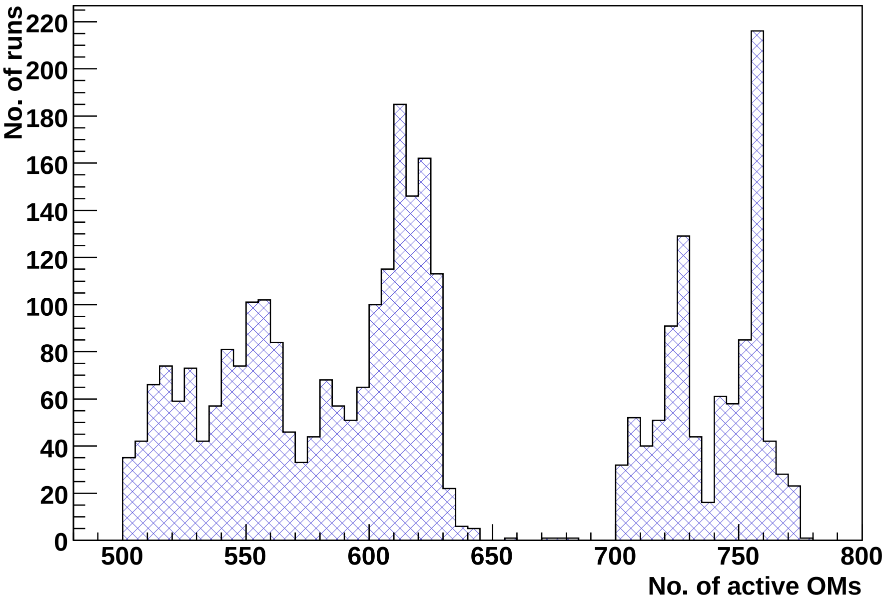

Figure 6.7: Distribution of the number of active optical modules for the 3081 considered runs.

conditions are called “silver runs”. Starting from run 30508 (Dec.07) up to run 45536 (Dec.09), 3081 runs satisfy the conditions; the equivalent livetime is of 335 days.

The runs are selected as “silver” according to the following data-quality conditions:

- Baseline rate < 120 kHz: It is the mean value of the optical rate count over all the OMs. Periods with high optical background are rejected.
- Burst fraction $< 40\%$: It is the percentage of time in which the counting rate of the PMTs is over $1.2\times$baseline.
- Minimum run duration > 1000 s.
- Minimum number of active OMs for 9-line runs = 500.
- Minimum number of active OMs for 10-line runs = 571.
- Minimum number of active OMs for 12-line runs = 701.

Detector conf.	Bkg run no.	No. OMs	OMs interval	No. of runs	Livetime
12-lines	37218	712	> 700	969	70.0 days
10-lines	32185	604	571-700	1167	128.4 days
9-lines	33341	540	500-570	945	136.1 days

Table 6.1: The 3 detector configurations considered in the Monte Carlo simulations. For each configuration, the run used to extract the background in the MC simulation is reported; the number of active OMs in that run; the range of active OMs in order that the real run is described by the background; the number of runs in the interval; the total livetime (computed with the number of active frames).

To correctly consider the different geometries of our detector, each run was classified depending on the number of lines and the number of OMs that are active in the run itself. In each data run, the detector can have a slightly different geometric configuration with respect to neighbouring runs. Fig. 6.7 shows the distribution of the number of active optical modules for the 3081 considered runs. 3 different detector configurations based on the number of lines and the number of active modules are necessary to describe the real detector. For each detector geometry, "an average run" is chosen to be used in MonteCarlo simulation to reproduce the background and the same fraction of active OMs. Some real runs have less and other have more active OMs w.r.t. the run used for the background.

The main informations about the three selected runs are reported in table 6.1. In the same table is also shown the number of runs that can be considered to have a 12-line, 10-line, or 9-line detector configuration, according to the intervals of active OMs for each geometry. The equivalent livetime for each sample of data in table 6.1 provides the relative weight to be used for the related MC sample.

6.4 MonteCarlo geometry configurations

Considering the three different detector geometries, dedicated MC productions have been generated. The TriggerEfficiency program (§4.4), during the simulation of trigger, turns off the OMs that result not active in the run used for background. Hence, starting from this intermediate step of the MC chain is possible to reproduce the detector with this fraction of active OMs.

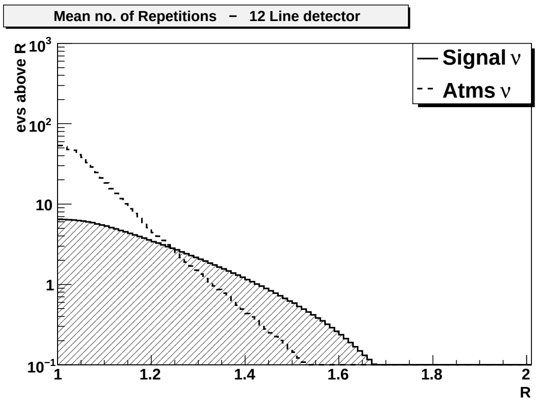

Figure 6.8: 12-lines. Cumulative distributions of R for signal and background ν.

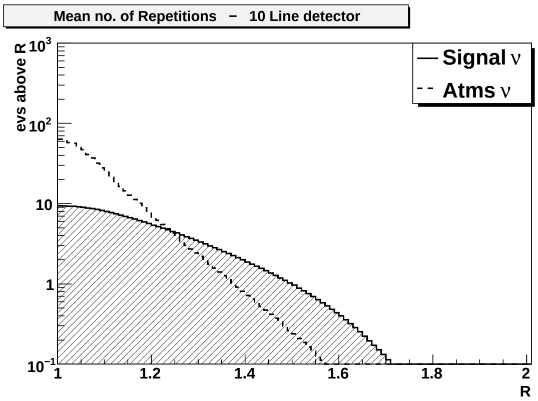

Figure 6.9: 10-lines. Cumulative distributions of R for signal and background ν.

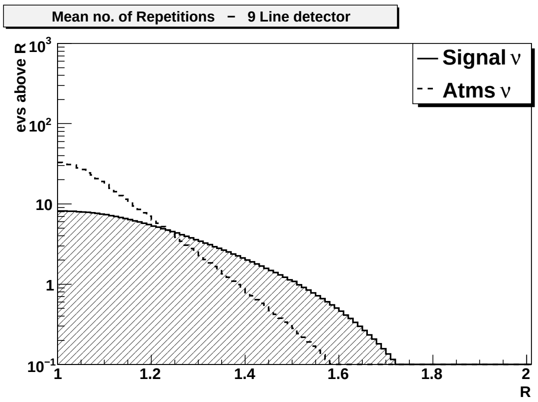

Figure 6.10: 9-lines. Cumulative distributions of R for signal and background ν.

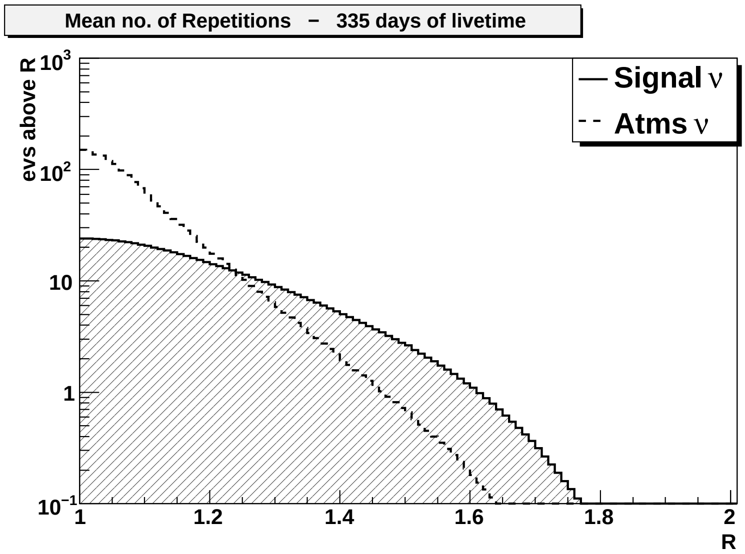

Figure 6.11: Cumulative distributions of the R variable for signal and background neutrinos. Combination of the three different geometries, weighted for their own livetime: 12-lines 70.0 days, 10-lines 128.4 days, 9-lines 136.1 days.

In order to evaluate the sensitivity for the real ANTARES detector using the 335 days of data, the R distributions for signal and background neutrinos in the thee geometrical configurations are needed. For the calculation of R, the correction defined in §6.1 in applied.

In Fig. 6.8-6.10 are shown the cumulative distributions of the R variable for background and signal relative to the three different geometries. The spectrum of signal neutrinos is assumed to be equal to the Φ_{test} defined in eq. 5.1. Concerning the atmospheric neutrino background, the “conventional” Bartol flux plus the RQPM-optimistic “prompt” contribution is taken into account. The uncertainty about the prompt neutrino production can be evaluated from the model without any prompt contribution (Bartol only) and the model that gives the maximum contribution (Bartol + QGSM): see table 5.4. Some pessimistic predictions of the prompt contribution, as for instance the charm production model denotes as pQCD in [97], give a negligible contribution w.r.t. the conventional Bartol and they can be approximated with zero.

For the calculation of the real ANTARES detector sensitivity the Bartol + RQPM-optimistic prompt model is chosen because it predicts an intermediate number of events between the maximum and the minimum. An uncertainties of ±10% on the correspond-

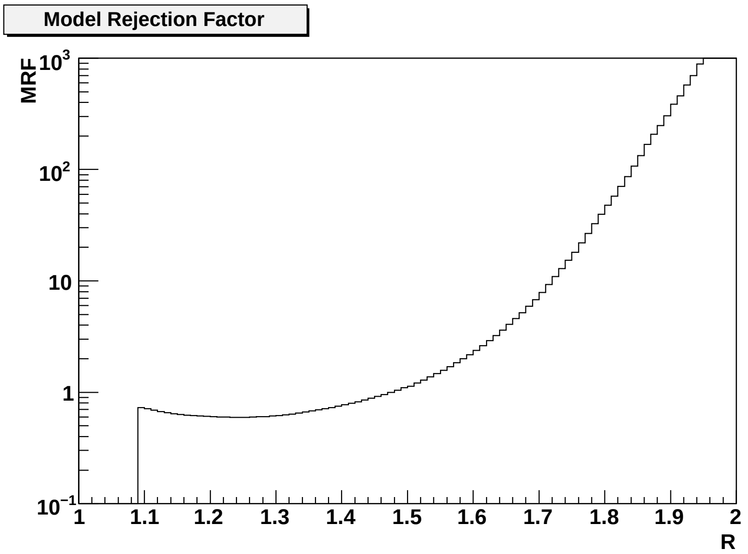

Figure 6.12: MRF for 335 days of considered data as a function of R. Three configurations of the real detector are taken into account. The minimum value is MRF $= 0.59$, for mean repetition rate $R = 1.24$.

ing sensitivity can be approximately attributed to the uncertainties of the prompt neutrino contribution. In Fig. 6.11 the cumulative distribution of the mean repetition rate R for signal and background neutrinos is shown (including prompt production). The three different MC samples have been weighted for the detector equivalent livetime: 12-lines for 70.0 days, 10-lines for 128.4 days, 9-lines for 136.1 days.

Fig. 6.12 shows the final plot for the MRF as a function of R, composed by different contributions from 3 detector configurations. The minimum value is MRF $= 0.59$, obtained for the cut $R > 1.24$. Assuming the Bartol flux plus the RQPM prompt contribution, 11.3 background events and 11.8 signal events are expected.

6.5 Real detector sensitivity

The ANTARES sensitivity to diffuse fluxes of astrophysical muon neutrinos has been calculated for the considered period of 335 days, taking into account the 3 different detector configurations. Using the Feldman-Cousins method, the average flux upper limit is:

$$E^2\Phi_{90\%} < 5.9 \times 10^{-8}\ \text{GeV cm}^{-2}\ \text{s}^{-1}\ \text{sr}^{-1} \quad \text{(335 days).} \tag{6.1}$$

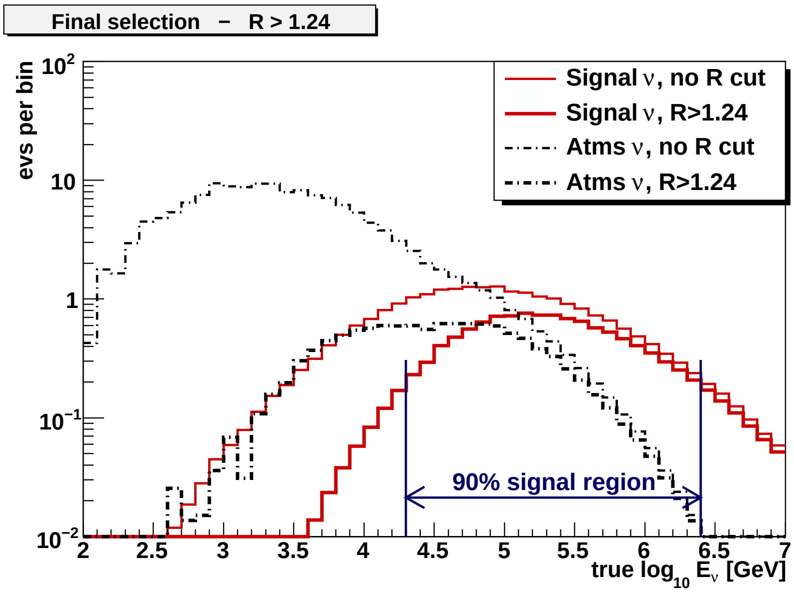

Figure 6.13: Neutrino energy spectrum before and after applying the $R > 1.24$ cut. The upper limit obtained is valid in the region that contains the 90% of signal neutrinos.

Fig. 6.13 shows the energy spectra for signal and background neutrino events before and after the cut $R > 1.24$. The central 90% of the signal is found in the neutrino energy range 20 TeV $< E_\nu <$ 2.5 PeV. Hence, the ANTARES sensitivity spans the same energy range.

In Fig. 6.14 the ANTARES sensitivity calculated here for the real detector configurations is compared with other experiments.

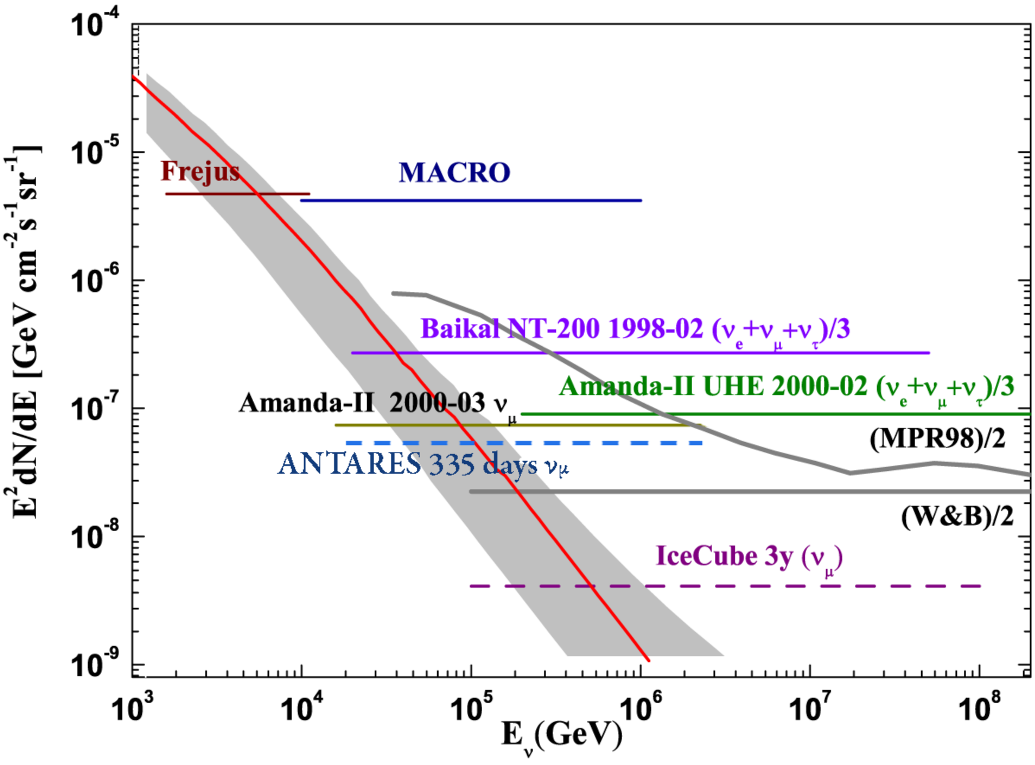

Figure 6.14: Sensitivity of the ANTARES detector for 335 days of data taking compared with sensitivities and upper limits of other experiments for a E^{-2} diffuse flux of high energy neutrinos of one flavour. Experimental upper limits are indicated as solid lines, sensitivities with dashed lines. Upper limits obtained from all-flavour analyses (Baikal and Amanda-II UHE 2000-02) are not directly comparable to the ν_μ upper limits. In that case, either a single flavour limit can be multiplied by three (and compared to an all-flavour result) or an all-flavour limit can be divided by three and compared to a single-flavour result, as it is done in the figure. For reference, the WB and MPR98 limits for transparent sources are also shown. Both upper bounds are divided by two, to take into account the neutrino oscillation effects.

Conclusions

The ANTARES telescope was completed in May 2008; it is composed by 12 lines anchored on the sea bed, equipped with 885 PMTs. The main topic of the ANTARES collaboration is the study of neutrino-emitting astrophysical objects, like AGN, GRB, and supernova remnants.

If the sensitivity of the ANTARES telescope to point-like sources is too poor to detect their fluxes, it is possible to search for an excess of events from unresolved sources, with respect to the expected atmospheric neutrino background. The work presented in this thesis is finalised to the search for diffuse astrophysical fluxes of muon neutrinos with the ANTARES detector.

The first step of this analysis is a study for the rejection of the atmospheric muon background. Even if the detector is located at a depth of 2500 m in the Mediterranean Sea, the flux due to atmospheric muons is $\sim 10^6$ times more intense than the flux due to atmospheric neutrinos. So muons are the main source of triggering events in the ANTARES detector. Looking for upward going events is not sufficient to reject the muon background, because single and multiple muon events can mimic fake upward going particles. Some conditions related with the number of hits and the quality of reconstructed tracks (called "Preliminary cuts" in the thesis) were defined on MonteCarlo samples in order to discard most of bad reconstructed tracks. Then, a more stringent cut ("Intermediate cut"), which relies on the correlation between the reconstruction quality and the number of hits, was defined to completely remove the background from atmospheric muons. Using the MUPAGE MonteCarlo package, developed by the ANTARES Bologna group, a high-statistics sample of atmospheric muons (1 year of equivalent livetime) has been generated to optimise the cut parameters.

The second step is the selection of the diffuse neutrinos from the atmospheric neutrino background. The discrimination between the two neutrino samples is based only on statistical criteria that use an energy-correlated variable. Since atmospheric neutrino energy spectrum follows a power law steeper than that of cosmic neutrinos, an excess of events at high energies would be an evidence of a cosmic diffuse flux. An original energy estimator for the ANTARES experiment, the "mean number of repetitions" R, has been defined. The R observable gives the lowest sensitivity to diffuse fluxes, according to the Model Rejection Potential technique. Hence, the sensitivity of the ANTARES detector for 1 year of data taking with a 12 line detector configuration is:

$$E^2\Phi_{90\%} < 4.7 \times 10^{-8}\ \mathrm{GeV\ cm^{-2}\ s^{-1}\ sr^{-1}} \qquad \text{(1 year, 12 lines)}$$

using the Feldman-Cousins method.

The expected signal and background neutrino event rate is obtained through a MonteCarlo simulation. A small sub-sample of real data was compared with MonteCarlo to check the variables used. The ANTARES sensitivity to diffuse fluxes of astrophysical muon neutrinos has been calculated for a real data-taking period equivalent to 335 days, taking into account 3 different detector configurations. The resulting sensitivity is:

$$E^2\Phi_{90\%} < 5.9 \times 10^{-8}\ \mathrm{GeV\ cm^{-2}\ s^{-1}\ sr^{-1}} \qquad \text{(335 days, 3-detector configuration)}$$

with the central 90% of the signal found in the neutrino energy range 20 TeV $< E_\nu <$ 2.5 PeV.

The upper limit on a diffuse flux of muon neutrinos at Earth published by the AMANDA-II collaboration for 2000-2003 data is 7.4×10^{-8} GeV cm^{-2} s^{-1} sr^{-1}. With this method, the ANTARES detector for 335 days of livetime gives a sensitivity in the Northern hemisphere to diffuse fluxes of muon neutrinos that is competitive with the results published by AMANDA-II in the Southern hemisphere.

The selected ANTARES dataset is going to be analysed in the next months after the "unblinding" procedure approval by the entire collaboration.

List of Figures

List of Tables

Bibliography

[1] V.F. Hess. *Phys. Zeit.*, **13**:1084, 1912.

[2] A. M. Hillas. **Cosmic Rays: Recent Progress and some Current Questions**. *astro-ph/0607109v2*.

[3] M. Longair. *High Energy Astrophysics*. Cambridge University Press, 1992.

[4] B. Wiebel-Sooth, P.L. Biermann, and H. Meyer. *Astron. and Astroph.*, **330**:389–398, 1998.

[5] E. Fermi. **On the origin of cosmic rays**. *Phys. Rev.*, **75**:1169, 1949.

[6] E. Fermi. **Galactic magnetic fields and the origin of cosmic radiation**. *Astroph. J.*, **119**:1, 1954.

[7] J.R. Horandel. **Models of the knee in the energy spectrum of cosmic rays**. *Astrop. Phys.*, **21**:241–265, 2004.

[8] T. Antoni et al. (KASKADE coll.). **Electron, muon, and hadron lateral distributions measured in air-showers by the KASKADE experiment**. *Astrop. Phys.*, **14**:245–260, 2001.

[9] A.M. Hillas. *Ann. Rev. Astron. Astrophys.*, **22**:425, 1984.

[10] K. Greisen et al. *Phys. Rev. Lett.*, **16**:748, 1966.

[11] G.T. Zatsepin and V.A. Kuz'min. *JETP Lett.*, **4**:78, 1966.

[12] The HIRES collaboration. *Phys. Rev. Lett.*, **100**:101101, 2008.

[13] J. Abraham for the Auger coll. *Phys. Rev. Lett.*, **101**:06110, 2008.

[14] M. Takeda et al. *Phys. Rev. Lett.*, **81**:1163, 1998.

[15] R.J. Protheroe. **Towards the Millennium in Astrophysics, Problems and Prospects**. In *International School of Cosmic Ray Astrophysics 10th Course*, page 3, 1998.

[16] T. Chiarusi and M. Spurio. **High-energy astrophysics with neutrino telescopes**. *Eur. Phys. J. C*, **65**(3-4):649–701, 2010.

[17] F. Aharonian et al. **High energy astrophysics with ground-based gamma ray detectors**. *Rep. Prog. Phys.*, **71**:096901, 2008.

[18] A. de Angelis et al. **Very-high-energy gamma astrophysics**. *Riv. Nuovo Cimento*, **31**:187, 2008.

[19] F. Halzen and D. Hooper. **High-energy neutrino astronomy: the cosmic ray connection**. *Rep. Prog. Phys.*, **65**:1025–1078, 2002.

[20] C.E. Fichtel and J.I. Trombka. **Gamma-ray astrophysics: New insight into the Universe**. RP 1386, NASA, 1997.

[21] A. Abdo et al. (Fermi LAT coll.). **Fermi Large Area Telescope Bright Gamma-ray Source List**. *Astroph. J. Suppl.*, **183**:44–66, 2009.

[22] T.C. Weekes et al. **Observation of TeV gamma rays from the Crab nebula using the atmospheric Cherenkov imaging technique**. *Astroph. J.*, **342**:379–395, 1989.

[23] R. Mirzoyan et al. **The first telescope of the HEGRA air Cherenkov imaging telescope array**. *Nucl. Instr. and Meth. A*, **351**:513–526, 1994.

[24] R. Enomoto et al. **Design study of CANGAROO-III, stereoscopic imaging atmospheric Cherenkov telescopes for sub-TeV gamma-ray**. *Astrop. Phys.*, **16**:235–244, 2002.

[25] F. Piron (CAT coll.). **Observation of the gamma-Ray Emission Above 250 GeV from the Blazars Markarian 501 and Markarian 421 by the CAT Cherenkov Atmospheric Imaging Telescope**. In *Proceedings of the XIth rencontres de Blois*, 1999.

[26] J.A. Hinton. **The status of the HESS project**. *New Astron. Rev.*, **48**:331–337, 2004.

[27] T.C. Weekes et al. **VERITAS: the Very Energetic Radiation Imaging Telescope Array System**. *Astrop. Phys.*, **17**:221–243, 2002.

[28] J. Albert et al. **Physics and Astrophysics with a ground-based gamma-ray telescope of low energy threshold**. *Astrop. Phys.*, **23**:493–509, 2005.

[29] C. Stegmann, A. Kappes, J. Hinton, and F. Aharonian. **Potential neutrino signals in a northern hemisphere neutrino telescope from galactic gamma-ray sources**. *Astroph. and Space Science*, **309**:429, 2007.

[30] E. Waxman and J. Bahcall. **High energy neutrinos from astrophysical sources: An upper bound**. *Phys. Rev. D*, **59**:023002, 1998.

[31] E. Waxman and J. Bahcall. **High energy astrophysical neutrinos: The upper bound is robust**. *Phys. Rev. D*, **64**:023002, 2001.

[32] J. Abraham et al. **Correlation of the highest-energy cosmic rays with nearby extragalactic objects**. *Science*, **318**:938–943, 2007.

[33] E. Waxman and J. Bahcall. **High energy neutrinos from cosmological gamma-ray burst fireballs**. *Phys. Rev. Lett.*, **78**:2292, 1997.

[34] D. Guetta et al. **Neutrinos from individual gamma-ray bursts in the BATSE catalogue**. *Astrop. Phys.*, **20**:429, 2004.

[35] D. Horns, F. Aharonian, A. Santangelo, A.I.D. Hoffmann, and C. Masterson. **Nucleonic gamma-ray production in Vela X**. *Astron. and Astroph.*, **451**(L51), 2006.

[36] D. Guetta and E. Amato. **Neutrino flux predictions for galactic plerions**. *Astrop. Phys.*, **19**:403, 2003.

[37] R. Fender and T. Maccarone. **High energy emission from microquasars**. *astro-ph/0310538*.

[38] F. Aharonian et al. (HESS coll.). **Very high energy gamma rays from the direction of Sagittarius A***. *Astron. and Astroph.*, **425**(L13), 2004.

[39] F. Aharonian et al. (HESS coll.). **Very high energy gamma rays from the composite SNR G0.9+0.1**. *Astron. and Astroph.*, **432**(L25), 2005.

[40] P. Sreekumar et al. (EGRET coll.). **EGRET Observation of the Extragalactic Gamma-Ray Emission**. *Astroph. J.*, **494**:523–534, 2000.

[41] R.J. Protheroe, K. Mannheim, and J.P. Rachen. *Phys. Rev. D*, **63**:023003, 2001.

[42] W. Rhode et al. (Frejus coll.). **Limits on the flux of very high energy neutrinos with the Frejus detector**. *Astrop. Phys.*, **4**:217, 1996.

[43] M. Ambrosio et al. (MACRO coll.). **Search for diffuse neutrino flux from astrophysical sources with MACRO**. *Astrop. Phys.*, **19**:1, 2003.

[44] A. Achterberg et al. (IceCube coll.). **Multiyear search for a diffuse flux of muon neutrinos with AMANDA-II**. *Phys. Rev. D*, **76**:042008, 2007.

[45] V. Aynutdinov et al. **Search for a Diffuse Flux of High-Energy Extraterrestrial Neutrinos with the NT2000 Neutrino Telescope**. *Astrop. Phys.*, **25**:140–150, 2006.

[46] M. Ackermann et al. (IceCube coll.). **Search for Ultra-High-Energy Neutrinos with AMANDA-II**. *Astroph. J.*, **675**:1014–1024, 2008.

[47] G.D. Barr, T.K. Gaisser, P. Lipari, S. Robbins, and T. Stanev. *Phys. Rev. D*, **70**:023006, 2004.

[48] G. Fiorentini, A. Naumov, and F.L. Villante. **Atmospheric neutrino flux supported by recent muon experiment**. *Phys. Lett. B*, **510**:173–188, 2001.

[49] A.M. Markov. In *Proceeding of the Rochester Conference*, New York, 1960.

[50] G.A. Askaryan. *JETP*, **14**:441, 1962.

[51] G.A. Askaryan et al. *Nucl. Instr. and Meth.*, **164**:267, 1979.

[52] P. Sapienza and G. Riccobene. **High-energy neutrino astronomy**. *Riv. Nuovo Cimento*, **32**(12), 2009.

[53] R. Gandhi et el. **Ultrahigh-energy neutrino interactions**. *Astrop. Phys.*, **5**:81, 1996.

[54] C. Amsler et al. (Particle Data Group). *Phys. Lett. B*, **667**:1, 2008.

[55] J. Pumplin et al. **New generation of parton distributions with uncertainties from global QCD analysis**. *JHEP*, **7**(12), 2002.

[56] M.H. Reno, R. Gandhi, C. Quigg, and I. Sarcevic. *Phys. Rev. D*, **58**:093009, 1998.

[57] *http://durpdg.dur.ac.uk/hepdata/pdf.html/.*

[58] **The CERN Program library**. *http://wwwinfo.cern.ch/asd/cernlib/.*

[59] G. Ingelman, A. Edin, and J. Rathsman. *Comp. Phys. Comm.*, **101**:108–134, 1997.

[60] T. Sjöstrand. *Comp. Phys. Comm.*, **82**:74–90, 1994.

[61] H. Plothow-Besch. *Comp. Phys. Comm.*, **75**:396–416, 1993.

[62] D.J.L. Bailey. **GENHEN v5r1: Software documentation**. ANTARES internal note, ANTARES-SOFT-2002-004, 2002.

[63] A.M. Cooper-Sarkar, R.C.E. Devenish, and A. De Roeck. *Int. J. Mod. Phys. A*, **13**:3385–3586, 1998.

[64] The CTEQ collaboration. *Eur. Phys. J. C*, **12**:375–392, 2000.

[65] I.A. Sokalski, E.V. Bugaev, and S.I. Klimushin. *Phys. Rev. D*, **64**(074015), 2001.

[66] A. Heijboer. *Track Reconstruction and Point Source Searches with ANTARES.* PhD thesis, NIKHEF, Amsterdam, 2004.

[67] J.D. Zornoza. *Sensitivity to Diffuse Fluxes and Energy Spectrum Reconstruction in the ANTARES Neutrino Telescope*. PhD thesis, Universitat de Valencia, Spain, 2005.

[68] P.A. Cherenkov. **Visible Radiation Produced by Electrons Moving in a Medium with Velocities Exceeding that of Light**. *Phys. Rev.*, **52**:378, 1937.

[69] M. Ambrosio et al. (MACRO coll.). **Neutrino astronomy with the MACRO detector**. *Astroph. J.*, **546**:1038–1054, 2001.

[70] K. Abe et al. **High energy neutrino astronomy using upward-going muons in Super-Kamiokande-I**. *Astroph. J.*, **652**:198–205, 2006.

[71] G. Carminati et al. **Atmospheric MUons from PArametric formulas: a fast GEnerator for neutrino telescopes**. *Comp. Phys. Comm.*, **179**:915–923, 2008.

[72] D. Heck et al. FZKA 6019, Forshungszentrum Karlsruhe, 1998.

[73] J. Hörandel. **On the knee in the energy spectrum of cosmic rays**. *Astrop. Phys.*, **19**:193–220, 2003.

[74] J. Brunner. **Analysis of 2007 and 2008 data with BBfit**. ANTARES internal note, ANTARES-PHYS-2009-006.

[75] F. Halzen and D. Saltzberg. **Tau Neutrino Appearance with a 1000 Megaparsec Baseline**. *Phys. Rev. Lett.*, **81**:4305, 1998.

[76] B.D. Hartmann. *Reconstruction of neutrino-induced hadronic and electromagnetic showers with the ANTARES experiment*. PhD thesis, Erlangen University, Germany, 2006.

[77] J. Brunner. **ANTARES simulation tools**. In *Proceedings of the VLVνT workshop*, Amsterdam, 2003.

[78] *http://antares.in2p3.fr/*.

[79] P. Amram et al. (ANTARES coll.). **Background light in potential sites for the ANTARES undersea neutrino telescope**. *Astrop. Phys.*, **13**:127–136, 2000.

[80] M. Ageron et al. (ANTARES coll.). **Performance of the First ANTARES Detector Line**. *Astrop. Phys.*, **31**:277–283, 2009.

[81] A. Roberts. **The birth of high-energy neutrino astronomy: A personal history of the DUMAND project**. *Rev. Mod. Phys.*, **64**:259, 1992.

[82] L. Kuzmichev. **The Baikal neutrino experiment: from NT200 to NT200+**. In *Proceeding of the* 29^{st} *ICRC*, 2005.

[83] J.A. Aguilar et al. (ANTARES coll.). **Measurement of the atmospheric muon flux with a 4 GeV threshold in the ANTARES neutrino telescope**. *Astrop. Phys.*, **33**:86–90, 2010.

[84] P. Amram et al. (ANTARES coll.). **The ANTARES optical module**. *Nucl. Instr. and Meth. A*, **484**:369, 2002.

[85] A.M. Brown. **Positioning system of the ANTARES Neutrino Telescope**. In *Proceeding of the* 31^{st} *ICRC*, 2009.

[86] J.A. Aguilar et al. (ANTARES coll.). **Transmission of light in deep sea water at the site of the Antares neutrino telescope**. *Astrop. Phys.*, **23**:131–155, 2005.

[87] P. Amram et al. (ANTARES coll.). **Sedimentation and fouling of optical surfaces at the ANTARES site**. *Astrop. Phys.*, **19**:253–267, 2003.

[88] M. Circella. **The construction of ANTARES, the first undersea neutrino telescope**. *Nucl. Instr. and Meth. A*, **602**:1–6, 2009.

[89] J.A. Aguilar et al. (ANTARES coll.). **The data acquisition system for the ANTARES neutrino telescope**. *Nucl. Instr. and Meth. A*, **570**:107–116, 2007.

[90] F. Feinstein. **The analogue ring sampler: A front-end chip for ANTARES**. *Nucl. Instr. and Meth. A*, **504**:258, 2003.

[91] D. Bailey. *Monte Carlo tools and analysis methods for understanding the ANTARES experiment and predicting its sensitivity to Dark Matter*. PhD thesis, University of Oxford, United Kingdom, 2002.

[92] J. Brunner. **Event generators for the ANTARES ν oscillation search**. ANTARES internal note, ANTARES-SOFT-1998-005.

[93] J. Brunner. **Updated tag list for the ANTARES event format**. ANTARES internal note, ANTARES-SOFT-1999-003.

[94] M. Honda et al. *Phys. Rev. D*, **52**:4985–5005, 1995.

[95] G. Battistoni, A. Ferrari, T. Montaruli, and P. Sala. **The FLUKA atmospheric neutrino flux calculation**. *hep-ph/0207035*, 2002.

[96] G.D. Barr, T.K. Gaisser, P. Lipari, S. Robbins, and T. Stanev. *http://www-pnp.physics.ox.ac.uk/~barr/fluxfiles/*.

[97] C.G.S. Costa. **The prompt lepton cookbook**. *Astrop. Phys.*, **16**:193–204, 2001.

[98] Y. Becherini et al. *Astrop. Phys.*, **25**:1, 2006.

[99] **GEANT program manual**. *CERN program library long writeup*, **W5013**, 1993.

[100] S. Navas and L. Thompson. **KM3 User Guide and Reference Manual**. ANTARES internal note, ANTARES-SOFT-1999-011.

[101] P. Antonioli et al. **A three-dimensional code for muon propagation through the rock: MUSIC**. *Astrop. Phys.*, **7**:357, 1997.

[102] M. de Jong. **The TriggerEfficiency program**. ANTARES internal note, ANTARES-SOFT-2009-001.

[103] J. Carr, S. Escoffier, and D. Zaborov. **Proposition for an alternative trigger based on the T3 cluster trigger**. ANTARES internal note, ANTARES-SOFT-2007-016.

[104] *http://root.cern.ch/*.

[105] E.V. Bugaev, V.A. Naumov, S.I. Sinegovsky, and E.S. Zaslavskaya. **Prompt leptons in cosmic rays**. *Nuovo Cimento C*, **12**(1):41–73, 1989.

[106] A.B. Kaidalov and O.I. Piskunova. *Z. Phys. C*, **30**:145, 1986.

[107] L.V. Volkova, W. Fulgione, P. Galeotti, and O. Saavedra. *Nuovo Cimento C*, **10**:465, 1987.

[108] G. Carminati. *Study of diffuse flux of high energy neutrinos through showers with the ANTARES neutrino telescope.* PhD thesis, Università di Bologna, Italy, 2010.

[109] G.C. Hill and K. Rawlins. **Unbiased cut selection for optimal upper limits in neutrino detectors: the model rejection potential technique**. *Astrop. Phys.*, **19**:393–402, 2003.

[110] N. Cottini and T. Stolarczyk. **Atmospheric neutrinos with 5 lines**. ANTARES internal note, ANTARES-PHYS-2008-003.

[111] G.J. Feldman and R.D. Cousins. **Unified approach to the classical statistical analysis of small signals**. *Phys. Rev. D*, **57**(7):3873–3889, 1998.